Multivalent ions for tuning the phase behaviour of protein solutions

Dissertation

der Mathematisch-Naturwissenschaftlichen Fakultät

der Eberhard Karls Universität Tübingen

zur Erlangung des Grades eines

Doktors der Naturwissenschaften

(Dr. rer. nat.)

vorgelegt von

Olga Matsarskaia

aus Genf (Schweiz)

Tübingen

2018

Tag der mündlichen Qualifikation: 07.12.2018

Dekan: Prof. Dr. Wolfgang Rosenstiel

1. Berichterstatter: Prof. Dr. Frank Schreiber

2. Berichterstatter: PD Dr. Fajun Zhang

Contents

Abstract

Protein phase behaviour is of importance in various areas of research such as structural biology, rational drug design and delivery, medicine (in particular protein condensation diseases), biotechnology, food science and cell biology. A particularly intriguing variety of phase behaviours can be induced in negatively charged, globular proteins in the presence of multivalent salts such as lanthanide (Ln) chlorides. These behaviours include reentrant condensation, crystallisation and cluster formation as well as liquid-liquid phase separation (LLPS) into a protein-rich and a protein-poor phase. LLPS can occur upon a temperature decrease or increase, which is referred to as an upper or a lower critical solution temperature (UCST- and LCST-LLPS), respectively. In the present thesis, the complex phenomenon of LCST-LLPS in systems of bovine serum albumin (BSA) and multivalent salts is investigated from different perspectives including thermodynamic, (non-)equilibrium and spectroscopic studies in a challenging set of experiments.

In the first part of this thesis, the rather unusual phenomenon of LCST-LLPS in aqueous systems consisting of BSA and yttrium chloride (YCl_3) is characterised thermodynamically. Surface charge (zeta (ζ) potential) and isothermal titration calorimetry (ITC) measurements show LCST-LLPS to be a hydration entropy-driven condensation. As the Y^{3+} cations bind to negatively charged residues on the protein surface and bridge protein molecules, highly ordered water structures around both the surface residues as well as the cations break up and water molecules are released into the bulk solution. This leads to an increase of the overall entropy of the system.

Starting from the Y^{3+}-induced LCST-LLPS described above, the second part of this thesis is concerned with the influence that the nature of the multivalent cations used has on this phase transition. The experiments focus on the three multivalent salts $HoCl_3$, YCl_3 and $LaCl_3$. Temperature-controlled UV-Vis absorbance measurements demonstrate that the transition temperature T_{trans} separating homogeneous from phase-separated states of the BSA-salt systems shifts to lower values when $HoCl_3$ is used. In contrast, using $LaCl_3$ leads to higher T_{trans} values. YCl_3, used as a reference system, leads to intermediate T_{trans}. These findings indicate that the interprotein interactions induced by $HoCl_3$ are much stronger than those induced by $LaCl_3$ or YCl_3. Importantly, this finding is corroborated by synchrotron small-angle X-ray scattering (SAXS) data which show the reduced second virial coefficient B_2/B_2^{HS} to be lowest in BSA-$HoCl_3$ systems, again pointing towards a stronger interprotein attraction induced by this salt. Zeta potential measurements confirm that Ho^{3+} has a stronger affinity to BSA than Y^{3+} and La^{3+}. The overall protein-protein and protein-cation interaction strengths can therefore be ranked

according to the order $Ho^{3+} > Y^{3+} > La^{3+}$. Taking into account their various characteristics such as radius, electron configuration and, importantly, hydration behaviour, multivalent cations are thus shown to be a sensitive tool to fine-tune protein interactions and their resulting phase behaviours in solution.

Having established the influence of cation characteristics on BSA phase behaviour, the third part is concerned with the kinetics of LCST-LLPS of BSA in the presence of varying ratios of $HoCl_3$ and $LaCl_3$. Using synchrotron ultra-small-angle X-ray scattering (USAXS), it is found that with an increasing $HoCl_3$ concentration — i.e., with increasingly attractive BSA-BSA interactions — the growth behaviour of the characteristic system length $\xi(t, T)$ is more likely to deviate from the $\xi \sim t^{1/3}$ growth law. A stronger interprotein attraction, moreover, leads to arrested states at lower temperatures. The results imply that both temperature and the overall cation-mediated protein-protein interaction strength can be used to obtain multidimensional control over the kinetics of LLPS in the BSA-cation systems used.

In the final part, the mechanism behind LCST-LLPS is investigated spectroscopically on the molecular scale. To this end, the change in the coordination number (CN) of Y^{3+} cations in BSA solutions is monitored using extended X-ray absorption fine structure (EXAFS) spectroscopy. Applying this method to protein-poor and protein-rich phases, it can be shown that the CN of Y^{3+} is higher in the protein-poor than in the protein-rich phase. This is attributed to the fact that in the protein-poor phase more Y^{3+} cations are surrounded by hydration shells and not bound to BSA or forming cation bridges between BSA molecules. The results obtained using EXAFS align well with the current rationalisation of LCST-LLPS as a hydration entropy-driven phenomenon.

The results obtained indicate that a careful choice of the multivalent cation used can fine-tune protein interactions and their phase behaviour in solution. In addition, EXAFS data provide atom-level insights into the mechanism of LCST-LLPS. These findings are of strong interest not only for a fundamental understanding of protein and soft matter thermodynamics, but are also potential anchoring points for the design of stimuli-responsive “smart” materials based on polymers, colloids or proteins.

Zusammenfassung in deutscher Sprache

Das Phasenverhalten von Proteinsystemen spielt eine wichtige Rolle in vielen Forschungsgebieten, z.B. in der Medizin und insbesondere bei der Untersuchung bestimmter Erkrankungen (engl. *protein condensation diseases*), in der Strukturbiologie, beim molekularen Design von Medikamenten und deren Verabreichung, in der Biotechnologie sowie der Zellbiologie. Mehrwertige Salze können in wässrigen Lösungen negativ geladener, globulärer Proteine eine faszinierende Vielfalt von Phasenverhalten induzieren. Hierzu gehören die sogenannte "reentrant condensation" (ein von der Salzkonzentration abhängiger Wechsel zwischen kondensierten und homogenen Zuständen), die Kristallisation, die Bildung von Proteinclustern sowie eine Flüssig-Flüssig-Phasentrennung (engl. *liquid-liquid phase separation*, LLPS) in eine proteinreiche und eine proteinarme Phase. Die Phasentrennung kann bei Temperaturerniedrigung (obere kritische Lösungstemperatur, engl. *upper critical solution temperature*, UCST-LLPS) oder bei Temperaturerhöhung (untere kritische Lösungstemperatur, engl. *lower critical solution temperature*, LCST-LLPS) auftreten. In der vorliegenden Arbeit wird das komplexe Phänomen der LCST-LLPS in Systemen aus Rinderserumalbumin (engl. *bovine serum albumin*, BSA) und multivalenten Salzen mithilfe zahlreicher komplementärer Methoden (diese beinhalten u.a. thermodynamische und spektroskopische Untersuchungen in (Nicht-) Gleichgewichtssystemen) umfassend beleuchtet.

Im ersten Teil der Arbeit wird das in Proteinsystemen recht selten beobachtete Phänomen einer Flüssig-Flüssig-Phasentrennung mit einer unteren kritischen Lösungstemperatur (LCST-LLPS) in wässrigen Lösungen von BSA und dem Salz Yttriumchlorid (YCl_3) thermodynamisch charakterisiert. Messungen der Oberflächenladung (ζ (zeta)-Potential) des Proteins sowie isotherme Titrationskalorimetrie (engl. *isothermal titration calorimetry*, ITC) zeigen, dass LCST-LLPS hier eine hydrationsentropisch getriebene Kondensation darstellt. Binden Y^{3+}-Kationen an negativ geladene chemische Gruppen auf der Proteinoberfläche, so werden hochgeordnete Wasserstrukturen um diese Gruppen sowie um die Kationen aufgebrochen und die Wassermoleküle in die Lösung freigesetzt. Dies bewirkt eine Erhöhung der Gesamtentropie des Systems.

Aufbauend auf diesen Erkenntnissen befasst sich der zweite Teil der Arbeit mit dem Einfluss kationenspezifischer Eigenschaften auf das Phasenverhalten von BSA-Lösungen. Die durchgeführten Experimente konzentrieren sich auf die drei mehrwertigen Salze $HoCl_3$, YCl_3 und $LaCl_3$. Temperaturkontrollierte Absorptionsspektroskopie von ultraviolettem und sichtbarem Licht (engl. *ultraviolet-visible*

(UV-Vis) spectroscopy) zeigt, dass die Temperaturen, bei denen ein Übergang von einem homogenenen zu einem phasengetrennten System erfolgt (engl. *transition temperature*, T_{trans}), im Falle von $HoCl_3$ sehr niedrig sind. Im Gegensatz dazu führt die Verwendung von $LaCl_3$ zu recht hohen T_{trans}-Werten. Bei YCl_3, welches hier als Referenzsystem dient, liegen die T_{trans} in einem mittleren Bereich. Diese Ergebnisse belegen, dass die durch $HoCl_3$ hervorgerufenen Protein-Protein-Wechselwirkungen deutlich stärker sind als die durch $LaCl_3$ und YCl_3 induzierten. Diese Erkenntnis wird durch synchrotronbasierte Röntgen-Kleinwinkelstreuung (engl. *small-angle X-ray scattering*, SAXS) untermauert. Letztere zeigt, dass die reduzierten zweiten Virialkoeffizienten B_2/B_2^{HS} bei der Kombination von BSA und $HoCl_3$ von allen drei untersuchten Systemen die niedrigsten Werte annehmen. Dies weist erneut darauf hin, dass $HoCl_3$ zu stärkeren Protein-Protein-Wechselwirkungen führt. Zeta-Potentialmessungen unterstützen die Erkenntnis, dass Ho^{3+}-Kationen eine höhere Affinität zu BSA haben als Y^{3+}- und La^{3+}-Kationen. Insgesamt können die Stärken der Kation-Protein- und der kationeninduzierten Protein-Protein-Wechselwirkungen in der Reihenfolge $Ho^{3+} > Y^{3+} > La^{3+}$ angegeben werden. Somit wird demonstriert, dass Kationenparameter wie z.B. ihr Radius, ihre Elektronenkonfiguration und insbesondere ihr Hydrationsverhalten wichtige Ansatzpunkte sind, um die Wechselwirkungen und das Phasenverhalten von Proteinlösungen zu modulieren.

Nachdem eine Beziehung zwischen Kationencharakteristika und dem Phasenverhalten der untersuchten BSA-Kation-Systeme hergestellt wurde, befasst sich der dritte Teil der Arbeit mit der Kinetik der LCST-LLPS von BSA in der Gegenwart verschiedener Verhältnisse von $HoCl_3$ und $LaCl_3$. Mittels synchrotronbasierter Röntgen-Ultrakleinwinkelstreuung (engl. *ultra small-angle X-ray scattering*, USAXS) lässt sich feststellen, dass das Wachstumsverhalten der systemspezifischen Korrelationslänge $\xi(t, T)$ mit steigender $HoCl_3$-Konzentration — d.h. mit stärker attraktiven BSA-BSA-Wechselwirkungen — zunehmend vom $\xi \sim t^{1/3}$-Wachstumsgesetz abweicht. Weiterhin führt eine stärkere Attraktion bereits bei tiefen Temperaturen zu stationären Zuständen (engl. *arrested states*), d.h., einer extrem langsamen Entwicklung von $\xi(t, T)$. Die Ergebnisse belegen, dass sowohl die Temperatur der Systeme als auch die effektive Stärke der kationeninduzierten attraktiven BSA-BSA-Wechselwirkungen verwendet werden können, um die Kinetik der LLPS auf mehreren Ebenen zu kontrollieren.

Im letzten Teil dieser Arbeit wird der LCST-LLPS-Mechanismus auf atomarer Ebene untersucht. Hierzu wird die Koordinationszahl von Y^{3+}-Kationen in BSA-Lösungen mithilfe von einer bestimmten Art von Röntgenabsorptionsspektroskopie (engl. *extended X-ray absorption fine structure spectroscopy*, EXAFS) ermittelt. Wird diese Methode auf proteinarme und -reiche Phasen angewandt, so kann gezeigt werden, dass die Koordinationszahl von Y^{3+} in der proteinarmen Phase höher ist. Dies wird darauf zurückgeführt, dass in der proteinarmen Phase mehr Y^{3+}-Kationen von einer Hydrathülle umgeben und nicht an BSA gebunden sind bzw. Kationenbrücken zwischen Proteinmolekülen bilden. Die erhobenen EXAFS-Daten stützen somit das aktuelle Verständnis der LCST-LLPS

als hydrationsentropiegetriebenen Phasenübergang.

Die dargestellten Ergebnisse zeigen, dass die Wahl des verwendeten mehrwertigen Kations Protein-Protein-Wechselwirkungen und das Phasenverhalten von Proteinen beeinflussen und modulieren kann. EXAFS-Daten erlauben weiterhin einen Einblick in die atomare Ebene des Mechanismus der postulierten LCST-LLPS. Die Ergebnisse sind von Bedeutung für ein grundlegendes Verständnis der Thermodynamik von Proteinen und weicher Materie im Allgemeinen. Zusätzlich bieten sie potentielle Anhaltspunkte für die praktische Anwendung des hier erworbenen Wissens, z.B. in der Entwicklung kolloid-, protein- oder polymerbasierter "intelligenter" Materialien.

Part I

Introduction

Chapter 1

Introduction to proteins

1.1 Proteins in a biological context

Proteins are biopolymers ubiquitously present in living organisms and composed of amino acids which are interconnected by peptide bonds. Starting out as linear peptide chains, they undergo an elaborate folding process leading to their final native structures [1]. Their size range spans from small peptides consisting of only a few amino acids to large and highly complex structures [2].

In addition to their pivotal roles in living cells [1], proteins are also important objects of various areas of applied science. They serve as biologically degradable surfactants in laundry detergents, are essential components of food supplements for athletes or those affected by malnutrition and are at the heart of pharmaceutical formulations such as hormone replacements, digestive enzyme supplements or antibody-based drugs [3, 4].

As a response to a variety of factors such as temperature, pressure, radiation, ionic strength or pH, protein solutions can undergo various changes of state of matter. The latter include crystallisation; unfolding and denaturation [5]; fibril formation [6]; aggregation [7] as well as reentrant condensation, liquid-liquid phase separation (LLPS) and arrest in the presence of multivalent counterions [8–14]. Such transitions lead to changes in the properties of the protein solutions in question. These can be beneficial in crystallography and structural biology, but at the same time prove a major drawback for transport and storage of medication [3, 15]. Protein aggregation and LLPS can also contribute to the development of so-called "protein condensation diseases" such as sickle cell anemia [16] or eye cataract [17]. In a non-pathological context, LLPS is crucial for intracellular organisation [18–21]. Finally, protein phase transitions are important driving mechanisms in the food industry [22, 23].

The ubiquity of proteins and their importance in many areas of everyday life are therefore a strong motivation for an extensive, systematic investigation of the mechanisms underlying protein phase behaviour. Rationalising the latter is of utmost importance for a thorough understanding of crystal growth kinetics which is a major obstacle in structural biology [24, 25], and establishing controllable, reproducible conditions for obtaining diffraction-quality crystals. Furthermore, such investigations can provide valuable insights into the development and prevention of protein condensation diseases and propel the design of environmentally com-

patible, stimuli-responsive "smart" materials [26].

The aforementioned complexity of protein molecules increases further when considering their interactions with each other and with their surroundings such as solvent molecules or co-solutes. Such interactions include electrostatic and steric forces, hydrophobic interactions, intra- and inter-molecular hydrogen bonds and depletion forces [27]. The focus of the present thesis is a thermodynamic rationalisation of protein phase transitions and the induction and control thereof using multivalent ions. A comprehensive investigation and general understanding of protein phase behaviour thus requires a biological approach to proteins to be complemented by a physical perspective. The following section therefore presents a physical approach to proteins based on insights from colloid science.

1.2 Proteins in a physical context

When stuyding proteins within a framework of colloid science, it is convenient to describe them by simple models which allow to shift the focus from the individual protein molecule to ensemble properties of protein systems (e.g. solutions).

Colloids have a typical radius on the nm to µm scale. When immersed in a solution, a defining characteristic of colloidal systems is the predominance of Brownian motion over sedimentation, implying that the sedimentation length l_{sed} (the ratio between the thermal energy k_BT and the gravitational constant g) is larger than the radius r_{coll} of the colloidal particles, i.e.

$$l_{sed} = \frac{k_BT}{m^*g} > r_{coll} \tag{1.1}$$

with m^*, the so-called buoyant mass, being equal to $(4\pi/3)\Delta\rho r_{coll}^3$ [28] ($\Delta\rho$ is the density difference between colloids and solvent). Examples of colloidal systems include simple suspensions of gold or silver particles in, e.g., water or a buffer, but can also be more complex (such as paint, dairy products or cosmetics). The intriguing aspect of colloidal solutions is that they can be considered analogous to atoms (sometimes being referred to as "superatoms"[29]), making them valuable tools for fundamental thermodynamic studies. As an example, experiments performed by Perrin based on theoretical considerations by Einstein showed that Boltzmann's distribution was able to account for the sedimentation equilibrium of resin colloids in solution [28]. These experiments were a pivotal step towards proving the existence of atoms and molecules in the beginning of the 20^{th} century [29].[1]

In the following decades, the field of colloid science developed rapidly in terms of both theory and experiments. In 1954, Asakura and Oosawa [30] published a

[1] Note, however, that in contrast to the simple hard sphere potential determining the interactions between atoms, interactions between colloids can be tuned by varying parameters such as surface charge, pH, type and concentration of co-solute or temperature [28].

theoretical explanation of the so-called depletion attraction (also known as "volume exclusion" or as the "excluded volume" effect), a phenomenon describing the introduction of an attractive force F_{attr} between colloids not initially attracted to each other in a solution of co-solutes such as non-adsorbing polymers. The mechanism behind this attraction is based on the degrees of freedom gained by (i.e. an increase in the entropy of) the co-solute molecules when the face-to-face distance r between the colloidal particles (visualised as parallel and large plates by the authors) decreases to a value smaller than the diameter σ of the co-solutes. F_{attr} is then given as

$$F_{attr} = k_B T N \frac{\partial \ln \tilde{Q}}{\partial r} \tag{1.2}$$

with

$$\tilde{Q} = \int_V \exp(-u(x,r)/k_B T)\, dx. \tag{1.3}$$

where $u(x,r)$ describes the potential energy of a co-solute molecule at position x resulting from its interaction with the colloids and N is the total number of co-solute molecules. Another way to rationalise this attractive force is to consider the osmotic pressure Π of the colloid-co-colute system [30],

$$\Pi = k_B T N/V \tag{1.4}$$

(where V is the total volume of the solution) exhibited by the solution surrounding the colloids. As co-solute particles are supplanted from the space between the colloids and become part of the solution surrounding them, Π increases, pushing the colloids closer together.

1.2.1 The importance of the interaction range

Based on the insights obtained by Asakura and Oosawa, Gast *et al.* [31] combined an electrostatic interaction potential with a volume exclusion potential, obtaining results in quantitative agreement with experiments on colloidal depletion systems performed by Sperry *et al.* [32]. A further publication by the same authors [33] demonstrates a successful application of their theory to experiments with systems of polystyrene latex and hydroxyethylcellulose; subsequent experiments [34] and simulations [35] further corroborated and extended these findings. Importantly, the work by Gast *et al.* showed that the range of the attractive potential — controlled by the radius of gyration of depleting polymers — between the colloidal particles has a strong influence on the characteristics of the phase diagram describing the system in question. These experimental and theoretical considerations thus raise the necessity to classify colloidal phase transitions and diagrams between colloidal particles based on their respective interaction ranges. In the following, a brief overview will be given on the relations between phase diagrams and interaction ranges in atomic and colloidal systems.

1.2.2 Phase diagrams and transitions of colloidal systems

The hard sphere model

A first approach towards describing the phase behaviour of colloids is *via* hard spheres (HS) with the corresponding interaction potential [36, 37]

$$u(r) = \begin{cases} \infty \text{ for } r \leq \sigma \\ 0 \quad \text{for } r > \sigma \end{cases} \tag{1.5}$$

where r is the centre-to-centre interparticle distance and σ is the particle diameter. A temperature-volume fraction ($T - \phi$) phase diagram of a HS system (Fig. 1.1a) features discrete fluid, crystal and fluid-crystal coexistence phases.

In spite of its apparent simplicity, a seminal publication by Pusey and van Megen [38] proved the model to be able to account for phase behaviours observed experimentally for polymethylmethacrylate (PMMA) colloids, providing another strong indication that aspects of atomic systems can be applied to colloidal ones and vice versa.

Introduction of attractive forces to account for the gas-liquid phase transition

Being a fundamentally important concept in physics, the hard-sphere model alone is nevertheless unable to describe the gas-liquid phase transition observed in many experimental systems since this phenomenon requires interparticle attraction. A first successful description of accounting for attraction-induced gas-liquid transitions was performed by van der Waals in 1873 [39–41]. Van der Waals' approach of introducing two correcting terms into the ideal gas equation of state is sketched in the following for the case of a HS fluid.

As in the HS model presented above, it is assumed that the particles considered cannot overlap (to account for real systems, this is justified by Pauli's principle), which reduces their effective molar volume by b, the first correcting term [40, 41]. In addition to b, a term accounting for long-range attractions between the particles and leading to an increase in the compressibility of the fluid when its pressure is increased at constant temperature. The effective pressure inside the HS fluid is thus greater than the external one by a term p_{add}. At very high pressures, the HS fluid cannot be compressed further and short-range attractions between its particles start to play a role.

These two correcting terms accounting for both attractive and repulsive intermolecular interactions were used by van der Waals to modify the ideal gas equation of state as follows:

$$(p + p_{add})(V - b) = RT \Leftrightarrow V^3 - \left(b + \frac{RT}{p}V^2 + \frac{a}{p}V - \frac{ab}{p}\right) = 0 \tag{1.6}$$

where $p_{add} = a/v^2$ with a constant a (for details see Ref. 41). Assuming impen-

etrable spherical particles the minimum distance between the centres of which is $2 \cdot \sigma/2 = \sigma$ and the excluded volume between two particles is therefore $\frac{4}{3}\pi(\sigma)^3 = 8V_{particle}$. The excluded volume of one particle is thus equal to $4V_{particle}$. Therefore, $b = N_A \cdot 4V_{particle}$ [40].

Solving Eqn. 1.6 for p yields the **van der Waals equation of state (e.o.s.)** [41]

$$p = \frac{RT}{V-b} - \frac{a}{V^2}. \tag{1.7}$$

From the van der Waals e.o.s., the compressibility factor Z_{HS} of a pure HS fluid can be obtained. Z_{HS} can be described as a series expansion of the volume of the fluid or approximated by a simpler term:

$$Z_{HS} = 1 + \frac{B}{V} + \frac{C}{V^2} + \cdots = \frac{p}{\rho k_B T} \tag{1.8}$$

with a particle density $\rho = N/V$. Note that a limitation of the series to its second term does not account for the vapour-liquid transition; truncating it after the third term, on the other hand, does not allow for an accurate description of the liquid-vapour transition [42], implying different shortcomings of this e.o.s. Therefore, multiple modified versions of the van der Waals e.o.s. have been established [37, 42]. An approach getting particularly close to the "real" phase behaviour of HS fluids observed in computer simulations was pioneered by Carnahan and Starling [36, 37, 42, 43] based on a solution of the Percus-Yevick equation for hard spheres. In this case, Z_{HS} is given by

$$Z_{HS} = \frac{1 + \phi + \phi^2 - \phi^3}{(1-\phi)^3} \tag{1.9}$$

where $\phi = \frac{4}{3}\pi\frac{\sigma}{2}^3\rho$ is the packing density of the hard sphere fluid considered. A complementation of Eqn. 1.9 by the attractive van der Waals term described above yields a Z_{HS} form equivalent to that obtained from the van der Waals equation [42] as can be shown by, e.g. density functional theory (DFT) [36]. Therefore, the van der Waals e.o.s. is used in the following in order to describe how the gas-liquid transition can be rationalised.

The van der Waals e.o.s. (Eqn. 1.7) can be rewritten in its cubic form

$$\left(\frac{\partial p}{\partial V}\right)_T = -\frac{RT}{(V-b)^2} + \frac{2a}{V^3}. \tag{1.10}$$

At high T the isotherms will therefore have a negative slope regardless of the molar volume. At lower T, the first term will dominate for low and high V whereas at intermediate V the second term will determine the sign of the isotherm. The isotherms will therefore have one minimum and one maximum each, which means that below a critical molar volume v_{crit} the isotherms will show an unphysical increase in v with increasing p (van der Waals loops) [40]. In real systems, macro-

scopic observations below this critical volume show that the gas condenses into a liquid. The van der Waals approach is thus no longer valid when gas and liquid phases coexist [41]. In the unstable states, the so-called Maxwell construction [36, 42, 44] is applied, reflecting the fact that the pressures and chemical potentials of the coexisting phases must be equal [40, 42]. Details on the equal-area approach are given in Ref. 45. Points determined in the framework of this approach are connected *via* horizontal lines. All endpoints of these horizontal tangents give rise to the so-called **coexistence curve** or **binodal**; the points corresponding to minima or maxima of the van der Waals loops form the **spinodal** [36]. Systems located inside the spinodal are unstable and phase-separate immediately. This process is referred to as spinodal decomposition (see Section 1.2.2). The region between the binodal and the spinodal is referred to as metastable, i.e. a certain energy barrier prevents the systems located in this region from immediate phase separation [46]. Binodal and spinodal lines coincide at the critical point characterised by, *inter alia*, the critical temperature T_c and the fact that the two derivatives of the pressure with respect to volume

$$\left(\frac{\partial p}{\partial V}\right)_{T=T_c} \tag{1.11}$$

and

$$\left(\frac{\partial^2 p}{\partial V^2}\right)_{T=T_c} \tag{1.12}$$

vanish identically [40].

The addition of a long-range attraction term to the hard sphere system as described above thus results in a much more complex phase behaviour than in the case of pure hard-sphere repulsion. In real-life experimental systems, long-range attractions are due to random fluctuations of electron density which subsequently give rise to mutually interacting dipoles. These interactions are summarised under the term "van der Waals interactions" and show a power law-type dependence on the inteparticle distance [27]. The overall combination of a long-range attraction and a short-range repulsion — which, as described above, stems from electronic repulsion of particle orbitals — can be described *via* the Lennard-Jones (LJ) potential

$$u_{LJ}(r) = u_0[(r_0/r)^{12} - 2(r_0/r)^6] \tag{1.13}$$

with r_0 being the interparticle distance at which the potential energy of their interaction is minimised and u_0 the energy value at this distance [47]. The first term corresponds to the interparticle repulsion and increases steeply with decreasing interparticle distance whereas the second term corresponds to the attractive interactions [47]. In Monte Carlo simulations, this potential is often cut off at a certain interparticle distance $r = R^c$ which is typically equal to 2.5σ [48]. More-

over, to avoid the delta function at $r = R^c$ in molecular dynamics simulations, a truncated and shifted (ts) version of the LJ potential,

$$u_{LJ,ts}(r) = \begin{cases} u(r) - u(R^c) & \text{for } r \leq R^c \\ 0 & \text{for } r > R^c \end{cases} \tag{1.14}$$

is often used [48].

In a colloidal phase diagram, the effects of a combination of a short-range repulsion and a long-range attraction are reflected in the presence of many different regions of the diagram — homogeneous fluid, gas, liquid, crystalline phases and coexistence thereof (Fig. 1.1 b). The phase diagram moreover features a triple point at which gas, liquid and crystals can coexist as well as a critical point below (upper critical solution temperature, UCST) or above (lower critical solution temperature, LCST) which the homogeneous fluid can phase-separate into a liquid and a gas phase. A more detailed discussion of both phenomena is found in Section 2.2. In colloidal systems, the homogeneous fluid can be thought of as being analogous to a homogeneous suspension whereas the gas and liquid phase correspond to colloid-poor ("dilute") and colloid-rich ("dense") phases, respectively, resulting from phase separation. This is particularly relevant in the case of short-ranged attraction as discussed below.

Short-ranged attraction and metastable LLPS

If the attraction in a (colloidal) system is not long-ranged, but short-ranged (e.g. $\sim 1/6$ of the particle diameter [49]) as in the case of the depletion colloid-polymer system studied by Gast *et al.*, the corresponding phase diagram changes shows a metastable liquid-liquid coexistence region below the critical point (Fig. 1.1 c), thus differing strongly from the case where only long-ranged attractions are considered. This liquid-liquid coexistence region therefore allows to rationalise the phase separation observed by Gast *et al.* [31, 33]. Detailed theoretical background for this attraction-range dependent appearance of the metastable liquid-liquid region was provided by Lomba and Almarza [50] as well as Hagen and Frenkel [49] using grand ensemble Monte Carlo simulations in hard-core Yukawa systems where the short-range interaction potential is given by [49]

$$u(r) = \begin{cases} \infty & \text{for } r < \sigma \\ -\epsilon \frac{\exp[\kappa\sigma(1-r/\sigma)]}{r/\sigma} & \text{for } r \geq \sigma. \end{cases} \tag{1.15}$$

Here, ϵ is the potential well depth, κ^{-1} determines the range of the attractive part and σ represents the diameter of the particles in question. For $\kappa > 7$, the critical point of the system is located below the sublimation line; thus, a stable liquid phase no longer exists [49]. Moreover, when the attraction range is shorter than roughly 30% of the hard-core particle radius, freezing prevents fluid-fluid separation [51].

In spite of the importance of short-range attractions, however, the long-range ones should not be ignored in particular when investigating gelation and crystallisation [51]. It is in particular the location of the percolation line that is influenced by the strength of the long-range attraction. With weak van der Waals forces, percolation occurs before the system can be brought to the metastable critical point; a liquid-liquid phase separation is therefore prevented. As the interaction strength increases, the metastable critical point is found outside the percolation regime. Very strong long-range attractions can lead to phase separation even in the absence of short-range attractive forces [51].

In an attempt to find a generalised approach to systems with different interaction ranges, Noro and Frenkel [52] formulated an extension of the van der Waals law of corresponding states (ELCS). In particular, the authors argue that the reduced second virial coefficient $B_2^* = B_2/\frac{2}{3}\pi\sigma_{eff}$ (σ_{eff} being the effective hard core diameter of the repulsive part of the potential in question) can be used to evaluate the effective attractive range of a system in question. Moreover, this approach allows for a prediction of the topology of the corresponding phase diagram. In fact, the values of the second virial coefficient have been shown to be reliable predictors for conditions favouring protein crystallisation [53]. The results from the latter study were further corroborated by Rosenbaum and colleagues [54] who demonstrated a striking similarity between the crystallisation of hard spheres and proteins. These results again indicate the complementarity between colloidal and protein-based systems and the fact that colloidal phase diagrams as the ones described above can indeed be used to describe the phase behaviour of proteins [55].

A first quantitative description of a metastable liquid-liquid phase separation in a protein-salt system (in this case, an aqueous lysozyme-NaCl mixture with an upper critical point) was published by Ishimoto and Tanaka in 1977 [56]. In this publication, the authors rationalised their observations using mean-field theory. Later on, Muschol and Rosenberger [57] applied the knowledge on the influence of short-range attractions on protein phase behaviour to explain LLPS, precipitation and crystallisation in supersaturated lysozyme solutions. Further protein systems in which liquid-liquid phase separation has been observed are, for example, crystallins [58–61], hemoglobin [62–64], lysozyme [57, 65] and elastin-derived polypeptides [26, 66]. The studies on crystallins moreover led to the development of a Monte Carlo simulation technique capable of capturing short-ranged attractions not accounted for in previous mean-field studies and indicating the importance of anisotropy in protein-protein interactions [67], a feature of major importance in proteins due to their heterogeneous charge and hydrophobicity distribution. Interestingly, theoretical work by Kern and Frenkel [68] showed that in systems with anisotropic (patchy) interactions neither one single value of the respective virial coefficient nor the knowledge of the attractive patch fraction are enough to describe the critical point of liquid-liquid phase separation. In addition to these two parameters, the critical temperature of such systems appears to be determined by the mutual orientation and arrangement of said patches whereas the interaction

range plays a less important role [68].

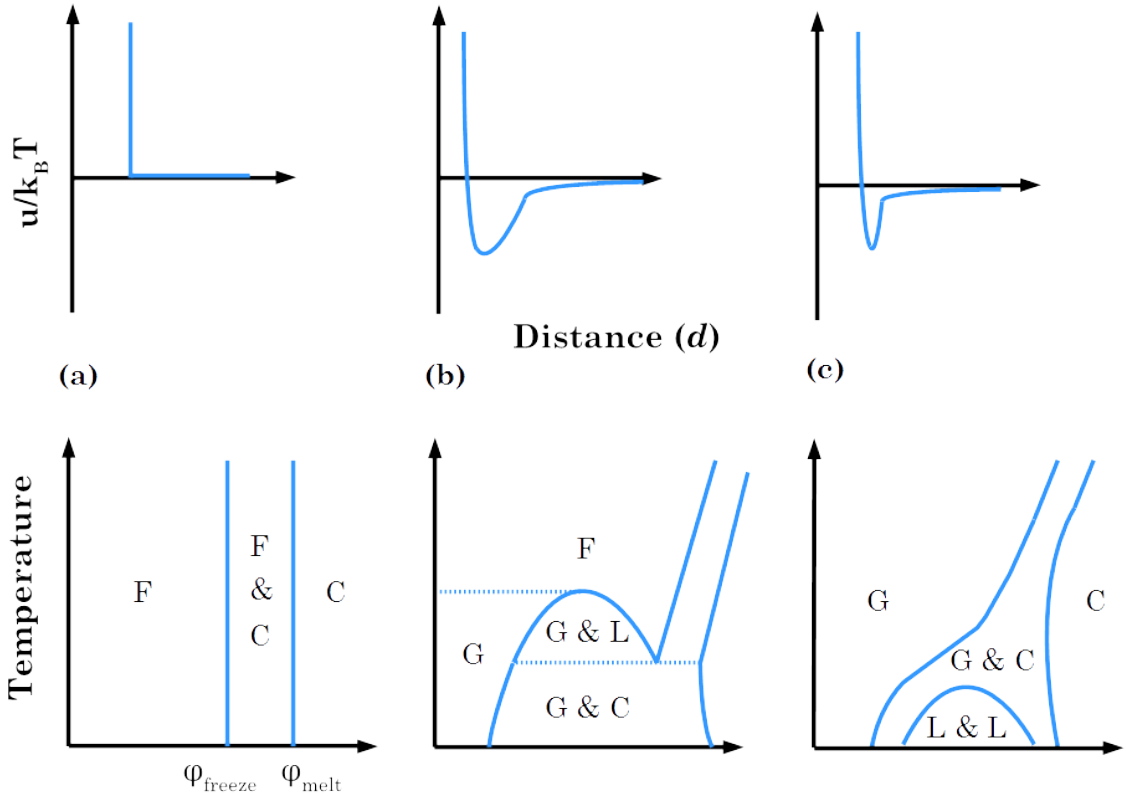

Figure 1.1: *Phase diagrams of systems with varying attraction ranges (bottom panel) with corresponding pair potentials (top panel). (a), purely hard sphere interaction; (b) long-ranged attraction and (c) short-ranged attraction. F, fluid; C, crystalline; G, gas; L, liquid. Image reproduced from Refs. [55] and [69]. See text for details.*

Spinodal decomposition as a pathway towards LLPS

As discussed above, metastable LLPS is a major feature of colloidal systems with short-range attractions. In the following, spinodal decomposition as a possible pathway leading towards LLPS is presented and its mathematical rationalisation is presented.

The metastable and unstable regions (discussed in Section 1.2.2) of a generic fluid (here, a binary mixture is considered) differ with respect to how density or concentration fluctuations propagate in the respective regions. When located in its metastable region, the system can withstand small density fluctuations. A large change is thus required to trigger phase separation, i.e. a nucleus enriched in one of the two components needs to be generated. This process is therefore referred to as nucleation and can be heterogeneous or homogeneous [46]. Classical nucleation theory (CNT) provides a way to quantify the change in the free energy ΔG of the

system upon formation of a (spherical) nucleus as a function of the radius r of the latter [70]:

$$\Delta G(r) = \frac{\frac{4}{3}\pi r^3}{v} k_B T \; lnS + 4\pi r^2 \gamma \tag{1.16}$$

where S is the supersaturation of the system, v is the molar volume of a growth unit and γ is the surface tension of the nucleus [70].

In the unstable region inside the spinodal, however, density fluctuations are amplified along the system in a homogeneous manner *via* a process referred to a spinodal decomposition (SD). To understand the mathematical description of SD (based on Ref. 42), a generic binary mixture containing components A and B will be considered again in the following. Prior to the onset of SD, the mixture is homogeneous. The concentration c of component A is equal to $n_A/(n_A + n_B)$ with n_A, n_B being the numbers of particles of species A and B, respectively.

Let c_0 represent the global concentration of component A in the binary mixture considered here. The free energy f per unit volume can be expanded into a series around c_0

$$f(c) = f(c_0) + (c - c_0)\Big(\frac{\partial f}{\partial c}\Big)_{c_0} + \frac{1}{2}(c - c_0)^2\Big(\frac{\partial^2 f}{\partial c^2}\Big)_{c_0} + \cdots \tag{1.17}$$

Assuming a low amplitude of the density fluctuations considered, the free energy of formation of the emerging phase ΔF is equal to

$$\Delta F = \int \Big[\frac{1}{2}\Big(\frac{\partial^2 f}{\partial c^2}\Big)_{c_0}(c - c_0)^2 + \frac{1}{2}K|\nabla c|^2\Big] dV \tag{1.18}$$

where $K > 0$ is the inhomogeneity term. Terms higher than the second order are neglected here. The system in question will remain stable in its homogeneous state for $(\partial^2 f/\partial c^2) > 0$ since this will lead to $\Delta F > 0$. In the opposite case, the inhomogeneous phase is stable and SD occurs. The time-dependent concentration fluctuation $\delta c(r, t)$ leading to SD can be Fourier-transformed to

$$\delta c(r, t) = \int \delta c(k, t) e^{ikr} dr. \tag{1.19}$$

The density fluctuation is assumed to be of the form $\delta c_k = A \; cos(kx)$ where A is its amplitude. ΔF can then be expressed as $\int \Delta F_k dk = \int \Delta F_k e^{ikr} dr$. Assuming periodic boundary conditions with a period of 2π and applying the integral to Eqn. 1.18 (the integral of $cos^2(kx)$ over the whole volume yields $\frac{1}{2}$) leads to the expression

$$\Delta F_k = \frac{1}{4} V A^2 \Big[\Big(\frac{\partial^2 f}{\partial c^2}\Big)_{c_0} + Kk^2\Big]. \tag{1.20}$$

Eqn. 1.20 shows that within the thermodynamically unstable region where $(\frac{\partial^2 f}{\partial c^2}) < 0$, density fluctuations with a wave vector larger than a certain critical wave vector

($k > k_c$ with $k_c^2 = \frac{-1}{K}\left(\frac{\partial^2 f}{\partial c^2}\right)_{c_0}$) or, in real space, with a wavelength $\lambda_c = 2\pi/k_c$ will increase ΔF_k, favouring homogeneity. In the opposite case ($k < k_c$), phase separation *via* SD will occur preferentially. Note that long-wavelength fluctuations imply the diffusion of molecules over long distances and short-wavelength ones generate a large interfacial area. A certain intermediate wavelength of concentration fluctuations will therefore dominate the process of SD [46].

The fact that $(\frac{\partial^2 f}{\partial c^2}) < 0$ in the unstable region has a very important implication in the context of SD, that is, uphill diffusion [46]. This term describes the seemingly counterintuitive phenomenon of diffusion from regions of lower concentrations to those with higher concentration. The reason for this unusual behaviour is the relation between the chemical potential μ and $(\frac{\partial f}{\partial c})$. Since $(\frac{\partial^2 f}{\partial c^2}) < 0$ in the spinodal region, the sign of the gradient of the chemical potential is opposite to that of the concentration gradient. This leads to uphill diffusion [46].
Overall, it can be shown [42] that the time-dependent evolution of the concentration can be expressed *via* the Cahn-Hilliard equation

$$\frac{\partial \delta c(r,t)}{\partial \delta t} = M\nabla^2\Big[\frac{\partial f}{\partial c} - K\nabla^2 c(r,t)\Big] \tag{1.21}$$

or, in its linearised form

$$\frac{\partial \delta c(r,t)}{\partial t} = M\nabla^2\Big[\Big(\frac{\partial^2 f}{\partial c^2}\Big)_{c_0} - K\nabla^2\Big]\delta c(r,t). \tag{1.22}$$

Here, $M = M_0/N$ with M_0, a constant transfer coefficient, being related to the concentration current J *via* $J = -M_0\nabla\mu$. The Fourier transform of $\delta c(r,t)$ (Eqn. 1.18) introduced earlier can be used to solve Eqn. 1.22 if it is assumed that concentration fluctuations relax as

$$\delta c(k,t) = \delta c(k,0)e^{-\omega_k t} \tag{1.23}$$

with ω_k being a damping coefficient. Combining Eqns. 1.23 and 1.22, ω_k can be defined as

$$\omega_k = Mk^2\Big[\Big(\frac{\partial^2 f}{\partial c^2}\Big)_{c_0} + Kk^2\Big] = MKk^2[k^2 - k_c^2] \tag{1.24}$$

Thus, in the unstable region of the phase diagram in question, with $k < k_c$ and $\omega_k < 0$, the respective concentration fluctuations are not damped and therefore increase with time. This leads to SD.

Throughout phase separation in the generic binary A-B mixture — regardless of whether phase separation proceeds by nucleation or SD — domains of component A will form inside a matrix of component B (or vice versa). Driven by a decrease in interfacial energy, said domains will then grow [46]. A prominent model of such a growth mechanism is Ostwald ripening. This model is based on the assumption that few polydisperse domains are present. The solubility of the

phase present in the domains being higher in the vicinity of small domains than it is near larger ones, the smaller domains dissolve and are consumed by the larger ones [46]. Calculations by Lifshitz and Slyozov [71] show that, as a result of this process, the domain size (or, as is sometimes phrased alternatively, the correlation or characteristic length, ξ, of a given system) grows in a manner proportional to $t^{1/3}$ in the late stage of phase separation.

In the present work, the growth of the correlation length of dense phases obtained *via* phase separation of BSA-$HoCl_3$/$LaCl_3$ mixtures with varying $HoCl_3$/$LaCl_3$ ratios is investigated using ultra-small angle X-ray scattering. The corresponding results are discussed in Chapter 7.

Chapter 2

Protein-cation interactions and resulting phase behaviour

2.1 Protein-cation interactions in a biological context

Typical intracellular concentrations of Na^+ and K^+ are 12 and 140 mM, respectively [1], and these ions are of vital importance to, *inter alia*, maintaining a physiological osmotic pressure in living tissues as well as signal transduction in neurons. With proteins featuring highly heterogeneous surface charge patterns, it is clear that they will engage in charge-mediated interactions with ions surrounding them. A rather general interaction type is a simple Coulomb attraction of oppositely charged ions to the protein surface. More specific interactions include the binding of ions to specific protein sites. As an example, bovine serum albumin can bind Mg^{2+} and Ca^{2+} cations and transport them to various destinations in the organism [72]. The interactions between proteins and ions can also go beyond transient transport-related associations. In several cases, the biological activity of proteins strongly depends on the presence of metal ions in their active centres. When bound covalently to residues in their active centres, the ions are referred to as prosthetic groups. A case in point is hemoglobin, the oxygen transporting activity of which requires a Fe cation to be bound to its prosthetic heme group consisting of a porphyrin-based organic structure [1]. Further ions of high physiological relevance for proteins include Zn^{2+} [1, 73], Ca^{2+}[1] and I^- [74].

2.2 Protein phase behaviour induced by multivalent cations

2.2.1 Protein-multivalent cation interactions

Given the obvious importance of protein-ion interactions for various physiological aspects, much effort has been invested into studying these interactions from biological, chemical and physical points of view. A necessary step to investigate ion-dependent proteins was to determine and characterise the ion binding sites of said proteins. Complexes of lanthanide ions and some organic ligands possess several

favourable fluorescence properties such as long fluorescence lifetimes, strong Stokes shifts and distinct emission peaks [75]. Depending on the choice of the ligand, the fluorescence can be enhanced [76], which makes lanthanides valuable structural probes to investigate cation binding sites of proteins. As an example, Harris and co-workers [77–81] examined the binding of various non-ferrous cations to human transferrin and lactoferrin, notably including the lanthanide cations Lu^{3+}, Er^{3+}, Ho^{3+}, Tb^{3+}, Gd^{3+}, Sm^{3+}, Nd^{3+} and Pr^{3+}. Amongst other results, the authors report a decrease in the amount of cations bound with increasing cation radius [79] — an aspect of strong interest from the perspective of the present work. Further insights into the thermodynamics of multivalent cation-protein interactions from literature are summarised in Chapter 6. Detailed information on thermodynamic and hydration properties of Ln cations is given in Section 3.2.

In addition to these cation-protein interactions of strong relevance on a biological and structural analysis level, multivalent cations can be used as thermodynamic agents inducing short-ranged attractions in protein systems. Starting from 2008, Zhang and colleagues [8–14, 82–90] documented an intriguing variety of phase behaviours in systems of negatively charged, globular proteins in the presence of multivalent cations such as Y^{3+}. The phase behaviours mentioned include clustering, crystallisation, reentrant condensation as well as a liquid-liquid phase separation with a lower critical solution temperature (LCST-LLPS). A detailed description of these phase behaviours and the mechanisms behind them will be given in the following.

2.2.2 Reentrant condensation

The overall basis for the rich phase diagram of negatively charged proteins in the presence of multivalent salts summarised above is the electrostatic interaction between positively charged cations (e.g. Y^{3+}) and negatively charged protein surface groups, mostly carboxyls, on the surface of, e.g., bovine serum albumin. At a certain protein concentration c_p and a low salt concentration c_s, the system is a homogeneous liquid (regime I). A continuous increase in c_s while keeping c_p constant decreases the negative surface charge of the protein and eventually condenses the protein molecules in solution into cluster-like structures. This condensed state is referred to as regime II the entrance into which is marked by a critical salt concentration, c^*. A further increase of salt concentration leads to overcharging of the protein and the clusters redissolve upon surpassing a second critical salt concentration, c^{**} (regime III). The entire phenomenon is therefore also referred to as "reentrant condensation" and was first observed in systems consisting of DNA or other polyelectrolytes and multivalent ions [91, 92].

Under certain conditions, a liquid-liquid phase separation (LLPS) into a protein-poor and a protein-rich phase can occur inside the condensed regime. These findings again reflect the importance of the short-range (e.g. depletion) interactions described in Section 1.2.

2.2.3 LCST-LLPS *via* spinodal decomposition

Notably, LLPS in systems of BSA and multivalent cations occurs upon temperature increase (LCST-LLPS). This phenomenon is traced back to entropic contributions by dehydration of both the yttrium cations and the carboxyl groups binding them [13] and is described in more detail in Section 5. Lower and upper critical solution temperatures have already been known for a long time, in particular in mixtures of small organic molecules. In the case of UCST (e.g. mixtures of hexane/nitrobenzene or palladium/palladium hydride) entropic contributions enhance mixing at high temperatures [40]. Typical LCST systems are water/triethylamine mixtures [40] or aqueous poly(N-isopropylacrylamide) (PNIPAM) solutions [93]. In the case of PNIPAM, the LCST behaviour can be explained as follows: at $T <$ LCST, water molecules form ordered clathrate-like structures around hydrophobic regions of the polymer. Additionally, hydrogen bonds are formed between water molecules and hydrophilic groups of PNIPAM. At higher temperatures, entropic contributions dominate the exothermic formation of hydrogen bonds and the ordered water structures are released into the bulk. The PNIPAM molecules thus undergo a so-called hydrophobic collapse and are no longer miscible with their aqueous surroundings [93, 94], resulting in phase separation into a polymer-rich and a polymer-poor phase.

The LCST-LLPS of BSA-YCl_3 systems has been shown to occur *via* spinodal decomposition and the kinetics of the latter have been studied using ultra small-angle X-ray (USAXS) and very small-angle neutron scattering (VSANS) [14]. It was found that the characteristic length ξ of the respective systems grows as a function of time t as $\xi \sim t^{1/3}$ for $T < 45$ °C. For $T > 45$ °C and at $t > 30$ s, the growth of ξ slows down. At even higher temperatures, arrest is observed as indicated by constant values of ξ until protein denaturing interferes with further investigations above 55 °C. In the present thesis, this study was extended to mixtures of BSA and weakly and strongly interacting cations (cf. Chapter 7).

2.2.4 A patchy particle model rationalising protein-multivalent cation interactions

A theoretical approach to rationalise the interaction between proteins and multivalent cations as well as the protein phase behaviours induced thereby has been developed by Roosen-Runge and co-workers [95]. The approach is based on the representation of proteins as so-called "patchy particles" [68, 96, 97] and describes the protein-protein interaction using a combination of a hard sphere repulsion V_{12} and a square-well attraction V_{pp} (here, i and j denote the indices of the patches considered):

$$V(1,2) = V_{HS}(R_{12}) + \sum_{i=1}^{m}\sum_{j=1}^{m} V_{pp}(r_{12}^{ij}) \tag{2.1}$$

where

$$V_{pp}(r_{12}^{ij}) = \begin{cases} -\epsilon_{pp} \text{ for } r_{12}^{ij} < r_c \\ 0 \quad\quad \text{for } r_{12}^{ij} \geq r_c \end{cases} \tag{2.2}$$

In the case of BSA and YCl_3, the patches in the model correspond to certain types of arrangements of carboxylic groups which can coordinate multivalent ions (in this case, Y^{3+}). When hosting a cation, a patch is considered "occupied". A sterically favourable orientation with respect to the unoccupied patch on another protein molecule can lead to the formation of a so-called cation bridge between two protein molecules. The protein-protein interaction energy ϵ_{pp} is a function of the average patch occupancy (Θ) by Y^{3+}

$$\epsilon_{pp} = \epsilon_{uu}(1-\Theta)^2 + 2\epsilon_{uo}\Theta(1-\Theta) + \epsilon_{oo}\Theta^2 \tag{2.3}$$

with the indices *uu*, *oo* and *uo* referring to the interaction between two unoccupied, two occupied or an unoccupied and an occupied patches, respectively, on two protein molecules. Together with results from small-angle scattering and X-ray diffraction experiments revealing a cation-induced short-range interprotein attraction between unoccupied and occupied patches on the protein surface [10, 12, 82], these theoretical assumptions are thus able to account for cluster formation, reentrant condensation and LLPS. Notably, the cation-mediated bridging of protein molecules can promote the nucleation and growth of crystal lattices in systems of β-lactoglobulin (BLG) and multivalent salts [82], thus allowing for a controlled generation of crystals which is considered a major obstacle in protein crystallography. Intriguingly, the exact location of the respective crystallisation samples in the phase diagram determines their crystallisation pathways. While classical nucleation dominates near c^* [86], a two-step mechanism can be observed in the vicinity of c^{**} [87] in the BLG-multivalent salt systems mentioned.

Part II

Materials and experimental methods

Chapter 3

Materials

3.1 Bovine serum albumin

The protein used in this thesis is bovine serum albumin (BSA) with a molecular weight of 67 kDa [72, 98] and an isoelectric point of 4.7 [99]. Serum albumins are abundant in the blood of mammals and are mostly responsible for the transport of fatty acids or cations such as Mg^{2+} and Ca^{2+} and maintaining the osmotic pressure of blood [72].

BSA (heat shock fraction, catalogue number A7906) with an indicated purity of $\geq 98\%$ was purchased from Sigma Aldrich (now Merck, Darmstadt, Germany) and used as received. Protein stock solutions were prepared by dissolving the required mass of BSA in ultrapure degassed water (18.2 MΩ; Merck Millipore, Darmstadt, Germany). The exact protein concentration was then measured by UV spectroscopy (see Section 4.6).

The BSA concentrations used for samples studied by visual inspection, temperature-dependent UV absorbance and SAXS (cf. Section 6) were 80 mg/ml or 85 mg/ml which, assuming a partial specific volume of 0.735 ml/g [100], corresponds to a volume fraction ϕ of 0.0588 or 0.0625, respectively. The average particle-particle distance in these samples is roughly 10.5 nm based on the SAXS correlation peak of an aqueous BSA solution of pure BSA. Assuming an effective sphere, the average particle size (hydrodynamic radius) of a BSA monomer is equal to 3.62 nm [101].

High-concentration samples prepared for USAXS and EXAFS measurements (initial protein concentration = 175 mg/ml) correspond to $\phi = 0.129$ (cf. Chapters 7 and 8). The dense phases of these samples were used for USAXS and VSANS measurements and have concentrations of $\sim$ 200-300 mg/ml (ϕ = 0.149-0.221).

The lowest BSA concentrations (1 mg/ml) were used for ζ potential and isothermal titration calorimetry measurements (cf. Sections 5 and 6). Here, the volume fraction is equal to $7.35 \cdot 10^{-4}$. This low volume fraction allowed to study cation adsorption to BSA while ignoring cation-mediated protein-protein interactions.

3.2 Yttrium and lanthanide chlorides

In this thesis, trivalent chlorides of yttrium (Y) and lanthanides (Ln) are used in order to induce and tune phase transitions of BSA. Given the occasionally

confusing variety of lanthanide nomenclature, a brief explanation thereof is given here. The elements following Ca (electron configuration [Ar]$4s^2$) and located in groups 3-12 are the *d block elements* [102]. The term *transition elements* is used to describe those d block elements the d orbitals of which are not fully occupied [103]. The 14 elements located between Ba and Hf are called *lanthanides* [104]. Therefore, the salts $HoCl_3$ and $LaCl_3$ used in this thesis are lanthanide chlorides; YCl_3 is a d block element chloride. Note that the term "rare earths" which is also used occasionally can be considered unsuitable due to the fact that the elements it is used for are neither earths (i.e., not oxides) nor actually rare [105].

Based on previous experiments [11, 12, 82], we assume that it is the respective rare earth cations which induce the BSA phase behaviours studied here by binding to negatively charged protein surface residues and introducing a short-range attraction between protein molecules. The chloride counterions of the yttrium and lanthanide cations are not a topic considered in this thesis. A detailed analysis of the influence that different counteranions of multivalent cations have on phase transitions of BSA can be found in Ref. 106.

One of the most obvious properties of lanthanides capable of influencing the phase behaviour of proteins in solution are their respective radii. Shannon [107] established an exhaustive overview of crystal and ionic radii for most elements. Importantly, in the presence of co-solutes interacting with the cations, the coordination number (CN) of each cation influences its effective radius and thus needs to be considered as well. A revised summary of lanthanide radii, taking into account their respective CNs, was published by D'Angelo *et al.* [108]. Given that the experiments performed in the scope of this thesis involve cations in solution, the cation radii considered in this thesis are those summarised in Table 3.1.

Table 3.1: *Ionic radii [108] and coordination numbers [108] of the lanthanide cations the trichlorides of which are used in this thesis. The radius of Y^{3+} is obtained from Ref. 107 and its coordination number from Ref. 109. Note that although strictly speaking, Y is not a lanthanide, it is nevertheless often discussed in the context of lanthanides due to shared chemical features [110].*

Cation	**Ho^{3+}**	**Y^{3+}**	**Gd^{3+}**	**Ce^{3+}**	**La^{3+}**
Coordination number	8.9	8.0	9.0	9.0	9.1
Ionic radius (Å)	1.055	1.019	1.105	1.220	1.250

Due to their similarity to actinidies, a series of elements vastly important in the context of nuclear energy [111] and to their use in radiochemical labelling [112], the properties of lanthanides have been of significant interest in both applied and theoretical science. In the following, a brief overview on some of the results obtained so far is given with a special focus on thermodynamic and hydration properties. A detailed discussion on the interactions between lanthanides and selected proteins

can be found in Chapter 6.

An extensive data set on the coordination — here used as a synonym for hydration — of lanthanides was obtained using X-ray diffraction by Habenschuss and Spedding [113–115]. The authors concluded that the CN — in this case, the number of water molecules surrounding in the primary hydration shell of the respective cations — varies from 9 for La^{3+}, Pr^{3+} and Nd^{3+} to 8 for Tb^{3+}-Lu^{3+}. Between Nd^{3+} and Tb^{3+}, an intermediate CN representing fractions of the hydrated Ln^{3+} population with CN = 8 or 9 [116] is observed. Similar findings were obtained by Cossy *et al.* [117] using neutron scattering.

A recent computational study by Zhang *et al.* [118] confirmed this result and traced the change from CN = 9 to CN = 8 back to a change of preferred water structuring around the cations due to an increase of water-water repulsion and an increasingly unstable capping water molecule.

To further characterise the transition from CN=8 to CN=9, the exchange frequency (EF; number of water exchanges per ns) of water molecules between the first hydration shell and bulk water was studied by Duvail *et al.* [116] using molecular dynamics (MD) simulations with explicit polarisation. This study reveals a highly non-monotonic behaviour of the EF along the lanthanide cation series. Starting with EF = 0 for La^{3+}, the number increases up to EF = 25 for Tb^{3+} (Persson and co-workers identify Ho^{3+} as the element with the strongest hydration structure change [119]) and then decreases back to almost 0 at Lu^{3+}. Duvail *et al.* propose an interconversion between different water structures along the lanthanides — La^{3+} features a tricapped trigonal prism consisting of 9 water molecules (6 making up the outer and 3 the inner triangle). With decreasing cation radii and polarisabilities, the inner-shell water molecules repel each other more strongly, which leads to a decrease in cation-water affinity and a decreasing CN. The heaviest Ln^{3+} then show an equilibrium between a square antiprism and a bicapped trigonal prism (BTP) with CN = 8 [116].

Given that the cation-protein and cation-induced protein interactions studied in this thesis are entropy-driven, thermodynamics of lanthanide interaction with both water and ligands are of particular interest. Hinchey and Cobble [120] investigated the hydration thermodynamics of the lanthanide series. Their findings indicate an increasingly negative free energy and enthalpy of solution with increasing atomic number Z. The respective entropic terms increase as well, thus pointing towards an important role of entropy in Ln hydration. This finding was corroborated by computational studies by Ciupka *et al.* [121]. Interestingly, Hinchey and Cobble also found the ionic entropies to increase linearly as a function of the respective inverse ionic radii [120] after eliminating the electronic entropy term from the corresponding calculations. Choppin [122] furthermore investigated complex formation of lanthanides and different ligands. Again, an increase in formation entropy was observed with increasing Z. Notably, this study includes ethylenediaminetetraacetic acid (EDTA) and glycine, both of which are of relevance for this thesis due to their chelating carboxyl groups. Both Habenschuss and Spedding and Ikeda *et al.* [109] provide experimental and computational evidence that the

probability of the formation of an inner-sphere chloride complex is unlikely. According to Ikeda *et al.*, the energy barrier for the formation of such a complex is around 5-10 kcal/mol [109]. According to a lanthanide concentration-dependent quantum chemical and MD simulation study performed by Beuchat *et al.* [123], however, Cl^- can get closer to the cation in the case of Gd^{3+} and Er^{3+}.

As a general caveat, it should be kept in mind that simulations and calculations of lanthandies and their properties can encounter difficulties due to non-negligible relativistic effects [118] caused by strong shielding of the nuclear charge [124], a large number of electrons and incomplete 4f electron orbital occupation [118]. Nevertheless, the above examples show that a large number of such studies shows good reproducibility and consistency.

All trivalent lanthanide and yttrium chlorides used in this thesis were purchased from Sigma Aldrich (now Merck, Damstadt, Germany) as anhydrous powder or beads. The respective catalogue numbers were 450901 ($HoCl_3$), 449830 ($LaCl_3$) and 451363 (YCl_3). Their purities were indicated by the manufacturer as 99.9-99.99% and the powders were used without further purification. Stock solutions were made by weighing the appropriate mass of salt into a volumetric flask and adjusting the water (ultrapure [18.2 MΩ] degassed MilliQ [Merck Millipore, Darmstadt, Germany]) volume according to the desired stock concentration. When not in use, the salts were stored in vacuum due to their hygroscopy.

Chapter 4

Experimental methods

4.1 Small-angle scattering

In this thesis, small-angle scattering was used to characterise the interactions multivalent salts induce in aqueous BSA solutions. This section first provides a general overview of the thermodynamic properties investigated. The setup of small-angle scattering experiments is discussed afterwards. Finally, the deduction of thermodynamic properties of the sample from the scattering signal is explained.

4.1.1 Thermodynamic quantities obtained from small-angle scattering experiments

The term "scattering" describes the deflection of waves (e.g. photons or neutrons) by matter. In soft matter research, scattering experiments are used in order to investigate samples such as surfaces, amorphous structures, powders, crystalline structures or colloidal dispersions. The unique characteristic of scattering methods is that they allow for deduction of both structural and thermodynamic properties of samples, the latter implying that scattering provides information about a time and space ensemble average of the system in question. In this thesis, the scattering method of choice is small-angle scattering (SAS) applied to protein solutions which, for the reasons described previously, can to a large extent be regarded and treated in a way similar to colloidal dispersions.

In the following, a brief overview of the determination of thermodynamic quantities from SAS experiments is given. If not stated otherwise, the information provided here is based on Ref. 37.
In complex fluids such as colloidal dispersions, a quantity of particular thermodynamic interest is the **pair correlation function** $g_N(\vec{r_1}, \vec{r_2})$ which describes the density profile of particles in the NVT ensemble:

$$g_N(\vec{r_1}, \vec{r_2}) := \frac{\rho_N^{(2)}(\vec{r_1}, \vec{r_2})}{\rho_N^{(1)}(\vec{r_1})\rho_N^{(1)}(\vec{r_2})} \tag{4.1}$$

If the system is homogeneous, $\rho_N^{(1)} = \rho = N/V$ is the particle number density and in isotropic systems, $\rho_N^{(2)}(\vec{r_1}, \vec{r_2}) = \rho_N^{(2)}(\vec{r_1} - \vec{r_2})$, the distribution function for $n = 2$ particles, is a function of the vector distance $r_{12} = r_1 - r_2$ between particles 1 and

2. For $r_{12} \to \infty$, $g_N(r_1, r_2) \to 1$. For isotropic and homogeneous systems, $\rho_N^{(1)}$ and g_N depend solely on $r = |r_{12}| = |\vec{r_1} - \vec{r_2}|$. Thus,

$$g_N(r) = \frac{N(N-1)}{\rho^2} \int d\vec{r_3} \cdots d\vec{r_N} P_N(r^N) \tag{4.2}$$

where $\vec{r_i}$ are position vectors of particles $1, \cdots, N$. The term $P_N(r^N)$ is equal to

$$P_N(r^N) = \frac{e^{-\beta U(r^N)}}{Z_N(V,T)} \tag{4.3}$$

with

$$Z_N(V,T) = \int d\vec{r_1} \cdots d\vec{r_N} e^{-\beta U(\vec{r}^N)} = \int d\vec{r^N} e^{-\beta U(\vec{r^N})}. \tag{4.4}$$

Thus, $P_N(r^N)$ describes the probability of finding the system in a certain arrangement of particle positions. $Z_N(V,T)$, the configurational integral, represents the probability density of finding all N particles of the system in question at positions $r_1, \cdots, r_N$.

By definition, $\lim_{N,V\to\infty} g_N(r) =: g(r)$. $g(r)$ is linked to the potential of mean force (PMF) $w(r_{ij})$ of the system under investigation as

$$g(r) =: e^{-\beta w(r)} \Leftrightarrow -k_B T \ \ln \ g(r_{ij}) = w(r_{ij}) \tag{4.5}$$

where r_{ij} is the distance between two particles. The PMF describes the force exerted on particle i if the position of particle j is fixed and the positions of all remaining $(N-2)$ particles are averaged. The PMF is linked to another crucial quantity describing the system in question — its potential energy $U(r^N)$ — *via*

$$-\nabla_i w(\vec{r_{ij}}) = \frac{\int d\vec{r_3} \cdots d\vec{r_N} (\frac{\partial U}{\partial \vec{r_1}})}{\int d\vec{r_3} \cdots d\vec{r_N} e^{-\beta U}} = \langle -\nabla_i U(\vec{r^N}) \rangle_{i,j} \tag{4.6}$$

The latter corresponds to the sum of interparticle pair interactions $\sum_{i<j}^{N} u(r_{ij})$ for all possible position vector configurations $\vec{r^N} = \{\vec{r_1}, \cdots, \vec{r_N}\}$. In the case of charge-stabilised colloidal particles, $u(r) = u_{el}(r) + u_{vdW}(r)$ is the total effective pair potential consisting of the electrostatic interaction u_{el} and the van der Waals attraction. In the dilute limit $\rho \to 0$, $w(r) \to u(r) \Leftrightarrow g(r) \to e^{-\beta u(r)}$.
Knowledge of $g(r)$ thus allows for a deduction of the effective interparticle interaction potential of the system under investigation. The experimental challenge is therefore to obtain $g(r)$ from a system with a given interaction potential. In the case of the protein-salt systems investigated in this thesis, these potentials are typically assumed to be screened Coulomb (SC) or sticky hard sphere (SHS) potentials. Before elaborating on details how $g(r)$ is obtained from scattering experiments, a brief overview on the setup of the latter will be given in the following.

4.1.2 Setup of small-angle scattering experiments

A schematic of a typical SAS experimental setup is shown in Fig. 4.1. In this simple description, we assume (a) that the interaction between the X-ray beam and the sample is weak, which means that only a small fraction of the incoming X-ray photons is scattered whereas the majority of them is transmitted, (b) that the scattering is predominantly elastic, i.e. only negligible energy exchange takes place between the sample and the X-ray photons, (c) that multiple scattering effects are negligible and (d) that the (colloidal or protein) particles are monodisperse and uniformly distributed throughout the sample [125, 126].

An X-ray wave with a wavelength λ, an initial wavevector $\vec{k_i}$ ($|\vec{k_i}| = 2\pi/\lambda$) and

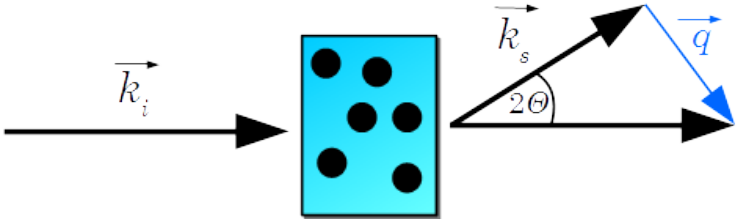

Figure 4.1: *Setup of a typical SAS experiment. Here, $\vec{k_i}$ and $\vec{k_s}$ are the wavevectors of the incoming and the scattered X-ray waves, $\vec{q}$ is the momentum transfer between them and 2θ is the scattering angle. The box represents a colloidal sample consisting of solvent (blue background) and particles dissolved therein. See text for details. Image reproduced in adapted form from Refs. 125 and 127.*

an initial frequency ω_i impinges onto a sample and is scattered at a certain angle 2θ. The scattered wave is described by a wavevector $\vec{k_s}$ and a frequency ω_f. The momentum transfer Δp between the X-ray wave and the particle of the scattering process is

$$\Delta p = \hbar\vec{k_i} - \hbar\vec{k_s} = \hbar\vec{q} \tag{4.7}$$

with $\vec{q} = \vec{k_i} - \vec{k_s}$. The relation between $q = \vec{q}$ and the scattering angle 2θ will be explained shortly. Similarly to the momentum transfer Δp, the energy transfer ΔE between the X-ray wave and the particle can be written as

$$\Delta E = \hbar\omega_i - \hbar\omega_s = \hbar\omega, \tag{4.8}$$

where $\omega = 2\pi\nu$ is the angular frequency of the radiation. The assumption that all scattering considered is elastic implies that the moduli of initial and scattered waves are equal [125]:

$$|\vec{k_i}| = |\vec{k_s}| = \frac{2\pi}{\lambda} \tag{4.9}$$

Using trigonometric considerations [125], the momentum transfer q can be shown to be related to the scattering angle by

$$q = \frac{4\pi}{\lambda} \sin\theta \tag{4.10}$$

The ratio of the incoming intensity I_i (flux, photons per unit time and area) and the final intensity I_f of a beam scattered by the sample at an angle 2θ and detected at a sample-detector distance L on a detector area $A_{det} = \Delta\Omega L^2$ is known as the differential scattering cross-section per unit solid angle of the sample investigated [126]:

$$\frac{I_f \cdot L^2}{I_i} = \frac{d\sigma}{d\Omega}(q) \tag{4.11}$$

The differential scattering cross-section can also be expressed as [126, 128]

$$\frac{d\sigma}{d\Omega}(q) = n(\Delta\rho)^2 V_{part}^2 P(q) S(q) \tag{4.12}$$

where n is the particle number density, $\Delta\rho$ is the electron density difference between the solvent and the particles and V_{part} is the volume of a single particle [126, 128]. The term $P(q)$ is referred to as the particle form factor and corresponds to the Fourier transform of the electron density of the particles studied [126, 129].

Detailed derivations of the form factor, *inter alia* for different molecular shapes can, e.g., be found in Refs. 125, 126 and 130. This aspect is not further discussed here. In the SAXS data analysis performed in the scope of the present thesis, the main focus was on the term $S(q)$ from Eqn. 4.12 which is referred to as the structure factor. In the next section, the route towards obtaining $g(r)$ and the determination of the effective interactions of the system in question from its $S(q)$ is explained.

4.1.3 Obtaining the interparticle potential $u(r)$ from $S(q)$

Importantly, the structure factor $S(q)$ obtained from a scattering experiment is the Fourier transform of the pair correlation function (introduced in Section 4.1.1) of the system in question:

$$S(q) = 1 + \frac{N-1}{V} \int_V (g(r) - 1) e^{-iqr} dr \tag{4.13}$$

The term $g(r) - 1$ is known as the so-called **total correlation function** $h(r)$ [126]. The Ornstein-Zernike (OZ) equation

$$h(r_{12}) = c(r_{12}) + \rho \int dr_3 c(r_{13}) h(r_{23}) \tag{4.14}$$

defines the **direct correlation function** $c(r)$. Eqn. 4.14 is known as the Ornstein-Zernike (OZ) equation. To clarify its physical meaning, $h(r)$ and $c(r)$ are often used with indices 1, 2 and 3 as seen in Eqn. 4.14 [126], referring to separate particles the interaction between which is considered. Thus, the total correlation between particles 1 and 2 includes their direct correlation as well as their respective correlation with an intermediate particle 3. This interpretation is based on the expression of Eqn. 4.14 as an infinite geometric series [126]. It is important to note that $c(r)$ is not known in the course of an experiment and that the OZ equation does not itself yield $u(r)$, the interaction potential of the system investigated. Another equation connecting $h(r)$ and $c(r)$ with $u(r)$ — a so-called closure relation — is thus needed [126].

Several closure relations are known such as the Percus-Yevick (PY), hypernetted chain (HNC), Rogers-Young (RY) or mean spherical approximation (MSA). As an example, the calculation of $S(q)$ using the mean spherical approximation (MSA) closure is given here. The MSA relation is obtained in the dilute limit ($\rho \to 0$) of Eqn. 4.14 [126], in which case, as discussed above, $g(r) = e^{-\beta u(r)}$. Therefore

$$c(r) = e^{-\beta u(r)} - 1 \tag{4.15}$$

and for $\beta u(r) \ll 1$

$$c(r) = -\beta u(r) - 1 \tag{4.16}$$

A final crucial relation discussed here is that of $S(q)$ to the isothermal compressibility χ_T which can be expressed as [36, 126, 131–134]

$$\chi_T = \rho^{-1}\Big(\frac{\partial \rho}{\partial p}\Big)_T = \Big(\frac{\partial \Pi}{\partial c}\Big)_T^{-1} = -\frac{1}{V}\Big(\frac{\partial V}{\partial P}\Big)_T \tag{4.17}$$

According to considerations based on the grand canonical ensemble, χ_T can be written as [36, 126, 131, 133, 134]

$$(\rho k_B T \chi_T)^{-1} = 1 - \rho\tilde{c}(0) = 1 - 4\pi\rho \int_0^\infty dr\ r^2 c(r) \tag{4.18}$$

$$\Leftrightarrow \rho k_B T \chi_T = 1 + \rho \int dr(g(r) - 1) = S(q \to 0)$$

Importantly, $S(q \to 0)$ and therefore also χ_T can be expanded into a series of virial coefficients A_n [132, 133, 135]:

$$S(q \to 0) = \frac{RT}{M_W}\Big(\frac{\partial \Pi}{\partial c}\Big)^{-1} = \frac{1}{1 + 2M_W A_2 c + ...} \tag{4.19}$$

where M_W (g/mol) is the molecular weight of the particles investigated.

The second virial coefficient B_2 [52]

$$B_2 = 2\pi \int_0^\infty dr\ r^2[1 - e^{\frac{-u(r)}{k_B T}}] \tag{4.20}$$

is related to A_2 *via* [136]

$$B_2 = A_2 \cdot \frac{M_W^2}{N_A} \tag{4.21}$$

The SAXS data obtained on the protein-cation experimental systems studied in this thesis were analysed using the software Igor Pro [137]. An ellipsoidal form factor with varying axis lengths, the volume fraction and the scattering length density of BSA were used as input parameters. At low salt concentrations, a screened Coulomb (SC) potential was used for data fitting. Above a certain threshold salt concentration, a sticky hard sphere (SHS) potential was assumed and the corresponding structure factor was calculated based on the above equations. The reduced second virial coefficient values, B_2/B_2^{HS}, were extracted *via* the stickiness parameter τ [52] obtained from the data fits. The B_2/B_2^{HS} values are used as a measure of the type of overall interactions in the samples investigated [52, 84, 89, 138]. Details of the data analysis routine followed in this thesis are given in Chapter 6.

The SAXS data presented in this thesis were obtained at beamline ID02 at the European Synchrotron Radiation Facility (ESRF) in Grenoble, France. Further details on the experimental setup are given in Chapter 6. Details about the beamline are found in Section 4.4.

4.2 Ultra-small angle scattering

4.2.1 Ultra-small angle x-ray scattering (USAXS)

In this thesis, USAXS was used to follow the kinetics of LLPS in BSA-multivalent salt systems in real time. Here, the objects measured using this technique are domains of the dense and dilute liquid phases obtained by heating samples showing LCST-LLPS behaviour. The parameter ultimately obtained from the USAXS experiments is the characteristic length scale of the system $\xi(t, T)$ which is calculated from the intensity value at q_{max}.

The USAXS experiments were performed at beamline ID02 at the ESRF. The minimum q values accessible were around 10^{-3} nm^{-1}, which corresponds to a sample-detector distance of 30.7 m. Further details of these experiments and the experimental setup are given in Chapter 7; details about the beamline are given in Section 4.4. The most important aspect of the USAXS technique used for the systems investigated here is the fact that it allows to monitor kinetic processes with a time resolution down to fractions of seconds, thus allowing to capture the initial state of phase separation.

4.2.2 Very small angle neutron scattering (VSANS)

A part of the kinetic measurements preformed in the scope of this thesis was performed using neutron scattering. Although the information obtained by X-ray and neutron small-angle scattering is rather similar in the experiments performed here, some general differences between these two techniques are inherent to the different physical properties of the two types of probe particles used. These will be briefly outlined in the following.

X-ray radiation consists of massless photons with a spin of 1 which mainly interact with electrons of the particles in question *via* long-range electromagnetic interactions [125]. According to wave-particle duality and Planck's quantum mechanical considerations, the energy E of X-ray radiation is equal to

$$E = h\nu = hc/\lambda \tag{4.22}$$

where h is Planck's constant, ν is the frequency and λ is the wavelength of the X-ray radiation and c is the speed of light [125]. E can also be expressed *via* the kinetic energy gained by an electron which is accelerated through a potential difference of V volts (i.e., 1 eV = 1.6 $\cdot 10^{-19}$ J). Thus, X-ray radiation can be classified by its wavelength (e.g. $\lambda = 1$ Å), its frequency (e.g. $3 \cdot 10^6$ THz) and/or its energy (e.g. 12.4 keV) [125].

In contrast, neutrons interact with atomic nuclei via the short-ranged strong nuclear force [125, 139]. Having a finite mass of $m_n = 1.66 \cdot 10^{-24}$ g, the particle-like properties of neutrons cannot be neglected. Therefore, the wavelength of neutron radiation is related to their finite particle mass *via* De Broglie's equation, $\lambda = h/p = h/(m_n v)$. Their energy is then expressed the classical way as $E = mv^2/2 = h^2/(2m_n\lambda^2)$. Neutron radiation with a wavelength of 1 Å therefore has an energy of 81.8 meV and, an aspect particularly important for experiments depending on energy selection, a velocity of 3.96 km s^{-1}. Additionally, the energy of neutrons is often expressed in units of thermal energy, $k_B T$.

Since neutrons have a magnetic moment $\mu = -1.913$ nuclear magnetons [139], they also interact with the orbital electron which gives rise to a magnetic form factor [125]. This phenomenon is not further considered here. However, another property of neutrons distinguishing them from photons leads to an aspect important to consider in experiments — their half-integer spin $S = 1/2$.

In the case of neutron scattering, the atomic form factor $f_0(\lambda, \theta)$ is equal to $-b$, the so-called scattering length [125]. b differs from element to element and from isotope to isotope. $\langle b_i \rangle$, the average b_i over all isotopes in a given sample is referred to as the coherent scattering length

$$b_i^{coh} = \langle b_i \rangle \tag{4.23}$$

The root mean square deviation (rms) of b_i from $\langle b_i \rangle$

$$[\langle b_i^2 \rangle - \langle b_i \rangle^2]^{1/2} \tag{4.24}$$

is known as the incoherent scattering length b_i^{inc}. The corresponding coherent and incoherent scattering cross-sections σ_{coh} and σ_{inc} are equal to $4\pi\langle b \rangle^2$ and $4\pi\langle (b - \langle b \rangle)^2 \rangle$, respectively.

Upon interaction of a hydrogen nucleus — which also has a spin of 1/2 — with a neutron, their spins can be combined into a triplet (S^+) in 3 possible ways or a singlet (S^-) in 1 possible way

$$\langle b \rangle = \frac{1}{4}[3b^+ + b^-] \tag{4.25}$$

and

$$\langle b^2 \rangle = \frac{1}{4}[3(b^+)^2 + (b^-)^2]. \tag{4.26}$$

The corresponding scattering cross sections σ_{coh} are 1.8 barns and $\sigma_{inc} = 80.3$ barns (1 barn = 10^{-24} cm^2) [125]. σ_{coh} and σ_{inc} of the heavy hydrogen isotope, deuterium (D) with a spin of 1, however, are equal to 5.6 barns and 2.0 barns, respectively. This implies that, when using neutrons as a scattering probe, the amount of hydrogen and deuterium will have a strong influence on the overall signal. The advantage is that selective deuteration of the sample in question can be used in order to investigate different parts of it. Importantly, since the incoherent scattering function is the Fourier transform of the self-correlation function [126], the incoherent scattering cross section can be used for investigations of dynamic processes inside the sample. This has been successfully applied to study e.g. protein diffusion [101, 140–144] or their internal dynamics [145–148] as well as the dynamics of water [149, 150] or polymer blends [151].

An advantage of neutron scattering techniques is that the absorption edges for neutrons are typically outside of the neutron wavelengths used in experiments. In addition, no ionisation takes place. These two aspects strongly decrease radiation damage.

The VSANS experiments described here were performed at beamline KWS-3 (FRM-II, Garching, Germany) at a sample-detector distance of 9.5 m. A more detailed description of the beamline is given in Section 4.5.

4.3 Extended x-ray absorption fine structure analysis (EXAFS)

In typical small-angle scattering experiments, the energy of the X-rays used is typically chosen so as to prevent X-ray absorption by the sample. However, designated spectroscopy experiments rely on X-ray absorption in order to deduce information about chemical properties of the sample in question. In the present

thesis, extended X-ray absorption fine structure analysis (EXAFS) was used to investigate the change in the coordination number (CN) of Y^{3+} cations (in this case, the CN corresponds to the number of oxygen atoms of either water molecules or BSA carboxyl groups) in the presence of BSA as a function of temperature and salt concentration. The method will be briefly described in the following.

For radiation frequencies ω far away from absorption edges, scattering is purely elastic, does not depend on the frequency of the incoming radiation and the atomic form factor $f_0(q)$, that is, the Fourier transform of the electron density of an isolated atom, is real-valued [125, 152]. However, certain X-ray frequencies correspond e.g. to the binding energies of core-level electrons [152, 153]. In this case, the scattering process is inelastic and absorption occurs. In literature, this phenomenon is often referred to as anomalous scattering [152]. $f_0(q)$ then features a pronounced dependence on ω and needs to be supplemented by a complex term consisting of a real part $f'(q,\omega)$ and an imaginary part $f''(q,\omega)$ [152] (known as the anomalous components [152] or dispersion coefficients [154]):

$$f(q,\omega) = f_0(q) + f'(q,\omega) + if''(q,\omega) \tag{4.27}$$

Note that the dependence on q is typically neglected when rationalising anomalous scattering [152] since the radius of the orbital hosting the electrons responsible for the anomalous signal is much smaller than the wavelength of the radiation used [154]. The complex term constituents can therefore be simply referred to as f' and f''. Overall, the complex term thus confers the behaviour of a damped harmonic oscillator close to a resonance edge to the atomic form factor.

It can be shown [152] that the sum of $f_0(q)$ and the real part f' is given by

$$f_0(q) + f' = \sum_{1}^{n(e)} g(s) \frac{\omega^2(\omega^2 - \omega_s^2)}{(\omega^2 - \omega_s^2)^2 + \alpha^2\omega^2} \tag{4.28}$$

and that the imaginary part $f''(q,\omega)$ corresponds to

$$f'' = \sum_{1}^{n(e)} g(s) \frac{\alpha\omega^3}{(\omega^2 - \omega_s^2)^2 + \alpha^2\omega^2}. \tag{4.29}$$

where the sum is calculated over the total number of electrons $n(e)$ in the atom considered, $g(s)$ is the oscillator strength for radiation with a frequency ω_s and α is a force constant. The real and imaginary terms are connected *via* the Kramers-Kronig transform [152]:

$$f'(\omega_0) = \frac{2}{\pi} \int_0^\infty \frac{\omega}{\omega^2 - \omega_0^2} f''(\omega) d\omega \tag{4.30}$$

From an experimental point of view, it is important that the distinct properties and states of the atom investigated influence the probability of an X-ray absorption process. This phenomenon gives rise to structures known as X-ray absorption fine

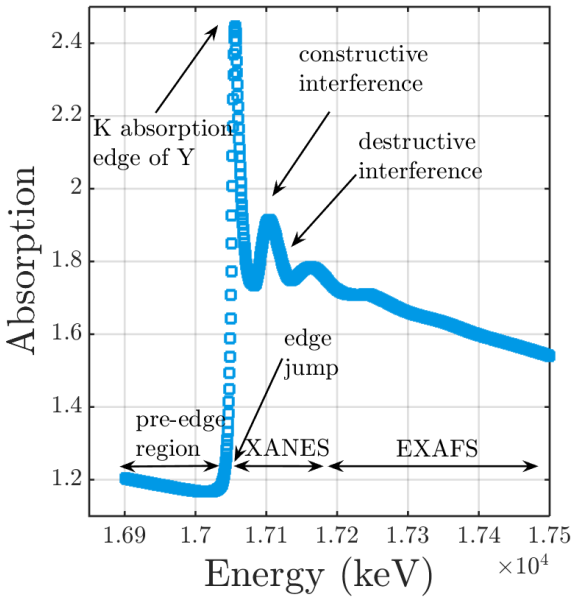

Figure 4.2: *An X-ray absorption spectrum. The Y K-edge data shown here were collected on a dense phase obtained after LLPS of a sample containing initial concentrations of 175 mg/ml BSA and 40 mM YCl_3 during beamtime SP14011 (beamline B18, Diamond Light Source, UK). The labelling is according to Ref. 153. See text for details.*

structure (XAFS).

An X-ray absorption spectrum is commonly divided into two regions (see Fig. 4.2). The first one is the X-ray absorption near-edge spectroscopy (XANES) region within 50 eV of the edge jump. XANES can be used to detect the coordination geometry and the oxidation state of the absorber. The second region is referred to as the extended X-ray absorption fine structure analysis (EXAFS) and is located at 50-1000 eV above the edge jump [155]. Note that the distinction between the EXAFS and XANES regions is somehow arbitrary due to the fact both regions rely on the same physical phenomena [155].

In the process of absorption of X-rays with an energy higher than the binding energy of a core-level electron of the absorbing atom, photoelectrons are emitted. Their wavenumber k is expressed as a function of E_0, the absorption edge energy and E, the transmitted X-ray energy and the electron mass m_e as

$$k = \sqrt{\frac{2m_e(E - E_0)}{\hbar^2}} \tag{4.31}$$

When analysing X-ray absorption spectroscopy data, EXAFS ($X(k)$) is commonly

defined as the modulation of the X-ray absorption coefficient [155]

$$X(k) = \frac{\mu_{abs} - \mu_{abs,0}}{\mu_{abs,0}} \tag{4.32}$$

where μ_{abs} is the absorption coefficient observed in the experiment and $\mu_{abs,0}$ is the theoretical absorption without EXAFS effects [155]. The characteristic oscillations of an EXAFS spectrum are due to backscattering of the photoelectron ejected from the absorber by neighbouring atoms. Constructive and destructive interference between the initial wavefunction of the photoelectron emitted lead to minima and maxima in the EXAFS spectrum [40, 152, 153], thus providing information on the type of and distance to the neighbouring atoms as well as the CN of the absorber [40, 153]. These aspects are summarised in the EXAFS equation [153]:

$$X(k) = \sum_j \frac{N_j f_j(k) e^{-2k^2 - \sigma_j^2}}{kR_j^2} sin[2kR_j + \delta_j(k)]. \tag{4.33}$$

Here, $\delta(k)$ and $f(k)$ are the phase shift and scattering amplitude of the atoms neighbouring the absorber. N is their number, R their respective distance to the absorber and σ^2 the mean square deviation of this distance [153] due to thermal and static disorder of the sample.

The EXAFS experiments described in this thesis were performed in transmission mode at beamline B18 (Diamond Light Source, UK). Data analysis using the Demeter software package [156] was performed by Sin-Yuen Chang and Sven L. M. Schroeder. Further experimental details and results are presented in Chapter 8.

4.4 Working principle of a synchrotron

The scattering experiments presented in the scope of this thesis were performed at large-scale facilities designated for applied research exploiting various X-ray and neutron radiation techniques. Details can, e.g., be found in Refs. 125, 152, 154, 157 and 139; here, only a brief summary of the principles of such facilities will be provided.

Synchrotron radiation was first observed as a side reaction at particle accelerators designed for high energy physics research in the late 1940s [125]. Once its full potential for research was realised, synchrotron radiation went on to become a most valuable research tool particularly for soft matter science. The information given here refers to the ESRF.

The principle of synchrotron radiation relies on the fact that a charge emits radiation when its speed or its direction of motion are changed [125]. In the case of a synchtrotron, electrons moving at relativistic speeds are used. Indeed, the extremely high intensity of synchrotron radiation as compared to, e.g., vacuum tubes, is traced back to a phenomenon referred to as relativistic beaming (see Refs. [125], [158] and [159] for details). The phenomenon of relativistic beaming

describes the fact that the radiation pattern of a particle moving along a curved trajectory with a velocity approaching c resembles a narrow cone tangential to the particle orbit and along the forward direction of the particle [125, 158]. The vertical half-opening angle ψ_{cone} of this cone is expressed as [159]

$$\psi_{cone} \approx m_e c^2 / E \tag{4.34}$$

For a storage ring energy in the order of 1 GeV, ψ_{cone} is therefore $\approx 0.029\,^{\circ}$. Relativistic beaming thus implies an extremely high degree of collimation of synchrotron radiation as well as outstandingly high fluxes on small areas [159].

In synchrotrons, the electrons are emitted by an electron gun at the beginning of the linear accelerator (linac). They are subsequently accelerated to 200 MeV and enter the so-called booster synchrotron. Here, the electrons are accelerated to 6 GeV and passed on to the storage ring with an ultra-high vacuum of 10^{-9} mbar [157]. The storage ring is divided into straight and curved sections [125]. In the former, a strong deviation of the electron beam from its path is prevented by focusing magnets. Additionally, so-called radio frequency (RF) cavities emit electromagnetic pulses to keep the electrons from losing too much energy due to radiation dissipation [125]. In the curved sections, bending magnets are the spots at which X-ray radiation is produced [125, 157].

In 3^{rd} generation synchrotrons [125], wigglers and undulators [125, 154, 157] (also known as insertion devices) are used additionally in the straight sections. Both devices consist of multipole magnets [159], thus applying an alternating magnetic field to the electron beam and allowing for the emission of synchrotron radiation at each magnet section [159]. The radiation resulting from the electron beam passing a wiggler is the incoherent sum of the radiation produced at each pole [159]. This implies that the intensity of the total synchrotron radiation emanating from a wiggler is N times more intense than that emitted at a bending magnet with N being the number of the wiggler poles [159]. In the case of an undulator, the amplitudes of the radiation produced at each pole are summed up coherently. Therefore, the intensity of synchrotron radiation emitted by an undulator is even more intense than that produced at a wiggler [159].

Generally, synchrotron radiation covers an energy range from high-energy X-rays to microwave radiation [157]. Once emitted by the insertion devices, it is then directed to designated beamlines at which experiments using the respective types of radiation are carried out [157].

The SAXS experiments described in this thesis were performed at beamline ID02 at the ESRF [160]. During the ESRF Phase I upgrade program (2009-2015), the q range of the beamline was extended to allow for time-resolved ultra-small angle scattering (TR-USAXS) measurements [161]. When combining (U)SAXS and WAXS (wide angle-X-ray scattering) setups, the upgraded instrument now covers a $q = \frac{4\pi}{\lambda}\sin(\frac{\theta}{2})$ range from 10^{-3} to 50 nm^{-1} [160]. The synchrotron radiation beam emanating from two undulators passes a Si(111) monochromator cooled by liquid N_2, after which it is focussed *via* a double (toroidal and fine

planar) mirror setup in the horizontal plane. This setup allows for high-flux measurements. To ensure high resolution, the beam is further collimated by slit collimation using pseudo channel-cut crystals [161, 162]. The detector tube (internal pressure = $5 \cdot 10^{-3}$ mbar) has a length of 34 m and hosts three detectors designated for (U)SAXS, high-resolution USAXS and standard SAXS [161]. The sample-to-detector distance (SD) for (U)SAXS measurements can be adjusted from 0.8 to 30.4 m *via* a rail wagon setup (Ref. 161 and refs. therein). The energy range of ID02 is 8-20 keV [160].

4.5 Working principle of neutron facilities

Neutron scattering experiments are performed at neutron reactors or spallation sources. At neutron reactors (here, the FRM-II reactor in Garching, Germany, at which the VSANS experiments described in this thesis were performed is taken as an example), a continuous production of free neutrons is ensured by fission of a fuel element made of uranium enriched with its radioactive isotope ^{235}U. Fission of the elements is induced by the absorption of a neutron from the fission reaction itself or from cosmic rays. A chain reaction ensues, creating fast neutrons. The fuel element is located in a moderator tank (which itself is inside the reactor pool) filled with heavy water (D_2O). The latter acts as a neutron moderator, thus ensuring production of the slow neutrons needed to sustain the fission reaction and for the experiments performed eventually [125, 139]. When in thermal equilibrium with the moderator, the neutrons will have a speed distribution according to Maxwell [40, 139]. The number of neutrons per unit area per second with a velocity distribution between v and Δv (flux $\Phi(v)$) is expressed *via* [139]

$$\Phi(v) = \Phi \frac{1}{2} \left(\frac{m_n}{k_B T} \right)^2 v^3 \; e^{\left(-\frac{1}{2} \frac{m_n v^2}{k_B T} \right)} \tag{4.35}$$

Given a moderator temperature of 300 K, the most probable neutron wavelength corresponds to 1.54 Å (thermal neutrons). This wavelength is ideal for the investigation of characteristic lengths (e.g. interatom distances) of liquid and solid samples [125, 139].

An alternative to neutron reactors are spallation sources. Here, protons are accelerated by an adjacent synchrotron in a pulsed manner and guided towards a target made from, e.g. Wo or Hg [139]. Elementary particles including neutrons and protons are generated during the proton-target collision referred to as spallation [125]. Just like in the reactor, the resulting neutrons are moderated to suit the experimental requirements [139]. Once free neutrons have been generated by either of the two methods (fission or spallation), they reach the experimentall hall *via* neutron guides. The latter can, e.g., be glass tubes with an internal 1000 Å cover of Ni, leading to total neutron reflection with a minimal loss of intensity [139].

The VSANS experiments described in this thesis were performed at beamline KWS-3 [163, 164] at the neutron reactor FRM-II in Garching (Germany). The

setup and experimental procedure of KWS-3 is as follows. Neutrons enter the instrument *via* the neutron guide and undergo velocity selection *via* a Mg-Li selector (wavelength divergence $\Delta\lambda/\lambda = 0.2$). A double focussing neutron mirror setup (2 mirrors coated with an 80 nm layer of ^{65}Cu [164]) with a horizontal reflection plane ensures a good resolution at low q (down to 1 $\cdot 10^{-4}$ Å^{-1}). This toroidal mirror setup, initially developed for x-ray telescopes [165] has the advantage of a strongly improved image due to the correction of gravity effects [166–168]. The detector is a 2D glass scintillator [164].

4.6 Ultraviolet-visible (UV-Vis) spectroscopy

In the experiments performed for this thesis, the absorption of ultraviolet (UV) light by aromatic amino acid residues at $\lambda = 280$ nm [1] was used to estimate the protein concentration of stock solutions and samples. The principles behind UV-Vis spectroscopy are described in the following.

In a UV-Vis spectroscopy experiment, UV-Vis radiation with an intensity I_0 is attenuated by a sample at a given wavelength λ. Having passed the sample, the intensity is equal to I with $I < I_0$. The change in intensity (dI) after passing through a sample layer of thickness dl with a sample concentration $[c]$ and a proportionality coefficient a can be expressed *via* [40]:

$$dI = -a[c]Idl \Leftrightarrow \frac{dI}{I} = -a[c]dl \tag{4.36}$$

The decrease in intensity upon passing a sample of total thickness l is then obtained as

$$\int_{I_0}^{I} \frac{dI}{I} = -a \int_0^l [c]dl. \tag{4.37}$$

$[c]$ is assumed to be constant throughout the sample so that the final integral is equal to

$$\ln\frac{I}{I_0} = -a[c]l. \tag{4.38}$$

$\ln(\frac{I}{I_0})$ can be converted into its decadic form $\log(\frac{I}{I_0})$ by multiplying the former expression by $\ln(10)$. The argument of the logarithm, $\frac{I}{I_0}$, is known as the transmission T of the sample:

$$T = \frac{I}{I_0} \tag{4.39}$$

and

$$\log(1/T) = A \tag{4.40}$$

defines the absorbance A of the sample. Replacing a by $\epsilon \cdot \ln 10$ and cancelling out ln 10 on both sides of the equation, Eqn. 4.38 can then be rewritten as

$$A = \epsilon[c]l \tag{4.41}$$

which corresponds to the commonly known, linearised form of the Beer-Lambert law [40]. Here, ϵ is the so-called extinction coefficient in units of volume/(mol · length). Eqn. 4.41 is used to determine protein concentrations c by monitoring the absorbance at $\lambda = 280$ nm. It is important to keep in mind that with increasing concentrations, deviations from the Beer-Lambert law can occur [169].

All UV measurements were performed in quartz cuvettes (Hellma, Müllheim, Germany) with path lenghts of 1 cm using a Cary 50 UV-Vis spectrometer (Varian Inc., now Agilent Technologies, California, USA). Every concentration was determined in triplicate. The background correction was performed by subtracting a water signal from the respective measurements.

In addition to concentration determinations, temperature-dependent absorbance measurements were performed to determine the transition temperatures of samples consisting of BSA and lanthanide mixtures. The experimental procedure is described in more detail in Chapter 6.

4.7 Zeta potential

The adsorption of multivalent cations to BSA changes the surface charge of the protein and is the driving force behind the cation-induced phase behaviour of BSA-cation complexes. To quantify this phenomenon, zeta (ζ) potential measurements were performed. The theoretical rationalisation of this phenomenon (if not stated otherwise, this information is based on Ref. 41) as well as the experimental technique will be briefly described in the following. Detailed descriptions of electrokinetic phenomena can be found in Refs. 170, 171 and 172. The model used for interpretation of the zeta potential data measured in the course of this thesis (cf. Chaps. 5 and 6) had been developed previously by Roosen-Runge *et al.* [83].

To describe the interaction between a charged surface and counterions adsorbing to it, Helmholtz developed a model of a rigid counterion layer attached to the surface in question. This model treats the surface and the counterion layer as a parallel plate capacitor with a capacitance C:

$$C = \frac{Q}{U} = \frac{\epsilon_0 \epsilon_r A}{d} \tag{4.42}$$

where Q and U are charge and voltage, ϵ_0 is the dielectric constant of the vacuum, ϵ_r the dielectric constant of the medium into which both the surface and the counterions are immersed, A is the area of the plates considered and d is the centre-to-centre distance between the charged surface and the counterion layer. The potential difference $\Delta\psi$ between the surface and the counterions is then given

by

$$\Delta\psi = \frac{d \cdot Q}{\epsilon_0 \epsilon_r A}. \tag{4.43}$$

In the case of the parallel plate capacitor approach, the potential difference between the surface and the counterion layer is linearly proportional to the distance between them.

The Helmholtz theory disregards thermal motion of the counterions, assuming an unrealistic rigidity of the counterion layer. This drawback is addressed in the Gouy-Chapman model which pictures the counterion layer as diffuse, but has the shortcoming of assuming that the charges in question are point-like. Rigid and diffuse models are combined in the Stern model (Fig. 4.3), resulting in a more comprehensive and realistic description of the interactions between charged surfaces and counterions.

In the Stern model, the potential between the charged surface and the first rigid counterion layer decreases linearly until the outer Helmholtz layer begins at a distance d_H. After this layer, the diffuse double layer begins and the potential decays exponentially. The thickness of the diffuse double-layer, β, is derived from electrophoretic theory and can be calculated *via* $1/\beta = \left(\frac{2N_A e^2 I}{\epsilon_0 \epsilon_r k_B T}\right)^{1/2}$ where e is the elementary charge, N_A is Avogadro's constant and I is the ionic strength. The extension of the diffuse double layer beyond into the bulk solution for length scales beyond β is denoted by x in Fig. 4.3). The potential decay along this extension is referred to as the ζ potential.

In order to investigate the potential decay as a function of the distance from the outer Helmholtz layer, the length scale $\zeta = x - d_H$ is introduced. Thus, the decay of the potential along the diffuse double layer — which begins at the outer Helmholtz layer — is referred to as the ζ potential. The relation between ζ, ψ and the spatial charge density ρ_s is given by the Poisson equation

$$\nabla^2\psi(\zeta) = \frac{d^2\psi}{d\zeta^2} = -\frac{\rho_s(\zeta)}{\epsilon_r \epsilon_0} = \left(\frac{1}{\beta}\right)^2 (\psi(\zeta) - \psi_A) \tag{4.44}$$

Importantly, Eqn. 4.44 accounts for the fact that ψ approaches a finite value ψ_A for $\zeta \to \infty$.

All ζ potential measurements presented in this thesis were performed by probing the electrophoretic mobility of BSA in the presence of different concentrations of multivalent cations *via* laser Doppler electrophoresis. To this end, an electric field is applied to the sample in question and the electrophoretic mobility μ_e [170]

$$\mu_e = \frac{2\epsilon_r \zeta f(\kappa a)}{3\eta} \tag{4.45}$$

(with ζ being the zeta potential, $f(\kappa a)$ the Henry function where κ is the Debye screening length, a is the particle diameter and η is the viscosity of the solution)

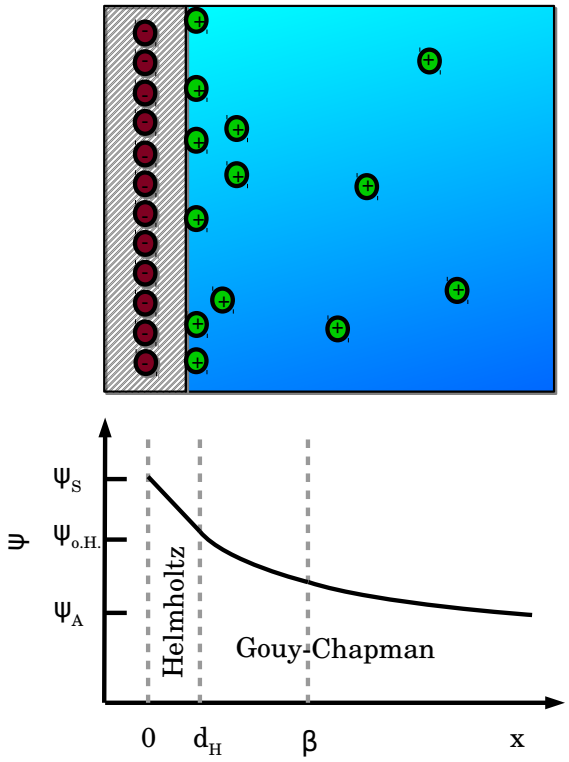

Figure 4.3: *Stern model combining the rigid (Helmholtz) and diffuse (Gouy-Chapman) double layer models. The grey shaded area represents a surface immersed into bulk liquid (blue continuum). The red circles on the shaded area represent negatively charged particles, the green circles illustrate positively charged ones. The potential ψ decays linearly between the surface (ψ_S) and the outer Helmholtz layer ($\psi_{o.H.}$ at a distance d_H). At d_H, the diffuse double-layer begins and ψ decays exponentially, asymptotically approaching a value ψ_A at long distances from the charged surface. The potential decay occuring along this extended protrusion of the diffuse double layer into the bulk is referred to as the ζ potential. Figure reproduced and adapted from Ref. 41.*

of the sample is measured by laser doppler. The Henry function can take values from 1.0 to 1.5 for κa values from low to infinity [170]. Depending on the mobility of the BSA-cation complexes in the sample, the scattering pattern (in this case, collected at an angle of 173 °) changes as known from dynamic light scattering experiments. This setup is referred to as non-invasive backscatter (NIBS) [173].

All zeta potential measurements were performed using a Nano Zetasizer (Malvern Instruments, Malvern, UK) at the Interfaculty Institute of Biochemistry (Tübingen). Experimental conditions are described in detail in Chapter 6. The ζ potential

values obtained from the measurements were subsequently converted to effective surface charges of the respective BSA-cation complexes (see Section 6.9).

4.8 Isothermal titration calorimetry

Isothermal titration calorimetry (ITC) is a technique commonly used to analyse the thermodynamic parameters of interactions between a ligand and a macromolecule. Typical areas of application can include protein-protein, protein-DNA or protein-ion interactions.

The setup consists of a reference cell and a sample cell surrounded by an adiabatic shielding and an injection syringe. The sample cell is filled with a solution containing the macromolecule in question (here: protein), while the reference cell contains the solvent in which the macromolecule is dissolved (here, water was used; for other experimental systems, buffer solutions may be preferred). During an ITC measurement, the syringe injects small volumes of ligand in user-defined time intervals into the sample cell. With each injection, the reaction between macromolecule and ligand absorbs heat (endothermic reaction, $\Delta H > 0$) [40] from or releases heat into (exothermic reaction, $\Delta H < 0$) [40] the sample cell. This heat q_i is proportional to the sample cell volume (V), the binding enthalpy of the reaction in question (ΔH) and the amount of ligand injected (ΔL_i) at every injection i [174],

$$q_i = V \cdot \Delta H \cdot \Delta L_i \tag{4.46}$$

A schematic of a typical isothermal calorimeter is shown in Fig. 4.4.

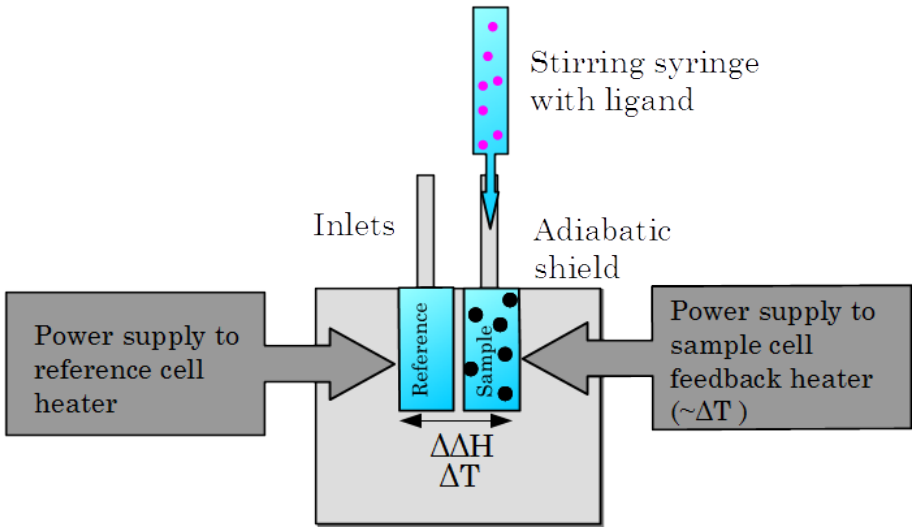

Figure 4.4: *Schematic setup of a typical ITC instrument. See text for details. Figure replotted and adapted from Ref. 175.*

For the experiments performed in this thesis, a so-called power compensation

calorimeter was used. The working principle is as follows. The entire setup is kept at a constant temperature which is achieved by a cooling circuit and simultaneous temperature control by a heater and a cooler. A temperature increase in the sample cell due to an exothermic macromolecule-ligand interaction reduces the power supply to the heater, ensuring that the overall temperature remains constant. Raw data are therefore obtained in units of µcal/s. The final result is given in cal/(mol of injectant) [175].
Importantly, the titration data obtained by titrating the ligand into the macromolecule need to be corrected for the heat of dilution of the ligand in the solvent. To this end, a "blank" titration of the ligand into the solvent is performed. These data are then subtracted from the ligand into macromolecule titration. An ITC measurement thus allows for direct determination of ΔH of the interaction between the macromolecule and ligand in question.
In the case of a simple system with only one ligand binding site, Eqn. 4.46 can also be written as [174]

$$q_i = v \cdot \Delta H \cdot [P] \cdot \left(\frac{K_a [L]_i}{1 + K_a [L]_i} - \frac{K_a [L]_{i-1}}{1 + K_a [L]_{i-1}} \right) \tag{4.47}$$

where $[P]$ represents the total macromolecule concentration and $[L]$ is the concentration of the free ligand at every injection i. For systems with more binding sites, the expression is expanded by additional terms. Thus, the association constant K_a between the ligand and the macromolecule can be determined. This, in turn, yields ΔG of the reaction *via* the Arrhenius equation [40]

$$K_a = A e^{\frac{-\Delta G}{RT}} \tag{4.48}$$

where A is an experimental constant (sometimes set to 1 in a biological context) and R is the ideal gas constant. Finally, the Gibbs-Helmholtz equation [40]

$$\Delta G = \Delta H - T \Delta S \tag{4.49}$$

allows to calculate the entropic term of the macromolecule-ligand interaction.

All ITC measurements were performed using a MicroCal iTC200 (Malvern Instruments, Malvern, UK; formerly GE Healthcare) located at the Max-Planck Institute for Developmental Biology in Tübingen (Chapter 5) or at the Centre for Plant Molecular Biology (*Zentrum für Molekularbiologie und Biochemie der Pflanzen*, ZMBP) (Chapter 6). Experimental details are given in Chapters 5 and 6.

Part III

Results

Chapter 5

Cation-induced hydration effects cause lower critical solution temperature behavior in protein solutions

5.1 Abstract

The phase behavior of protein solutions is important for numerous phenomena in biology and soft matter. We report a lower critical solution temperature (LCST) phase behavior of aqueous solutions of a globular protein induced by multivalent metal ions around physiological temperatures. The LCST behavior manifests itself via a liquid-liquid phase separation of the protein-salt solution upon heating. Isothermal titration calorimetry and zeta-potential measurements indicate that here cation-protein binding is an endothermic, entropy-driven process. We offer a mechanistic explanation of the LCST. First, cations bind to protein surface groups driven by entropy changes of hydration water. Second, the bound cations bridge to other protein molecules, inducing an entropy-driven attraction causing the LCST. Our findings have general implications for condensation, LCST, and hydration behavior of (bio)polymer solutions as well as the understanding of biological effects of (heavy) metal ions and their hydration.

5.2 Introduction

Understanding and tuning the phase behavior and phase transitions of proteins in solution is an important goal in many areas of protein science, such as protein condensation diseases or formulation of antibody-based drugs, and the search for tunable pathways to protein crystallization. In particular, liquid-liquid phase separation (LLPS), that is, the separation of protein solutions into a dilute and

dense phase, has attracted much attention due to its potential role in protein condensation diseases such as eye cataract and sickle cell anemia [17, 63, 133]. Moreover, a metastable LLPS can play an important role in the nucleation of protein crystals [133, 176, 177].

The generic control parameter of LLPS is temperature (T). Intuitively, one expects a mixed system at higher T due to the dominating entropic contributions, and phase separation at lower T. This so-called *upper critical solution temperature (UCST)* behavior occurs, for example, in aqueous solutions of several proteins such as crystallins [17], lysozyme [57, 178, 179] or β-lactoglobulin [82].

Interestingly, under certain conditions, systems feature a *lower critical solution temperature (LCST)*, that is, the mixed state of a system occurs at a *lower* temperature than the phase-separated state. It is important to note that, for a given system, UCST and LCST typically form a closed-loop [180] diagram with phase separation between LCST and UCST and intermixing below and above the critical points, respectively. A LLPS with LCST behavior (further referred to as LCST-LLPS) has been frequently observed, for example, in solutions of synthetic polymers [93, 94, 181, 182] and elastin-like peptides [26, 183]. In these cases, this behavior is attributed to increasing polymer-polymer interactions and polymer contraction upon temperature increase. These are accompanied by a release of water molecules surrounding their hydrophobic regions (see, *e.g.*, ref [94]). However, in aqueous solutions of globular proteins, LCST-LLPS is a so-far unexplored phenomenon with potentially interesting general implications for underlying control mechanisms of phase behavior.

Here, we report LCST-LLPS in solutions of globular, hydrophilic proteins in their native conformation, induced by the addition of trivalent cations. On the basis of the thermodynamics of the interaction between protein and metal ions, we present a picture of the underlying mechanism of the LCST-LLPS in our system. Our findings have implications for the general understanding of LCST behavior in protein and (bio)polymer systems. In addition, the thermodynamic characterization of the interaction of heavy or multivalent metal ions with proteins is also relevant for protein crystallization [82] and the understanding of biological effects of metal ions [184], e.g. in cancer treatment [185] and bacterial metabolism [186].

5.3 Experimental Methods

Bovine serum albumin (BSA) and YCl_3 were obtained from Sigma Aldrich. Protein and salt stock solutions were prepared in degassed ultrapure (18.2 MΩ) water (Merck Millipore). All samples were prepared from stock solutions. LLPS was facilitated via centrifugation. The partitioning of YCl_3 between the two phases (Fig. 5.1C) was determined by anomalous X-ray absorption (ID02 at ESRF; for technical details see Ref. 10).

Measurements of isothermal titration calorimetry and zeta potential were performed using a MicroCal iTC200 calorimeter (Malvern). YCl_3 solution (3 mM)

was titrated into BSA solution (1 mg/mL) at a stirring speed of 750 rpm and a temperature of 24 °C. The injection volumes were 0.4 μL for the first injection and 1 μL for the following ones. Each injection lasted 2 s with 180 s spacings between every two injections. A total of 30 injections were performed. A "low-gain" mode was used for the titration. The heat of dilution of the 3 mM YCl_3 solution was measured separately with the same parameters and subtracted from that of the YCl_3-protein titration as a background. The raw ITC data are shown in the Supporting Information (SI, Section 5.7).
Zeta-potential measurements were performed at 15, 20, and 25 °C using a Zetasizer Nano (Malvern), employing phase analysis light scattering. Samples were prepared by mixing appropriate volumes of BSA, MilliQ water, and YCl_3 solution and filled into zeta-potential cuvettes (Malvern). Each sample contained 1 mg/mL BSA. The concentrations of YCl_3 used were from 0.1 to 1 mM. An average zeta-potential value from five independent measurements was calculated per sample.

5.4 Results and Discussion

The LCST-LLPS behavior of bovine serum albumin (BSA)-YCl_3 systems can be directly observed by visual inspection: Fig. 5.1A shows a sample with 150 mg/mL BSA and 30 mM YCl_3 at 4 °C and 25 °C. At low T, the sample is transparent and homogeneous. When heated up to 25 °C, the solution becomes turbid and over time or after centrifugation separates into two liquid phases, protein-rich and protein-poor, with a distinct interface between them. This transition is reversible and the LCST for these sample conditions is around 13 °C (see also video in the SI [Section 5.7]). Note that BSA solutions without trivalent salt do not show LLPS, implying that the mechanism behind the phase behavior, and thus the LCST, is linked to ion-induced protein interactions [83].

To investigate the LCST behavior in more detail, we have determined LLPS binodals for different aqueous BSA-YCl_3 mixtures (Fig. 5.1B). Indeed, all binodals broaden in protein density with increasing T. We prepared several samples with a constant composition of 150 mg/mL BSA and 30 mM YCl_3 or 175 mg/mL BSA and 38 mM YCl_3, respectively, at different T's. After LLPS, the concentrations of the protein-poor phases were determined by UV absorption. The protein concentrations of the corresponding protein-rich phases were calculated according to mass conservation. This method allows the determination of the binodals for a fixed sample composition, which is essential because the salt-induced protein interactions might depend on the protein/salt ratio as well as the total concentration of the sample.

The isothermal phase behavior features a reentrant condensation with respect to salt concentration [8] and a LLPS in a closed region that is metastable with respect to crystallization [10]. Importantly, as expected for LCST behavior, the LLPS region shrinks with decreasing T (Fig. 5.1C).

Conceptually, at a fixed T, these phenomena can be understood on the basis

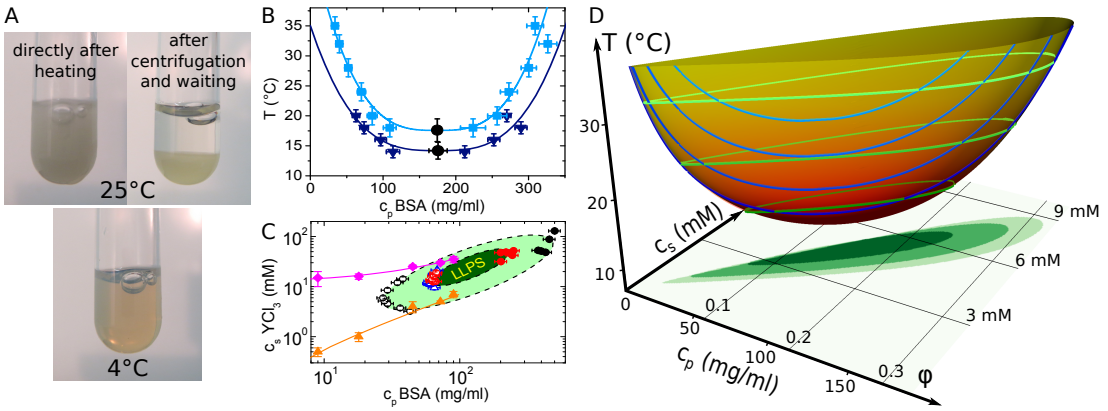

Figure 5.1: *LCST-LLPS in solutions of BSA induced by the addition of YCl_3: (A) A solution with 150 mg/ml BSA and 30 mM YCl_3 is uniform at 4°C (bottom) and phase-separates at 25°C (top). (B) The LCST behavior is systematically reflected in the binodals for two system compositions: 150 mg/mL BSA, 30 mM YCl_3 (light blue squares) and 175 mg/mL BSA, 38 mM YCl_3) (dark blue triangles). The two points (c_c, T_c) (black circles) were calculated on the basis of the critical behavior $|c - c_c|/c_c = A((T - T_c)/T_c)^\beta$ with β=0.325 corresponding to a 3D Ising system. (C) In the isothermal (c_p, c_s)-plane, LLPS of the protein solution into protein-poor and protein-rich phases occurs in a closed region (light and dark green ellipsoids). With an increase in temperature, the LLPS region broadens, reflecting the LCST behavior. Outside the LLPS region, a reentrant condensation is observed between the critical salt concentrations c* and c** (orange triangles and magenta diamonds, see refs. [8, 10] for details). (D) LCST-LLPS coexistence surface calculated for a protein model with cation-activated attractive patches with a binding free energy based on the thermodynamical characterization of the cation binding (see Figure 5.2 and text for details).*

of a combination of two effects. First, the overall protein charge is reduced and finally inverted. Second, cation bridges between different protein molecules are formed [82], representing a salt-induced interprotein attraction. This mechanism allows for a qualitative and semiquantitative description of the isothermal phase behavior [95]. However, this isothermal picture cannot explain the observed LCST behavior. A LCST implies an overall more attractive interaction with increasing temperature, which suggests an attraction of entropic origin. Thus, a thermodynamic investigation is needed to address the mechanism of the LCST behavior.

To elucidate the mechanism behind the cation-induced LCST-LLPS, we focus on the cation–protein interaction. As a first step, we measured the zeta potential, ζ, in solutions with 1 mg/mL BSA and varying YCl_3 concentration (Fig. 5.2A). The ζ-profile is consistent with a binding of cations with a positive charge, $\nu_s = 3$, to N independent binding sites on a protein with an initial negative charge Q_0

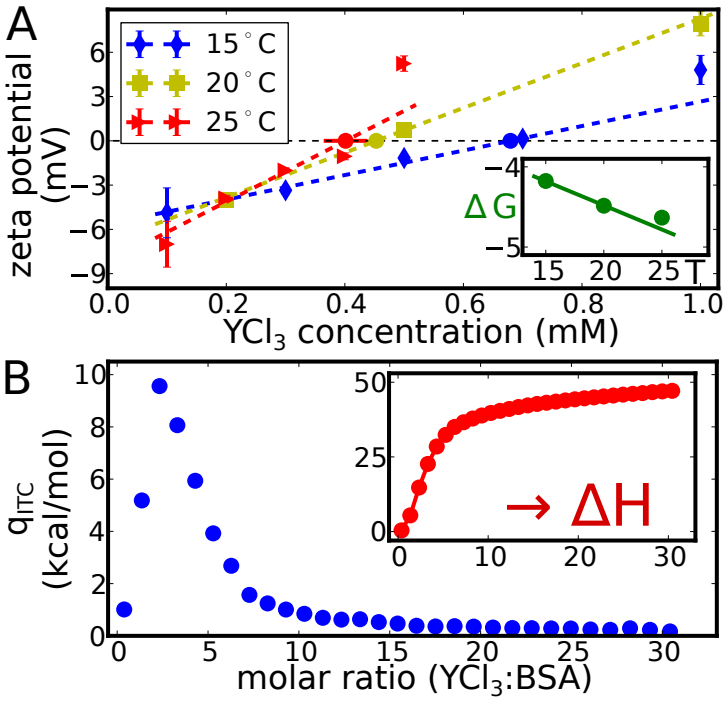

Figure 5.2: *Thermodynamic characterization of cation binding to the protein: (A) Zeta-potential measurements provide an estimation of the average free energy of binding, $\Delta G_b = \Delta H_b - T\Delta S_b$ (inset, error-weighted fit), yielding entropic and enthalpic changes upon binding. Where not visible, error bars are smaller than the symbols. (B) The positive enthalpy change upon cation binding measured by ITC evidences an entropic driving force of the cation binding.*

[83]. At a given salt concentration c_s, the net protein charge is

$$Q = Q_0 + N\nu_s \frac{c_s}{c_s + K} \tag{5.1}$$

The equilibrium constant, K, is linked to the binding free energy, $\Delta G_b' = G_{\text{bound}} - G_{\text{free}}$, via $K = \exp(\Delta G_b'/k_BT)$. Importantly, at the point of zero charge, $c_{s,0}$, electrostatic contributions to the binding are minimized, and the non-electrostatic binding free energy ΔG_b can be estimated as

$$\Delta G_b = k_BT \log\left[-c_{s,0}\left(1 + \frac{N\nu_s}{Q_0}\right)\right] . \tag{5.2}$$

Here, we use $N = 6$ and $Q_0 = -9$, which represent reasonable values for the present system [83]. Using values for ΔG_b at different temperatures, the error-weighted linear regression, $\Delta G_b = \Delta H_b - T\Delta S_b$, provides an estimation of the enthalpic and entropic changes upon binding (Fig. 5.2, inset), being fully equivalent to an error-weighted van't Hoff analysis. The estimated values are summarized in Table 5.1, and evidence directly the entropically-driven character of the cation

	$T(^\circ C)$	$c_{s,0}$ (mM)	ΔG_b	ΔH_b	$T\Delta S_b$
ζ	15	0.68 ± 0.01	-4.18 ± 0.01		17.3 ± 0.6
ζ	20	0.45 ± 0.01	-4.49 ± 0.01	13.2 ± 0.6	17.6 ± 0.6
ζ	25	0.40 ± 0.04	-4.63 ± 0.06		17.9 ± 0.6
ITC	25	—	—	15.7	—

Table 5.1: *Binding parameters in kcal/mol from isothermal titration calorimetry (ITC) and the point of zero charge $c_{s,0}$ from zeta potential (ζ) (see text).*

binding.

In a second independent approach, we measured the heat, q_{ITC}, which accompanies the binding process using ITC. The resulting enthalpy curve (Fig. 5.2B) shows the ion binding to be endothermic ($q_{ITC} > 0$). The enthalpy change per binding site, ΔH_b, can be estimated from the heat accumulated in the ITC measurements up to the molar ratio of zero charge divided by $-\nu_s/Q_0$.

The estimated values for ΔH_b in Table 5.1 from ITC and zeta potential measurements agree well, which is not expected a priori. It is important to note that zeta-potential measurements are used to extract contributions from cation-protein binding, whereas ITC results encompass all contributions, including long-ranged electrostatics. Thus, the good agreement between these two complementary techniques provides a comprehensive thermodynamic characterization of cation-protein binding and suggests that the energy contributions from the binding dominate over long-ranged electrostatics. The endothermic character of Y^{3+} binding to BSA aligns well with literature data characterizing the complex formation of trivalent cations with amino acids as an endothermic reaction [187, 188].

5.5 Conclusions

The thermodynamic signatures of cation binding obtained from zeta potential and ITC measurements imply an entropy gain upon cation binding to the protein. Because the protein remains in its native compact conformation and no strong entropic changes are expected for its internal degrees of freedom, the entropy gain of the system is dominated by that of the solvent, that is, water.

Thus, focusing on hydration effects during cation binding reveals the entropic driving force (Figure 5.3): in the unbound state, both the trivalent cations and the carboxylic binding sites are surrounded by stable hydration shells. Yttrium(III) ions in aqueous environments have been shown to be surrounded by 8–10 water molecules [189, 190]. The protein hydration shell amounts to roughly two water molecules per hydrophilic residue [191]. In the cation-bound state, a part of the water molecules from the hydration shells is released and, thus, the system entropy increases. Given the entropy cost of 2 kcal/mol at 300 K to transfer a water molecule from solution into a tight hydration configuration [192], the observed entropy change of ≈18 kcal/mol (Table 5.1) corresponds to a physically reasonable

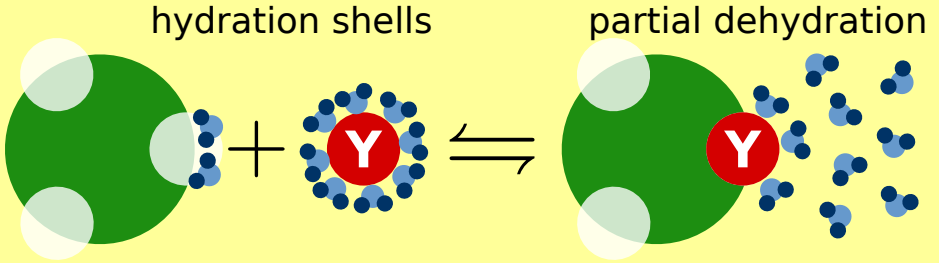

Figure 5.3: *Mechanism of LCST behavior: In the unbound state, the cations and the hydrophilic protein site are hydrated. Upon cation binding and cation bridging between proteins, water molecules are released and the system entropy is increased.*

number of released water molecules, that is, ≈9. As apparent from the ITC measurements, the endothermic contribution of broken hydrogen bonds dominates the exothermic electrostatic and the coordinative cation–carboxyl interaction. Thus, the entropy effectively drives the cation binding. Similarly, cation bridges between proteins [82, 95] formed after cation binding to the protein surface are expected to cause a release of water molecules, although presumably less pronounced. Thus, both cation binding and bridging cause an increase in entropy and, consequently, become more pronounced at *higher* T. It is important to note that additional entropic contributions such as translational entropy of water also lead to UCST behavior in our system. However, this behavior cannot be observed due to the fact that proteins denature above a certain T, thereby changing the system before the UCST is reached.

The thermodynamic characterization of the cation-protein interaction allows us to extend the theoretical modeling from isothermal conditions to a conclusive mechanistic picture of LCST-LLPS: Fig. 5.1D displays the LCST-LLPS phase diagram depending on the two control parameters c_s and T, as calculated from a coarse-grained protein model with $N = 6$ cation-activated attractive patches (for theoretical background, see Ref. 95). We used the temperature-dependent binding free energy, $\varepsilon_b = \Delta H_b - T\Delta S_b$, derived from zeta-potential measurements (Table 5.1). For the cation-bridging free energy, $\varepsilon_{uo} = \Delta H_{\text{bridge}} - T\Delta S_{\text{bridge}}$, we choose $\Delta H_{\text{bridge}} = 8\,\text{kcal/mol}$ and $T\Delta S_{\text{bridge}} = 17.9\,\text{kcal/mol}$ (at 25 °C). The resulting coexistence surface reproduces the experimental binodals and thus enables a conceptual understanding of the LCST behavior.

Summarizing the thermodynamic mechanism, cation binding to protein functional groups causes a partial dehydration and is driven by the entropy difference between hydration and bulk water. With increasing T, cation binding becomes more effective, and consequently, cation bridges between protein molecules represent a stronger attraction. Thus, the coexisting surface opens up at higher T as observed in the T-dependent binodals (Fig. 5.1B), and in the differences among different isothermal planes (Fig. 5.1C).

Generally, hydration effects are well known to be important in biology [193] and

to affect the phase behavior of polymer and protein solutions [194, 195]. However, hydration effects do not per se induce LCST behavior. In fact, lysozyme solutions show UCST-LLPS even under extreme conditions, such as for partially collapsed hydration shells due to pressure [179] or hydration enhanced by glycerol [178]. Apart from the system discussed here, LCST-LLPS in protein solutions has only been reported for hemoglobin in the presence of poly(ethyleneglycol) [63]. LCST behavior of protein solubility, a so-called retrograde solubility, has been observed for hemoglobin [196] and equine serum albumin in concentrated ammonium sulfate solutions [197]. However, although expected from theoretical considerations, once significant entropic contributions of the solvent are present [198–200], LCST behavior is still rather uncommon in protein solutions, whereas it is well-known in polymer solutions where it is usually explained by effects of (hydrophobic) hydration [180], accompanied by changes in molecular conformations [26].

The different behaviors of proteins and (bio)polymers can be rationalized by differences in the surface patterns, in particular the regularity. Synthetic polymers and elastin-like peptides consist of periodically repeating units containing hydrophilic and hydrophobic parts. By contrast, proteins exhibit an irregular distribution of hydrophobic and hydrophilic patches on the solvent-exposed surface. Frequently, LCST is explained by a hydration shell that breaks up at higher temperature, and subsequently allows for polymers to condense. However, a breakup of the hydration shells alone does not explain condensation. A second requirement is an attraction between compatible surface patterns which in turn also stabilizes the dehydration. Thus, LCST behavior in (bio-)polymer solutions is realized by a cooperative process of dehydration and surface-pattern-induced attraction, both of which are eventually driven by entropic contributions due to the release of water from a hydration shell into the bulk.

Thus, we present a simple rationalization of the difference between the LCST behaviors of proteins and polymers: the attraction of polymers can be more or less rationally designed through the choice of the repeating unit and the related hydrophobic pattern. By contrast, the conformation of globular proteins evolved over millions of years within the constraint of solubility. Consequently, hydrophobic and protein surface charge patterns generally ensure an overall repulsion of proteins within the biological temperature window. The addition of multivalent cations and thus attraction via interprotein cation bridges disturb the subtle interplay of protein interactions and eventually allow for LCST behavior.

In summary, we have observed a LCST phase behavior in aqueous BSA solutions induced by multivalent cations. The LCST is reflected in a LLPS that takes place above a certain temperature. We have identified the entropy-driven thermodynamic character of the cation–protein binding and protein–protein bridging. The reported LCST behavior can be explained as a result of cation binding and bridging between protein molecules. Importantly, the cation-protein interaction is driven by entropy changes of water molecules that are released from the hydration shells of both cation and protein upon binding. The thermodynamic characterization of the protein–cation interaction in this particular system is important

for the general understanding of cation effects in biological and soft matter systems. The experimental and theoretical evidence of the LCST-LLPS presented here along with the picture of the underlying mechanism is promising for a better understanding and control of phase transitions in aqueous protein solutions and has general implications for hydration- and cation-mediated effects in soft matter systems.

5.6 Acknowledgement

We acknowledge discussions with R. Akiyama (Kyushu), T. Narayanan (Grenoble), M. Dolg (Cologne), B. Höcker, S. Da Vela and G. Zocher (Tübingen), and S. Sukharev (Maryland). We thank T. Stehle, F. Bono, T. Lahaye (Tübingen), and the PSCM (Grenoble) for sharing lab resources. We thank S. Shanmugaratnam and C. Wolf (Tübingen) for assistance during ITC measurements. O.M. acknowledges a fellowship by the Studienstiftung des Deutschen Volkes. We thank the DFG for financial support and the ESRF for beamtime allocation on beamline ID02.

5.7 Supporting Information

5.7.1 Raw ITC data

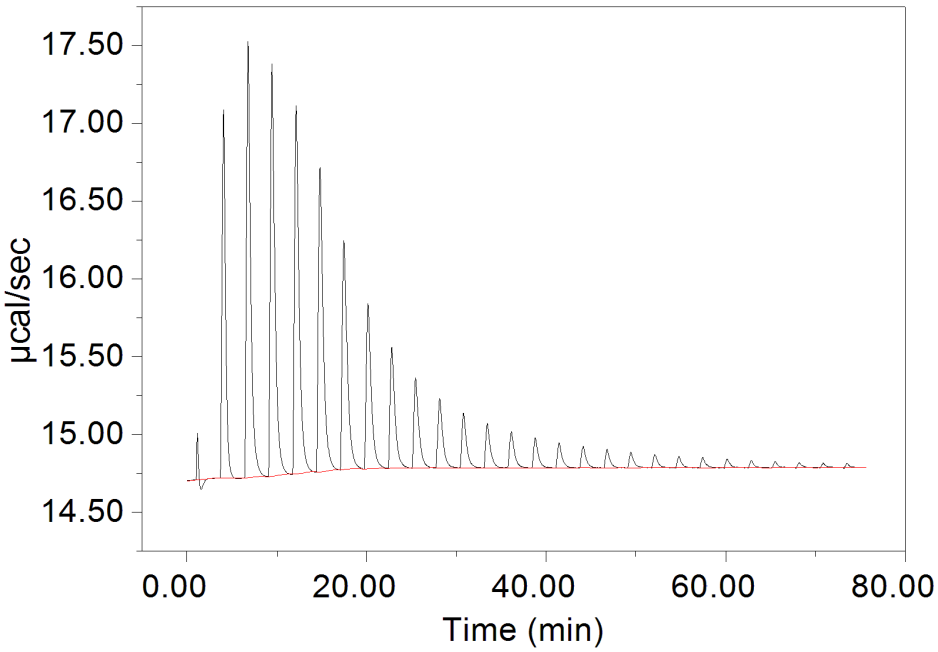

Figure 5.4: *Raw ITC data obtained for the titration of 1 mM YCl_3 into a 1 mg/ml solution.*

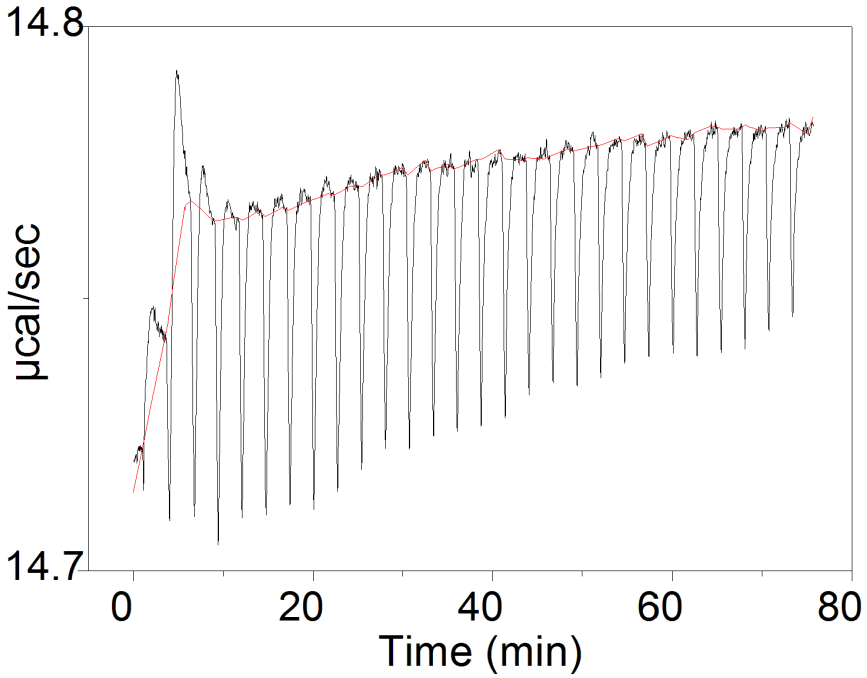

Figure 5.5: *Raw ITC data obtained for the titration of 1 mM YCl_3 into water. This data represents the heat of dilution of YCl_3 in water and was used for background correction of the data shown in Fig. 5.4.*

5.7.2 Movie showing reversible LCST behavior of a BSA-YCl_3 sample

Movie description: two vials containing equal phase-separated BSA-YCl_3 samples (175 mg/ml BSA, 38 mM YCl_3) are shown. One of the vials is immersed into hot water (40 °C) while the second one is placed into cold water. The sample immersed into hot water shows LCST-LLPS and becomes highly turbid, while no change is observed for the sample kept in the cold water. The sample positions are then switched. The turbid sample becomes clear again while the clear sample becomes turbid. This heating-cooling cycle can be repeated many times with no signs of irreversibility of the LCST-LLPS behavior.

The movie is available *via* the URL https://pubs.acs.org/doi/suppl/10.1021/acs.jpcb.6b04506 (24.32 MB).

Chapter 6

Tuning phase transitions of aqueous protein solutions by multivalent cations

The following is reproduced from Ref. 201 with permission from the PCCP Owner Societies.

6.1 Abstract

In the presence of trivalent cations, negatively charged globular proteins show a rich phase behaviour including reentrant condensation, crystallisation, clustering and lower critical solution temperature metastable liquid-liquid phase separation (LCST-LLPS). Here, we present a systematic study on how different multivalent cations can be employed to tune the interactions and the associated phase behaviour of proteins. We focus our investigations on the protein bovine serum albumin (BSA) in the presence of $HoCl_3$, $LaCl_3$ and YCl_3. Using UV-Vis spectroscopy and small-angle X-ray scattering (SAXS), we find that the interprotein attraction induced by Ho^{3+} is very strong, while the one induced by La^{3+} is comparatively weak when comparing the data to BSA-Y^{3+} systems based on our previous work. Using zeta potential and isothermal titration calorimetry (ITC) measurements, we establish different binding affinities of cations to BSA with Ho^{3+} having the highest one. We propose that a combination of different cation features such as radius, polarisability and in particular hydration effects determine the protein-protein interaction induced by these cations. Our findings imply that subtle differences in cation properties can be a sensitive tool to fine-tune protein-protein interactions and phase behaviour in solution.

6.2 Introduction

A thorough understanding of phase transitions in protein solutions is of utmost importance for the design and stabilisation of protein-based therapeutics [3, 4], disentangling cell-signalling processes [18], finding treatment options for protein condensation diseases [17] as well as rationally manipulating pathways of protein

crystallisation [82]. The heterogeneous charge distribution and intricate interactions with their environment — the latter can additionally be influenced by various parameters including temperature, pH and pressure — make proteins highly complex molecules. In an attempt to better understand and investigate proteins and their interactions with their surroundings, it is thus helpful to make use of simplified physical models.

In this context, the framework of colloid theory with corresponding model interaction potentials provides a successful approach. An important insight from colloid science describes the influence of the interaction range between particles on their phase behaviour. Specifically, interparticle attraction on a range smaller than the particle diameter is reflected in a metastable liquid-liquid coexistence region which shifts below the gas-crystal line [49, 50, 55, 57]. This liquid-liquid coexistence, also referred to as liquid-liquid phase separation (LLPS), can be considered analogous to the liquid-gas transition in the van der Waals gas [42]. The experimental evidence for this phenomenon in colloidal systems, which also laid the foundation for its subsequent theoretical rationalisation by Gast *et al.* [31], was provided by Sperry and co-workers [32] in a latex-polymer system with depletion attraction.

Importantly, such phenomena can also be observed in protein solutions. One of the earliest observations of LLPS in a protein system was documented by Tanaka *et al.* for an aqueous lysozyme-NaCl mixture [56]. Since then, many more examples of LLPS in different protein solutions have been described. Examples include crystallins [58–61], different types of hemoglobin [62–64], lysozyme [57, 65], polypeptides derived from elastin [66] as well as cellular structures [21].

Under physiological conditions, proteins and their interactions are influenced by cations such as Na^+, K^+, Ca^{2+}, Mg^{2+} or Zn^{2+} [1]. Moreover, many proteins, notably serum albumins, can directly bind and transport cations [72]. In addition to these physiologically occuring cation species, the interactions of proteins with less common cations such as lanthanides (Ln) are of fundamental interest in toxicology [202, 203], the onset and development of neurodegenereative diseases[204, 205], bacterial metabolism [186], tumour treatment [185, 206] as well as spectroscopic [207] and diagnostic methods [112, 208, 209]. Cation-specific effects are not limited to proteins, but similarly occur in soft matter systems. For example, a recent study by Yu *et al.* [210] showed a strong decrease in polyelectrolyte brush lubricity upon the addition of multivalent cations such as Y^{3+}.

Throughout the past years, our group has successfully established a rich phase behaviour induced in negatively charged globular proteins by trivalent salts such as YCl_3. It has been found that Y^{3+} cations introduce a short-range attraction between the protein molecules by forming cation bridges between negatively charged residues of protein molecules [82], leading to a variety of phenomena including crystallisation [10, 11, 82], cluster formation [11], reentrant condensation [8, 10, 83], and metastable LLPS [11] with a lower critical solution temperature (LCST-LLPS) [13, 14, 89].

A representative salt-protein concentration ($c_s - c_p$) phase diagram of a nega-

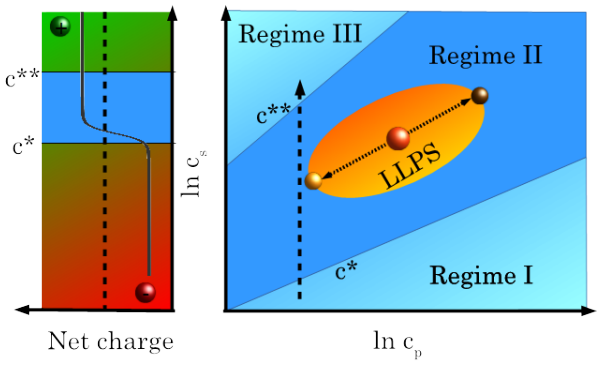

Figure 6.1: *Phase diagram showing regimes I, II and III, reentrant condensation and LLPS. See text for details.*

tively charged globular protein in the presence of a trivalent salt describing our experimental systems is shown in Fig 6.1. The dashed arrow in the right part shows the phase transitions at constant c_p upon increasing c_s. In regime I, at low c_s, few cations bind to protein molecules. The overall protein surface charge is negative (left part of Fig. 6.1) and the net interactions are thus repulsive. An increasing c_s leads to a weakened protein surface charge and a subsequent condensation of the protein solution. This area of the phase diagram is referred to as regime II and is separated from regime I by a critical salt concentration c^*. Under appropriate conditions, a sample located in a certain region of the phase diagram (orange sphere on yellow ellipsoid) can undergo liquid-liquid phase separation into a protein-rich and a protein-poor phase (brown and yellow spheres on the high- and low-c_p edges of the yellow ellipsoid, respectively), which is due to a short-range interprotein attraction induced by cation bridging [10]. An even further increase of c_s leads to a charge inversion of the protein surface due to an extensive binding of cations upon crossing a second critical salt concentration c^{**}. These experimental findings can be rationalised from a theoretical point of view in the framework of an ion-activated patchy particle model [95] which combines a hard-sphere repulsion of the proteins and a square-well attraction induced by cations binding to patches (negatively charged amino acid residues) on the protein surface. This mechanism features similarities to cation-mediated condensation of DNA [211, 212]. Interestingly, molecular dynamics and Monte Carlo studies by Pasquier *et al.* [213] show an anomalous development of the protein-protein potential of mean force with increasing salt concentration in a system of human serum albumin (HSA) and YCl_3. The results obtained by Pasquier *et al.* [213] are in excellent agreement with the different regions of the experimental phase diagram shown in Fig. 6.1.

Previous studies showed that this phase behaviour also depends on the choice of the salt. We have found that trivalent salts other than YCl_3 (such as $FeCl_3$ and $AlCl_3$) also induce reentrant condensation. However, we established that as opposed to YCl_3, pH effects on the reentrant phase behaviour due to salt hydrolysis

are significant in the case of $FeCl_3$ and $AlCl_3$ [83]. Furthermore, we found that for a protein solution with fixed YCl_3 concentration, the addition of a monovalent salt could be used to shift the phase boundaries to higher critical concentrations, suggesting a subtle balance of charge repulsion and salt-induced attraction to be essential for the phase behaviour [214]. The effect of different counterions of lanthanide cations on the phase behaviour of BSA is subject of a recent investigation [106].

Given that details of the interaction potential have a strong influence on the phase behaviour of colloidal systems, we aim at investigating the influence of cations with different radii and chemical properties (Ho^{3+}, La^{3+} and Y^{3+}). Note that none of these cations cause strong pH effects by hydrolysis, and therefore the changes observed are due to different effective interactions due to subtle differences in the cation properties. Our main interest consists in fine-tuning and controlling the phase behaviour of protein solutions using different cations.

In the present work, we first describe macroscopic observations which evidence that different trivalent cations lead to remarkably strong differences in the phase behaviour of bovine serum albumin (BSA). Determining transition temperatures of different protein-cation mixtures by UV-Vis spectroscopy, we observe a strong interprotein attraction induced by Ho^{3+} in BSA solutions, whereas these attractions are weaker in the presence of La^{3+}. Systems consisting of BSA and Y^{3+} are used as a reference. Reduced second virial coefficient values (B_2/B_2^{HS}) obtained from small-angle X-ray scattering (SAXS) confirm this conclusion. In addition to cation-induced protein interactions, we study cation binding to BSA by zeta potential measurements and isothermal titration calorimetry (ITC) to obtain a comprehensive thermodynamic characterisation of cation-protein interactions.

6.3 Materials

Bovine serum albumin (BSA, product no. A7906), YCl_3, $HoCl_3$ and $LaCl_3$ were purchased from Sigma Aldrich (Taufkirchen, Germany, now Merck, Darmstadt, Germany) and used without further purification. Protein and salt powders were dissolved in ultrapure degassed water (18.2 MΩ, Merck Millipore, Darmstadt, Germany). The exact protein concentration was determined using UV-Vis spectroscopy (Cary 50 UV-Vis spectrometer, Varian Inc., now Agilent Technologies, California, USA; absorbance at 280 nm). Samples were subsequently prepared by mixing appropriate volumes of aqueous protein and salt stock solutions.

6.4 Experimental Methods

6.4.1 Isothermal coexistence phase diagrams

c_s-c_p phase diagrams were determined at room temperature for 80 mg ml^{-1} (1.2 mM) BSA and increasing concentrations of $HoCl_3$, $LaCl_3$ and YCl_3. The dilute phases

were studied by visual inspection and light microscopy. Samples with dilute phases that were homogeneous under the microscope but appeared turbid upon visual inspection were classified as "turbid". Where liquid-liquid phase separation was visible under the microscope, the samples were labelled as "LLPS". In the absence of any inhomogeneity, samples were classified as "clear".

6.4.2 T-dependent UV-Vis spectroscopy

All of the BSA-trivalent cation systems studied here show a LCST-LLPS-type behaviour. To elucidate the differences in protein-protein interactions induced by the different cations, cation mixtures were used. In order to determine the respective transition temperatures T_{trans} from homogeneous to phase-separated states of the BSA-cation mixtures, temperature-dependent UV scans were performed using a Cary 50 UV-Vis spectrometer (Varian Inc., now Agilent Technologies, California, USA) connected to a water bath (Haake A 10B, Thermo Fisher Scientific, Schwerte, Germany). Samples were then subjected to temperature scans at a rate of 0.1 K/min while their absorbance was monitored over a wavelength range from 400 to 800 nm. The intensity values of the spectra obtained were summed and divided by the respective number of data points. T_{trans} was determined from the maximum of the first derivatives with respect to temperature of the respective curves.

6.4.3 Zeta potential measurements

Zeta potentials were measured by electrophoretic light scattering (ELS) using a Nano Zetasizer (Malvern Instruments, Malvern, United Kingdom). Samples containing 1 mg ml^{-1} (15 µM) BSA and increasing salt concentrations (0.1, 0.3, 0.5, 0.7 and 1 mM of $HoCl_3$, YCl_3 or $LaCl_3$) were prepared shortly before the measurements. The low BSA concentration was chosen to avoid phase separation of the samples. Every sample was measured at 5 different temperatures, with 10 min of equilibration time before each measurement. The ζ potential values were subsequently converted into effective surface charge values Q in units of elementary charge e as explained in the ESI † (Section 6.9).

6.4.4 Isothermal titration calorimetry (ITC)

ITC measurements were performed using a MicroCal iTC200 (Malvern Instruments, formerly GE Healthcare). Salt solutions with concentrations of 800 µM or 3 mM were titrated into 1 mg ml^{-1} (15 µM) BSA solutions in 0.5 µl steps with a duration of 1 s each. A preliminary titration step of 0.2 µl with a duration of 0.5 s was used for equilibration. In the case of the titrations performed with 3 mM salt solution, the durations of these steps were 0.4 and 1 s, respectively. In

order to correct for the heat of dilution of the salt, a background measurement was performed by titrating the 800 µM or 3 mM salt solutions into water. The background measurements were subtracted from the salt-protein measurements. For each measurement, 60 injections were performed in total. The time interval between each injection was 90 s with a filter period of 5 s. For titrations with 3 mM salt solutions, these time intervals were 180 and 2.5 s, respectively. The stirring speed of the syringe was 750 rpm and the reference power was set to 1.3 µcal/sec. All data sets were taken at 24 °C.

6.4.5 Small-angle X-ray scattering (SAXS)

SAXS measurements were performed at beamline ID02 (ESRF, Grenoble, France) at a sample-detector distance of 2 m and an energy of 12.46 or 16 keV (λ = 0.8-0.9 Å). The scattered intensity was recorded using a Rayonix MX160 or a FReLoN Kodak CCD detector, covering a q range from 0.04 to 4 nm^{-1}.
Samples containing 80 or 85 mg ml^{-1} (= 1.2 or 1.3 mM) BSA and increasing (0-50 mM) concentrations of $HoCl_3$, $LaCl_3$ or YCl_3 were prepared at room temperature (ca. 21 °C) and centrifuged for 5 min at 9500 rcf to facilitate phase separation for those samples located in the LLPS region of their respective phase diagrams. Samples were loaded into a flow-through capillary and measured at a constant temperature of 20 °C controlled by a Peltier element connected to the flow cell. In the case of phase-separated samples, the dilute phases were measured. Per sample, 5-10 acquisitions were performed with an exposure time of 0.05-0.1 s. The data were calibrated to absolute intensity using water as a reference [215]. Data were averaged and background-corrected using either water or pure salt solutions with appropriate concentrations.
In a SAXS experiment, the scattering intensity $I(q)$ is measured as a function of momentum transfer $q = \frac{4\pi}{\lambda}\sin(\theta)$ with a scattering angle 2θ [126]. It can be expressed as

$$I(q) = \Phi V_{particle}(\Delta\rho)^2 P(q) S(q) \tag{6.1}$$

where $V_{particle}$ represents the volume of a particle (i.e. protein) in question, Φ the volume fraction of particles in the sample and $\Delta\rho$ the scattering contrast between solvent and particles. $P(q)$, the form factor of the particles, represents the Fourier transform of their respective electron densities.

In systems with sufficiently high particle concentrations where intermolecular interactions cannot be neglected, the latter are accounted for by the structure factor

$$S(q) = 1 + 4\pi\rho \int_0^\infty dr\ r^2 h(r) \frac{\sin(qr)}{qr} \tag{6.2}$$

where $\rho = N/V$ and $h(r) = g(r) - 1$ is the total correlation function [37].

Importantly, the structure factor at $q \to 0$ is proportional to the osmotic compressibility $(\partial\Pi/\partial c)^{-1}$ of the system in question [133, 134] which can be expanded into a series of virial coefficients A_n [133, 135]:

$$S(q \to 0) = \frac{RT}{M}\left(\frac{\partial\Pi}{\partial c}\right)^{-1} = \frac{1}{1 + 2MA_2c + ...} \tag{6.3}$$

where $R = 8.314$ JK^{-1}mol^{-1} is the ideal gas constant, T is the temperature and M is the molecular weight of the particles investigated. The second virial coefficient B_2 is related to A_2 via [136]

$$B_2 = A_2 \cdot \frac{M^2}{N_A} \tag{6.4}$$

where N_A is Avogadro's constant ($6.022{\cdot}10^{23}$ mol^{-1}). In this study, the normalised second virial coefficient B_2/B_2^{HS} (with $B_2^{HS} = 2\pi\sigma^3/3$ being the second virial coefficient of a system consisting of hard spheres with diameter σ [68]) is calculated from the SAXS profiles in order to characterise the overall nature of their interactions.

For c_s = 0-3 mM, the form factor was combined with a screened Coulomb (SC) structure factor [216, 217]. The screened Coulomb potential is expressed as

$$\beta U(x) = \begin{cases} \gamma e^{-kx}/x & (x > 1) \\ \infty & (x \leq 1) \end{cases} \tag{6.5}$$

where $x = r/\sigma$ (interparticle distance normalised by particle diameter) and $k = \kappa\sigma$ with κ being the Debye screening length. β is in units of $(k_BT)^{-1}$ and $\gamma e^{-k} = \beta\pi\epsilon_0\epsilon\sigma\psi_0^2$ (ϵ_0 is the vacuum permittivity, ϵ the permittivity of the solvent, σ the particle diameter and ψ_0 the surface potential) represents the potential upon contact of two particles (in this case, proteins).

For $c_s \geq 4$ mM, a sticky hard sphere structure (SHS) factor was used [52, 218, 219]. The SHS potential is expressed as [52]

$$U(r) = \begin{cases} \infty, r \leq \sigma \\ -\epsilon, \sigma < r \leq \lambda\sigma \\ 0, \lambda\sigma < r \end{cases} \tag{6.6}$$

where the range of the attractive part of the potential, R, is equal to $\lambda - 1$. The stickiness parameter τ is defined *via* [52, 219]

$$\tau^{-1} = 4[\exp(-\epsilon/k_BT) - 1][(a - \sigma)^3 - 1] \tag{6.7}$$

where $a = \sigma + \Delta$ and Δ is the attractive well width [219].

From τ, the reduced second virial coefficient is obtained *via* $B_2/B_2^{HS} = 1 - 1/(4\tau)$ [68]. The fitting routine using the software Igor PRO [137] employed here has been described in detail elsewhere (see Refs. [10, 84, 89]).

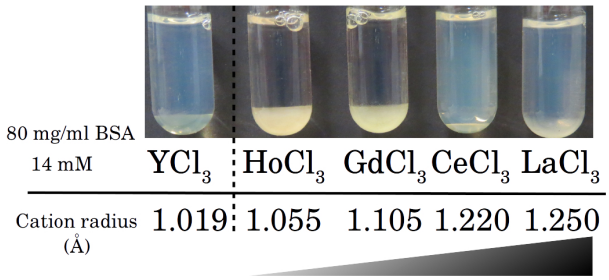

Figure 6.2: *Comparison of dense phases of liquid-liquid phase separated samples containing 80 mg ml^{-1} BSA and different trivalent salts. The protein concentration (c_p) is 80 mg ml^{-1}, the salt concentration (c_s) is 14 mM in every sample. All samples are located in the LLPS region of regime II of their respective c_s-c_p phase diagrams. Note that the dense phases obtained in the presence of Ho^{3+} and Gd^{3+} may correspond to an arrested state (see text for details). The cationic radii of the lanthanides are obtained from Ref. 108 and that of Y^{3+} from Ref.107. The dashed vertical line between YCl_3 and $HoCl_3$ indicates that YCl_3 is used as a reference system.*

6.5 Results

6.5.1 Macroscopic properties of phase-separated samples

Fig. 6.2 shows a series of samples consisting of aqueous solutions of 80 mg ml^{-1} (=1.2 mM) BSA and the same concentration (14 mM) of different trivalent salts prepared at 21 °C. In the sample containing YCl_3, a moderate amount of a clear, yellowish, dense liquid phase is observed, consistent with earlier observations [8, 13, 82]. The samples made with $HoCl_3$ and $GdCl_3$ form a substantial amount of dense phase; the dense phases are opaque, but still flow slowly. Using $CeCl_3$ leads to a strong decrease of the amount of dense phase, which in this case is transparent. When $LaCl_3$ is used, no dense phase is formed at 21 °C (see also Ref. 89). The diffuse turbid region at the bottom of this sample and in the dilute phases of the samples prepared with YCl_3 and $CeCl_3$ is presumably due to cluster formation in regime II. This macroscopic observation thus indicates differences in protein-protein and protein-salt interactions induced by the different lanthanide salts used. Based on Fig. 6.2, the strongest protein-protein interactions are expected for $HoCl_3$ and the weakest ones for $LaCl_3$. We therefore focused our studies on $HoCl_3$ and $LaCl_3$, using YCl_3 as a reference system based on extensive previous work [8, 10–12, 82].

6.5.2 Isothermal coexistence c_s-c_p phase diagram

As a first step towards a more quantitative description of the phase behaviours of our systems, phase diagrams were established for BSA in the presence of YCl_3, $LaCl_3$ and $HoCl_3$. Homogeneous samples with salt concentrations below c^* and

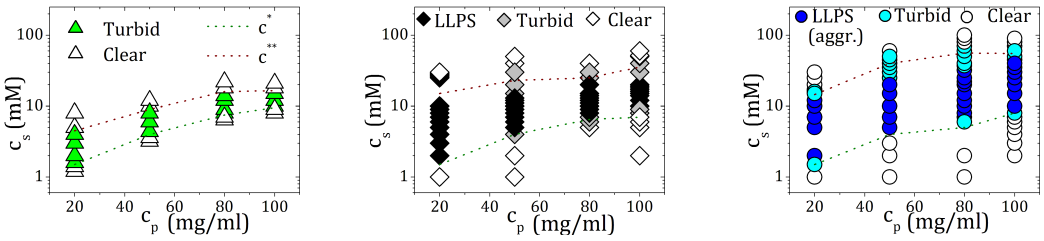

(a) *BSA + $LaCl_3$.* *(b)* *BSA + YCl_3.* *(c)* *BSA + $HoCl_3$.*

Figure 6.3: *Isothermal phase diagrams of BSA in the presence of $LaCl_3$, $HoCl_3$ and YCl_3. Data in (a) are replotted based on Ref. 89. In the presence of $HoCl_3$, the dense phases formed feature network-like structures which may indicate aggregation. Nevertheless, these samples still show LCST behaviour and are therefore classified as showing both aggregation and LLPS.*

beyond c^{**} as well as liquid-liquid coexistence diagrams of phase-separated samples in regime II are shown in Fig. 6.3.

Fig. 6.3 illustrates the differences in the isothermal phase behaviour of BSA induced by the three different salts studied here. The most striking feature is the complete lack of LLPS at room temperature when $LaCl_3$ is used [89]. Using $HoCl_3$, however, leads to a rather broad region of LLPS, larger still than the one induced by YCl_3. The BSA-$HoCl_3$ one shows more aggregation than the BSA-YCl_3 one. A detailed characterisation of the properties of these dense phases is beyond the scope of the present publication. Nevertheless, the presence of aggregates suggests that the dense phases of the BSA-Ho^{3+} system may be in an arrested state caused by a stronger intermolecular attraction, as observed for other protein systems [65]. This interpretation is further supported by the observation that dense BSA-Ho^{3+} (and BSA-Gd^{3+}) phases appear turbid after preparation, but can mature into clear dense phases after several weeks.

6.5.3 Temperature-dependent UV spectroscopy

As an alternative route to investigate the effect of different cations on the macroscopic phase behaviour of our experimental systems, we systematically determined the cloud temperature T_{trans} for BSA in the presence of cation mixtures. Fig. 6.4 shows a typical data set obtained for a constant BSA concentration of 80 mg ml^{-1} (1.2 mM). The total salt concentration was also kept constant at 10 mM while increasing the $HoCl_3$ fraction and simultaneously decreasing that of $LaCl_3$. Similar scans were also performed using different YCl_3/$LaCl_3$ and YCl_3/$HoCl_3$ ratio combinations. The transition temperature T_{trans} of each system was determined as the maximum of the first derivatives with respect to temperature of the respective integrated absorbance curves.

In order to quantify the influence of different cations on T_{trans} of the different

cation mixtures, the differences in T_{trans} values (ΔT_{trans}) between different mixtures and samples containing 100 % YCl_3 (the T_{trans} of which is 30.6 °C) were calculated (Fig. 6.5). As can be seen from the rightmost part ($HoCl_3$/$LaCl_3$ mixtures), the strongest ΔT_{trans} (-15 °C) is obtained in a mixture of 20 % $LaCl_3$ and 80 % $HoCl_3$. In other words, with higher fractions of $HoCl_3$, the samples phase-separate already at lower T. This is also the lowest overall ΔT_{trans} observed amongst all mixtures investigated and supports the hypothesis that Ho^{3+} cations induce the strongest interprotein attraction of all cations studied here. This conclusion is also reflected in the fact that samples containing $HoCl_3$ percentages higher than 80% already phase-separate at 12 °C, the initial equilibration temperature for the measurements presented here. Due to this behaviour, no measurements of BSA-$HoCl_3$/$LaCl_3$ samples containing more than 80% $HoCl_3$ could be performed. When mixtures of YCl_3 and $HoCl_3$ (leftmost part of Fig. 6.5) are considered, any sample with a $HoCl_3$/YCl_3 ratio higher than 50/50 also phase-separates already at 12 °C. The higher the fraction of $HoCl_3$, the higher the T_{trans} difference to a sample containing only YCl_3. Again, this indicates a strong interprotein attraction induced by Ho^{3+}.
In the case of YCl_3/$LaCl_3$ mixtures (central part of Fig. 6.5), the highest ΔT_{trans} is obtained with the highest $LaCl_3$ concentration. This implies that addition of $LaCl_3$ shifts T_{trans} towards higher values, confirming that Y^{3+} cations induce a stronger interprotein attraction than La^{3+} cations. Based on these measurements, the cations can be ranked according to the order of increasing cation-induced protein-protein interaction strengths as $La^{3+} < Y^{3+} < Ho^{3+}$.

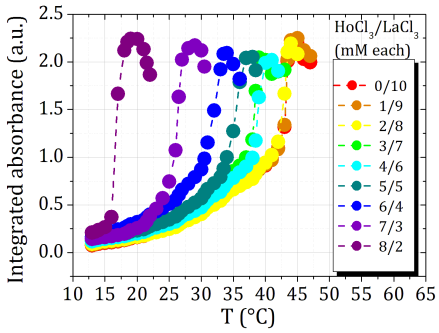

Figure 6.4: *Typical series of T-dependent absorbance measurements (raw data) of samples containing a constant c_p of 80 mg/ml (1.2 mM) BSA and a constant total ionic strength of 10 mM consisting of different salt ratios (here: $HoCl_3$ & $LaCl_3$). Similar series were also recorded for mixtures of $HoCl_3$ & YCl_3 as well as YCl_3 and $LaCl_3$. T_{trans} values of all samples were compared to a sample with 10 mM pure YCl_3 (Fig. 6.5).*

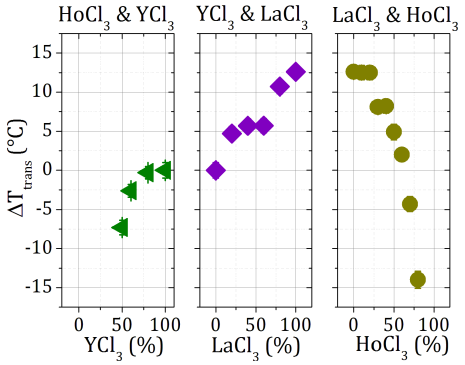

Figure 6.5: *Difference between T_{trans} values determined for each sample consisting of BSA and a cation mixture and T_{trans} of a sample containing 80 mg/ml BSA and 10 mM pure YCl_3. Where not visible, error bars are smaller than the data symbols.*

6.5.4 Effective interactions characterised by small-angle X-ray scattering

Small-angle X-ray scattering (SAXS) was performed in order to characterise the influence that the different cations investigated have on the protein-protein interactions of BSA. Background-corrected SAXS data obtained for BSA in the presence of an increasing $HoCl_3$ concentration are shown in Fig. 6.6.

Fig. 6.6 shows that the intensity at low q, $I(0)$ increases and decreases in an alternating fashion. The intensity $I(0)$ at low q was used to qualitatively estimate the strength of the interactions in the systems investigated (Fig. 6.7).

Fig. 6.7 shows three c_s/c_p regimes with consistent results: first, for $c_s/c_p < 7$, $1/I(0)$ behaves comparably for all cations, with a slightly lower $1/I(0)$ for Ho^{3+}. For c_s/c_p in the range from 7 to 22, the different phase behaviours induced by Ho^{3+}, Y^{3+} and La^{3+} are reflected in the strengths of the respective humps. While no hump is observed for La^{3+}, the humps for Ho^{3+} and Y^{3+} are related to the reduced protein concentration in the dilute coexisting phases. As in Fig. 6.3, the LLPS appears more prominent for $HoCl_3$ (i.e. the density difference between the corresponding dense and dilute phases is larger) than for YCl_3, and is absent for $LaCl_3$. Finally, at higher c_s/c_p (> 22), $1/I(0)$ follows the order $Ho^{3+} < Y^{3+} < La^{3+}$. Together with the trend towards lower T_{trans} values for samples containing $HoCl_3$ (Fig. 6.5), all these features indicate an interprotein attraction decreasing in the sequence $HoCl_3 > YCl_3 > LaCl_3$, consistent with the above UV-Vis absorbance data in Section 6.5.3.

In order to further quantify the cation-induced protein-protein interactions, the SAXS curves were treated as follows: for salt concentrations $c_s <$ 6 mM, data were fitted using a screened Coulomb (SC) potential structure factor; at higher salt concentrations, a sticky hard sphere (SHS) potential structure factor was used (see model fit in Fig. 6.6). From the curves fitted with the SHS structure

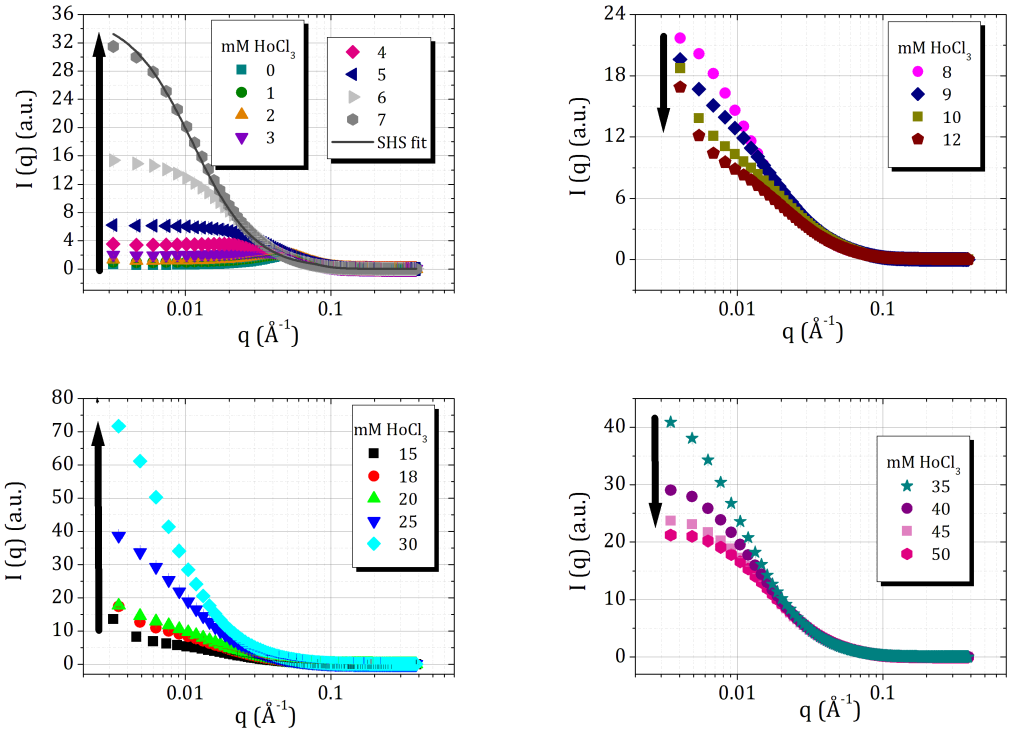

Figure 6.6: *SAXS profiles of BSA with increasing $HoCl_3$ concentrations. Samples were prepared at a protein concentration of 85 mg ml^{-1} (1.3 mM). In case of phase separation, the SAXS measurements were performed in the dilute phase. Data were normalised to the high q region of a BSA sample without salt (0 mM $HoCl_3$) and only every 5th data point was plotted for clarity. The dark grey line in the top left part represents an SHS model fit (as also done for the other curves, but omitted for clarity) to the curve obtained in the presence of 7 mM $HoCl_3$.*

factor, stickiness parameters τ were extracted and used to calculate the reduced second virial coefficients ($B_2/B_2^{HS} = 1-1/(4\tau)$ [68]). Being related to the osmotic compressibility of the system investigated (see Methods section), these values can be used as a means to determine the overall strength of the interactions of the system in question. In particular, a positive B_2/B_2^{HS} indicates overall repulsion whereas negative values indicate net attraction. A value around -1.5 moreover indicates proximity to the critical point of LLPS in colloidal theory [138]. The B_2/B_2^{HS} values obtained for BSA in the presence of $HoCl_3$, $LaCl_3$ and YCl_3 are shown in Fig. 6.8 as functions of the c_s/c_p ratio.

The B_2/B_2^{HS} values obtained for the BSA-$LaCl_3$ system show that these samples nearly always show net attractive interactions, but, as confirmed by macroscopic experimental data, do not phase-separate under the given conditions. In the BSA-YCl_3 and BSA-$HoCl_3$ systems, however, the B_2/B_2^{HS} values indicate phase separation, as is confirmed from macroscopic observations. The systems containing YCl_3 and $HoCl_3$ therefore feature overall stronger attractive interactions.

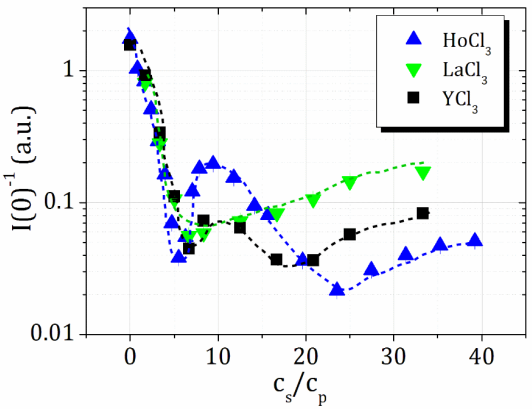

Figure 6.7: *Inverse $I(0)$ values (determined at $q = 0.068$ Å^{-1}) from the respective SAXS curves. Dashed lines represent guides to the eye. c_p is 80 mg ml^{-1} (= 1.2 mM) for the BSA-YCl_3 and BSA-$LaCl_3$ systems and 85 mg ml^{-1} (= 1.3 mM) for the BSA-$HoCl_3$ system. Where not visible, the error bars are smaller than the symbols.*

The B_2/B_2^{HS} values of the BSA-$HoCl_3$ system are overall more negative than those of YCl_3 and differ in spite of the rather similar cationic radii of Y^{3+} and Ho^{3+}. Note that the reason for the absence of humps as they are observed in the case of the $1/I(0)$ data in the B_2/B_2^{HS} values is the fact that the density difference between the two phases only manifests itself in the $1/I(0)$ values. The B_2/B_2^{HS} values, however, are equal in coexisting dense and dilute phases (see e.g. Ref. 138), meaning that no density-dependent signature like the $1/I(0)$ hump is visible in the B_2/B_2^{HS} plot (Fig. 6.8).

The macroscopic phase behaviours observed here are linked to a combination of cation-induced interprotein interactions and cation-protein binding. To explore the cation binding behaviours to BSA and to explain potential differences between them, a comprehensive thermodynamic analysis using ζ potentials and isothermal titration calorimentry was performed. The results are summarised in the next section.

6.5.5 Thermodynamics of cation-protein binding: zeta potential and ITC measurements

In order to characterise the binding behaviour of cations to BSA, we measured BSA-salt sample series with increasing salt concentrations at different temperatures.

In Fig. 6.9 an exemplary temperature-dependent raw zeta potential data set of BSA in the presence of $HoCl_3$ system is shown. Corresponding data sets were also obtained for BSA in the presence of YCl_3 and $LaCl_3$. For further analysis, the data

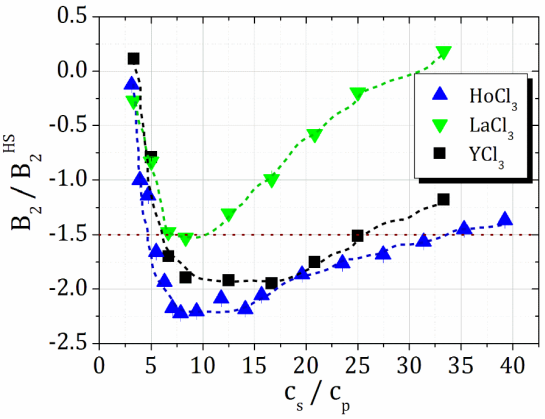

Figure 6.8: *2nd virial coefficients determined from sticky hard sphere potential fits to background-corrected SAXS data. Dashed lines represent guides to the eye. c_p is 80 mg ml^{-1} (1.2 mM) for the BSA-YCl_3 and BSA-$LaCl_3$ systems and 85 mg ml^{-1} (1.3 mM) for the BSA-$HoCl_3$ system. The dark-red dotted line indicates the critical B_2/B_2^{HS} value below which phase separation is expected to occur [138]. Where not visible, the error bars are smaller than the symbols.*

were fitted using the following equation (see ESI † [Section 6.9] for derivation):

$$Q = Q_0\left(1 + \frac{c(Q_0 - Q_1)(c_1 - c_0)}{c(c_0(Q_0 - Q_1) - c_1 Q_0) + c_0 c_1 Q_1}\right) \tag{6.8}$$

where Q_1 is the protein surface charge at the maximum salt concentration of $c_1 = 1\,\mathrm{mM}$, and c_0 is the salt concentration at the point of zero charge. The initial protein charge Q_0 without added salt was fixed to -9e, consistent with Ref. 13.

A first quantitative parameter obtained from the fit is c_0 as a function of temperature and type of salt. c_0 can be regarded as a measure for the cation-protein affinity. As can be seen from Fig. 6.10, c_0 decreases with temperature in every experimental system. This behaviour underlines the entropy-driven character of cation binding [13]. Moreover, a strong difference between the BSA-$HoCl_3$ system and the two other systems becomes obvious — overall, less Ho^{3+} cations are needed to neutralise the BSA charge, indicating a stronger binding affinity of Ho^{3+} to BSA.

The average number of cations binding to the protein surface, N, can be calculated via the relation $N = (Q_1 - Q_0)/3$ with $Q_0 = -9$ exploiting the fact that every cation has a charge of $+3$. The respective values are shown in Fig. 6.11. As can be seen in Fig. 6.11, the average number again shows the sequence $Ho^{3+} > Y^{3+} > La^{3+}$, with overall roughly 0.5–0.7 more cations bound for Ho^{3+} compared to La^{3+}. We remark that the exact choice for Q_0 is not essential for comparison between the cations, as the relative sequence in N is robust against variations of

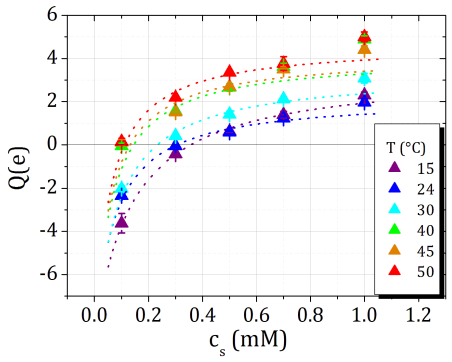

Figure 6.9: *Temperature-dependent ζ potential data of 1 mg/ml BSA with increasing $HoCl_3$ concentrations. Each data point is an average of five measurements, error bars represent the standard deviation. The grey line indicates the point of zero charge (c_0, $Q = 0$). The zeta potential values obtained were converted to elementary charge values using the calculations described in the SI. The dashed lines represent fits to the data (Eqn. 6.24.)*

Q_0.

In order to thermodynamically quantify cation-protein binding, isothermal titration calorimetry (ITC) measurements were performed, as shown in Fig. 6.12. While the profiles for $HoCl_3$ and YCl_3 appear to be very similar, the systems with $LaCl_3$ show a smaller enthalpic gain.

ΔH_{bind} was calculated by determining the integral of the curve until the respective molar ratios of zero charge (= 20.4 for $HoCl_3$, 29.1 for $LaCl_3$ and 30.9 for YCl_3) and divided by $Q_0/-\nu_s$ [13]. The obtained values read 10.6 kcal/mol for $HoCl_3$, 10.4 kcal/mol for YCl_3 and 7.8 kcal/mol for $LaCl_3$, reiterating the observation that $LaCl_3$ shows a smaller value, while $HoCl_3$ and YCl_3 appear similar. We note that due to batch-to-batch variations of BSA [220], potentially due to different content of co-ions remaining after the purification process, the absolute values of ΔH_{bind} should not be overinterpreted. Nevertheless, we argue that the values obtained here can be used for a semi-quantitative characterisation of our systems, in particular when comparing the cation-BSA binding for different cations within the same BSA batch.

6.6 Discussion

Based on the characterisation of cation-protein association and cation-induced protein interactions for different trivalent cations, we now discuss the implications for a general understanding which physicochemical parameters determine the interactions between proteins and multivalent cations.

Cation radii are obvious parameters that can be seen as influencing the overall protein–ion interactions. In the present study, this is most clearly reflected in the

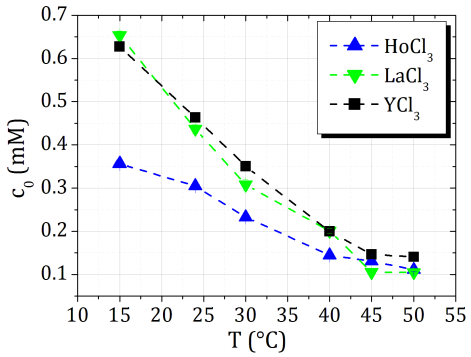

Figure 6.10: *c_0 values for the BSA-YCl_3, BSA-$LaCl_3$ and BSA-$HoCl_3$ systems (c_p = 1 mg/ml = 15 µM). The c_0 values were determined from fits (Eqn. 6.24) to the raw ζ potential data as shown exemplarily in Fig. 6.9. Dashed lines are guides to the eye.*

B_2/B_2^{HS} values where stronger attractions go along with smaller cation radii. Similar findings were obtained by Schomäcker et al [221] in a study showing a clearly linear dependence of human serum albumin and human blood serum affinity to Ln cations on cation radius. A publication by Smolka *et al.* [222] furthermore provides a detailed discussion of the role of the cation radius regarding the affinity of Ln cations to α-amylase, a system that is Ca^{2+}-dependent under physiological conditions. According to the authors, the smallest cation is likely to experience the strongest attraction to the protein due to the fact that its charge is concentrated near its binding site on the protein. In the case of a strong cation binding site, this effect can compensate the high hydration free energy of the cation, which leads to an increased protein-cation affinity with decreasing cationic radius [222].

While the relationship between cation radius and protein attraction strength appears straightforward in the case of the B_2/B_2^{HS} data, the c_0 calculations and ITC measurements indicate that the situation is more complex. This suggests that cation-protein binding energies (measured by ITC and zeta potentials) and cation-induced protein-protein bridging energies (measured by T_{trans} and B_2/B_2^{HS}) are not directly coupled. In particular, c_0, the salt concentration at the point of zero charge as a measure of cation-protein affinity, is rather similar for Y^{3+} and La^{3+}, while the c_0 values of Ho^{3+} differ strongly. In contrast, the B_2/B_2^{HS} values of Ho^{3+} and Y^{3+} resemble each other, whereas those of La^{3+} are clearly higher. In the case of ITC, the ΔH_{bind} values are comparable for Y^{3+} and Ho^{3+} whereas they are lower for La^{3+}, which indicates that no strong trends of cation-protein binding are seen in ITC. This may be caused by uncertainties of the experimental procedure and product purities. Since c_0 and B_2/B_2^{HS} measure cation-protein binding and cation-mediated protein-protein bridging, respectively, these findings appear to indicate that binding and bridging strengths can be different for the same cation.

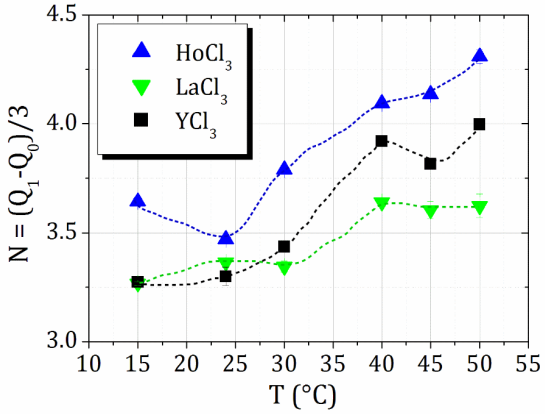

Figure 6.11: *Average number of cations, N, binding to BSA as calculated from ζ potential data as $(Q_1 - Q_0)/3$, Q_0 = -9. Dashes lines are guides to the eye.*

A probable explanation for this difference is the different surface geometry in the case of a cation being bound to one protein as opposed to when it is bridging two proteins. As the binding appears to be driven by entropy of hydration water [13], the dehydration due to the first bond to one protein molecule might be very different from that of the second bond to another protein. This explanation also emphasises that cation radii are not the only parameters that need to be taken into account in order to rationalise the influence of different cations on protein phase behaviour. This assumption is corroborated by a study conducted by Gomez *et al.* [223]. The authors investigated the abilities of lanthanide and Y^{3+} cations to restore the Ca^{2+}-dependent biological activity of trypsinogen — another protein known to bind Ca^{2+} as well as lanthanide and Y^{3+} cations at aspartic acid residues — after depleting their trypsinogen system of Ca^{2+}. At low lanthanide concentrations (around 10^{-4} M), the authors did not find a simple relationship between the cation radii and their efficiency in restoring the biological activity. Similarly, a non-monotonic relation between protein-lanthanide affinity and lanthanide radius has been found by Mulqueen *et al.* [224].

Gomez at al. [223] attribute their findings to potentially incomplete dehydration of different cations upon trypsinogen binding and to different amounts of water molecules bound to the protein-lanthanide complex. This aspect is very important to consider since our experimental system is known to be driven and strongly influenced by hydration effects [13, 89]. Gomez *et al.*[223] furthermore observe that Y^{3+} has a protein-cation affinity not fitting into the expected trend based on the cationic radii of the lanthanides. Along with findings indicating that the strengths of different Y^{3+}-ligand complexes vary strongly depending on the ligand chosen and can thus interfere with a straightforward integration of yttrium into trends of the lanthanide series [225, 226] this provides further evidence that parameters other than radius can play a role in the interactions between proteins

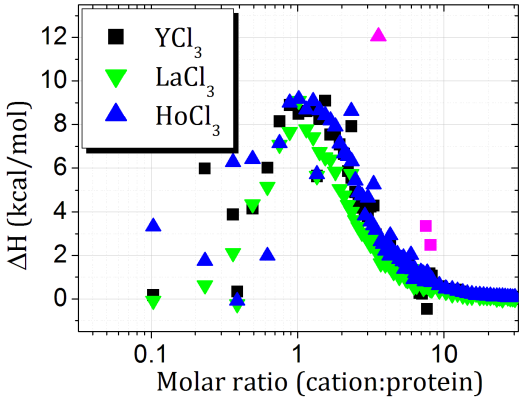

Figure 6.12: *ITC profiles of BSA titrated with YCl_3, $HoCl_3$ and $LaCl_3$. Magenta data points were considered outliers and therefore excluded from the analysis. The data sets were merged from measurements performed with 3 mM and 800 µM salt solutions.*

and multivalent cations. These can e.g. include electron configuration [184, 226] as well as cation polarisabilities and resulting dipoles [227].

Previous work on the thermodynamic properties of lanthanides [122] reports higher entropic contributions for the complexation of Ho^{3+} to ethylenediaminetetraacetic acid (EDTA). While a protein is certainly more complex than the rather simple EDTA molecule, coordination of lanthanide cations in the case of BSA nevertheless also proceeds via carboxylic groups, making EDTA-lanthanide complex formation a reasonable reference point. Our previous work [13] was strongly supported by earlier results obtained for lanthanide and Y cations binding to amino acids in solution [187, 188]. Together with the zeta potential results which indicate a higher number of cations bound for Ho^{3+}, this can help explain the stronger overall interprotein attraction induced by these cations.

The trypsinogen system investigated by Smolka *et al.* [222] which we mentioned earlier is known to have two cation binding sites, whereas our system features several (around four) sites with varying local geometry. In addition to this, the cations used in the present work do not simply bind to BSA, but also bridge protein molecules and lead to an overall more complex phase behaviour of our system[13, 95]. The aspects mentioned by Gomez *et al.* [223], especially cation and complex hydration, might thus have even more intricate effects on our systems. We suggest that these two aspects can thereby help explain the differences in BSA phase behaviour induced by different cations and the difference between Y^{3+} and Ho^{3+} in spite of the closeness of their cationic radii. This finding is consistent with the lower T_{trans} values in the presence of $HoCl_3$ as well as the larger LLPS areas obtained for BSA with $HoCl_3$.

From a broader perspective on biological matter, it is interesting to compare the protein system to the well-studied example of DNA: Analogously to the ob-

servations in our protein-cation systems, cation- [228] and polymer- [229] induced attraction between DNA strands can similarly stabilise and shift the melting temperature of DNA to higher values. An additional factor influencing the melting transition of DNA is its degree of hydration [230], which provides another conceptual link between phase transitions of DNA and proteins. The crucial aspect of hydration in our protein-cation systems will be discussed in more detail in the following.

Computational results on lanthanide cations in the absence of proteins confirm the importance of hydration effects and differences in cation hydration along the lanthanide series. Duvail *et al.* [116] performed an explicit polarisation molecular dynamics study on the exchange frequency (EF) of water molecules between the first hydration shell of lanthanide cations and bulk water. The EF shows a strongly non-monotonic behaviour along the lanthanide series with the maximum EF being observed for Tb^{3+}, a lanthanide cation located close to Ho in the periodic system. Additionally, the authors provide evidence for a change in both hydration water structure and coordination number along the lanthanide series, a result corroborating earlier findings by Habenschuss and Spedding [113–115] and studied in even more detail by Zhang *et al.* [118]. Persson *et al.* [119] furthermore identified Ho^{3+} as the cation with the strongest change in hydration structure.

As a general caveat, it should be kept in mind that simulations and calculations for lanthanides and their properties encounter difficulties due to non-negligible relativistic effects [118] caused by strong shielding of the nuclear charge [124], a generally large number of electrons and incomplete 4f electron orbital occupation [118]. Nevertheless, the above examples show that a large number of such studies exhibits good reproducibility and consistency. We assume that these findings can potentially help explain non-monotonous effects that we observe in our experimental systems and that cannot be explained only by cation radii.

When discussing the effects the cations studied here have on protein phase behaviour, the classification of Y with respect to the lanthanide series is an important aspect to be mentioned. As apparent from the study by Gomez *et al.* [223], this is not always straightforward. On the one hand, the chemical properties of Y are sufficiently close to the lanthanide series for it to be treated like a lanthanide [110]; on the other hand, extensive studies classifying lanthanide and Y complexes with various ligands show that depending on the ligand, Y can behave similarly either to the heavy or the light lanthanides [225, 226]. This is consistent with our own observations that points of zero charge or enthalpies of Y-BSA binding do not always follow a trend that could be expected based on cation radii or position in the periodic system. Our results confirm that while BSA phase behaviour induced by Y^{3+} cations is sufficiently similar to that induced by lanthanides, it cannot always be expected to follow similar trends.

6.7 Conclusions

The experiments presented here offer an insight into the differences in protein phase behaviours — in particular liquid-liquid phase separation (LLPS) — induced by the trivalent cations Y^{3+}, Ho^{3+} and La^{3+}. Whereas in the case of La^{3+} no phase separation is observed, Ho^{3+} leads to the formation of a dense phase which is potentially arrested. When Y^{3+} is used, the dense phase is more liquid-like. This difference in protein-protein attractions induced by the different cations is reflected in the increase and decrease of the transition temperature T_{trans} upon $LaCl_3$ and $HoCl_3$ addition to the BSA samples, respectively. In addition, the stronger interprotein attraction manifests itself in lower reduced second virial coefficient B_2/B_2^{HS} values as determined from SAXS experiments. The different cations used in this work can therefore tune thermal sensitivity of the samples. We emphasise that cation radius may not be the only parameter that should be considered when quantifying both cation-protein binding as well as cation-induced protein-protein interactions, and that hydration effects can be particularly important.

By carefully choosing multivalent cations, we are able to tune the phase transitions of aqueous BSA solutions. Our results thus provide a deeper understanding of thermodynamic fundamentals of colloidal and soft matter systems. Additionally, our findings are of relevance in the area of stimuli-responsive materials (e.g. for targeted drug delivery and release [231] or water pollutant clearance [232]) where tuning the sensitivity to different environmental factors is of pivotal importance.

Conflicts of interest

There are no conflicts of interest to declare.

6.8 Acknowledgements

The authors gratefully acknowledge financial support by the Deutsche Forschungsgemeinschaft (DFG) and thank the ESRF for beamtime on beamline ID02. O.M. acknowledges a PhD fellowship by the Studienstiftung des Deutschen Volkes (German Academic Scholarship Foundation) and thanks the PSCM (Grenoble), Thilo Stehle and Nina Jaspert (Tübingen) for sharing their laboratory resources as well as Pinelopi Christodoulou for help with the ITC measurements. F.R.-R. acknowledges funding from the Knut and Alice Wallenberg Foundation (project grant KAW 2014.0052). The authors are grateful to Theyencheri Narayanan (ESRF, Grenoble), Leonardo Chiappisi (ILL, Grenoble), Stefano Da Vela, Martin Oettel and Roland Roth (Tübingen) and Michael Dolg (Cologne) for valuable discussions.

6.9 Supporting Information

6.9.1 Calculation of effective protein surface charge, $Q(e)$, from ζ potentials

From the ζ potential data obtained from the measurements, the effective protein charge Q was calculated as follows.

First, the Debye screening length, κ^2 was calculated as [170]

$$\kappa^2 = 4\pi\lambda_B N_A \sum_i n_i Z_i^2 \tag{6.9}$$

with the Bjerrum length λ_B [27]

$$\lambda_B = \frac{e^2}{4\pi\epsilon_0\epsilon_{H_2O}k_BT} \tag{6.10}$$

with e being the elementary charge, ϵ_0 the vacuum dielectric permittivity and ϵ_{H_2O} the total dielectric permittivity of water at the respective temperature [233].

The Henry equation relates the electrophoretic mobility μ of a colloidal particle with a spherical shape, a radius a and a zeta potential ζ in a medium with a viscosity η *via* [172, 234]

$$\mu = \frac{2}{3}\frac{\epsilon_r\epsilon_0}{\eta}\zeta f(\kappa a) \tag{6.11}$$

Here, the Henry function $f(\kappa a)$ as given by Ohshima [172]

$$f(\kappa a) = 1 + \frac{1}{2}[1 + (\frac{2.5}{\kappa a[1 + 2\exp(-\kappa a)]})]^{-3} \tag{6.12}$$

is used to relate the electrophoretic mobility. The ζ potential is then calculated with the BSA radius a=3.3 nm. The default Zetasizer setting uses a Henry function $f(\kappa a) = 1.5$, which does not consider effects specific to the systems investigated here. Therefore, corrected ζ values ζ_{corr} are obtained by multiplying each ζ potential value by its corresponding $f(\kappa a)$ value. The ζ_{corr} values are furthermore rescaled by multiplying them by e/k_BT. The rescaled values are referred to as ζ^*.

The protein surface charge density, σ (C/m^2), is given by [171]

$$\sigma = \frac{\epsilon_0\epsilon_r\kappa k_BT}{e}(2\sinh(\zeta^*/2) + (4/(\kappa a)\tanh(\zeta^*/4))) \tag{6.13}$$

Finally, the surface charge Q of BSA under the respective sample conditions given by salt concentration and temperature are calculated as

$$Q = 4\pi a^2\sigma \tag{6.14}$$

6.9.2 Fitting model for $Q(e)$ as a function of temperature and salt concentration

We begin with a standard Langmuir-like equation describing the binding of cations to the protein surface:

$$Q = Q_0 + \frac{N\nu c}{c + K} \tag{6.15}$$

which can be converted into its alternative form

$$N\nu c + K(Q_0 - Q) + c(Q_0 - Q) = 0 \tag{6.16}$$

Here, Q_0 is the initial protein surface charge in the absence of salt, N is the number of binding sites, ν the valence of the salt (here, it is always +3), K the binding constant and c the salt concentration.

Next, we define the point of zero charge:

$$Q(c_0) = 0 \tag{6.17}$$

and the charge at $c_s = c_1 = 1\ mM$ (plateau value) as

$$Q(c_1) = Q_1 \tag{6.18}$$

Substituting expressions 6.17 and 6.18 into Eqn. 6.16, we obtain a system of linear equations:

$$N\nu c_0 + KQ_0 + cQ_0 = 0 \tag{6.19}$$

$$N\nu c_1 + K(Q_0 - Q_1) + c_1(Q_0 - Q_1) = 0 \tag{6.20}$$

which allows us to express N and K from Eqn. (6.15) as

$$\begin{pmatrix} \nu c_0 & Q_0 \\ \nu c_1 & Q_0 - Q_1 \end{pmatrix} \begin{pmatrix} N \\ K \end{pmatrix} = \begin{pmatrix} -c_0 Q_0 \\ -c_1(Q_0 - Q_1) \end{pmatrix} \tag{6.21}$$

Solving this system of equations yields the following expressions for K and N:

$$N = \frac{1}{\nu} \frac{Q_0(Q_0 - Q_1)(c_1 - c_0)}{c_0(Q_0 - Q_1) - c_1 Q_0} \tag{6.22}$$

$$K = \frac{c_0 c_1 Q_1}{c_0(Q_0 - Q_1) - c_1 Q_0} \tag{6.23}$$

and, finally, the equation used to fit the temperature- and salt concentration-dependent Q values:

$$Q = Q_0\Big(1 + \frac{c(Q_0 - Q_1)(c_1 - c_0)}{c(c_0(Q_0 - Q_1) - c_1 Q_0) + c_0 c_1 Q_1}\Big) \tag{6.24}$$

Chapter 7

Phase-Separation Kinetics in Protein-Salt Mixtures with Compositionally Tuned Interactions

7.1 Abstract

Liquid-liquid phase separation (LLPS) in protein systems is relevant for many phenomena, from protein condensation diseases to subcellular organization to possible pathways toward protein crystallization. Understanding and controlling LLPS in proteins is therefore highly relevant for various areas of (biological) soft matter research. Solutions of the protein bovine serum albumin (BSA) have been shown to have a lower critical solution temperature-LLPS (LCST-LLPS) inducible by multivalent salts. Importantly, the nature of the multivalent cation used influences the LCST-LLPS in such systems. Here, we present a systematic ultrasmall-angle X-ray scattering (USAXS) investigation of the kinetics of LCST-LLPS of BSA in the presence of different mixtures of $HoCl_3$ and $LaCl_3$, resulting in different effective interprotein attraction strengths. We monitor the characteristic length scales $\xi(t, T_{fin})$ after inducing LLPS by subjecting the respective systems to temperature jumps into their liquid-liquid coexistence regions. With increasing interprotein attraction and increasing T_{fin}, we observe an increasing deviation from the growth law of $\xi \sim t^{1/3}$ and an increased trend toward arrest. We thus establish a multidimensional method to tune phase transitions in our systems. Our findings help shed light on general questions regarding LLPS and the tunability of its kinetics in both proteins and colloidal systems.

7.2 Introduction

Liquid-liquid phase separation (LLPS) is known to occur in a variety of systems from mixtures of organic molecules to colloidal matter with, in many cases, complex interaction potentials. When occuring in protein systems, metastable LLPS plays an important role in cellular organization, signaling and development [18–21, 236]. Furthermore, LLPS is related to the main reason behind protein condensation diseases such as cataract [17] and sickle cell anemia [237] and can influence the properties of protein-based therapeutics [3, 15, 238]. In addition, several properties of industrial food products are similarly governed by phase separation phenomena [22, 23]. Importantly, the density inhomogeneity associated with LLPS can be an important precursor for protein crystallization [82, 176, 239]. Understanding and rationally manipulating LLPS in protein solutions is thus of strong interest for several areas of biological and soft matter research.
The two main mechanisms leading to liquid-liquid phase separation are nucleation and spinodal decomposition (SD), respectively, taking place in the metastable and unstable regions of the area inside the binodal of the phase diagram of the system in question. Nucleation is often described via classical nucleation theory (CNT) (see, e.g., ref 46), whereas SD is commonly rationalized using Cahn-Hilliard theory relating the temporal variation of concentration fluctuations $\frac{\partial \delta c(r,t)}{\partial t}$ to the changes in the free energy F of the system [42, 46, 240, 241]. In the late stages of SD, coarsening according to Lifshitz and Slyozov [46, 71, 242] and Binder and Stauffer [243] predicts a time-dependent growth of the characteristic length ξ of the respective system according to the power law $\xi \sim t^{1/3}$.
LLPS, SD and their interplays with phenomena such as arrested phase transitions have been studied both theoretically and experimentally in a variety of systems such as metal alloys [244, 245] and polymer blends [246, 247] as well as colloidal systems (see, e.g., refs 248–253 and 254 for a review).

It was found experimentally and established theoretically [31–33, 49, 50] that a metastable LLPS in colloidal systems can be traced back to short-ranged (i.e., much smaller than the particle diameter [49]) attractions between the colloids. Importantly, this concept established in colloid science is, within certain approximations and limits, applicable to many protein systems since the latter typically also exhibit short-ranged interparticle attraction [55]. Under certain conditions, protein systems can also undergo a metastable LLPS [56–58, 60, 63, 65, 255–259] which can be described and rationalized using concepts from colloid theory.

For example, Shah et al. [256] observed a continuous transition from metastable to unstable phase separation mechanisms in aqueous lysozyme solutions with an upper critical solution temperature (UCST) for varying temperature quench depths. A further experimental study on lysozyme by Cardinaux et al. [65] reported that the quench depth into the coexisting region determines whether the system undergoes complete LLPS or whether glass formation interferes with the latter. These results were later confirmed by Gibaud et al. [258] who showed that the arrested two-phase system obtained by Cardinaux et al. [65] consisted of a

bicontinuous network in an arrested state. The work by Gibaud et al. [258] also clearly illustrates the change of the growth exponent α of $\xi \sim t^{\alpha}$ with increasing time. Although α is equal to 1/3 in the initial stages of growth, there is a substantial slowing down in the late stages of the experiment, i.e., for large t. The network obtained for deep quenches is the result of an arresting spinodal decomposition in the early stages of critical quenches.

Throughout the past years, our group has established a model system of proteins in aqueous solutions with a short-range interprotein attraction induced by multivalent cations [8–14, 82–90]. Among other phenomena, this short-range attraction leads to a metastable LLPS [10, 12] which can play an active role in the nucleation and growth of protein crystals [10, 11, 82, 86, 87]. The short-range interprotein attraction induced by multivalent cations has been rationalized by a cation-activated patchy particle model [95, 260]. Binding patches on the surface of proteins are known not only for ions but also for more complex ligands such as pharmaceuticals [261]. Notably, the LLPS in our systems is entropically driven and appears as temperature increases, i.e., it features a lower critical solution temperature (LCST-LLPS) [13, 14, 89]. A recent study reported that the type of multivalent cation used has a strong influence on the phase behavior on the LCST-LLPS of BSA [201]. We established that using $HoCl_3$ induces strong a interprotein attraction whereas the attraction is relatively weak in the case of $LaCl_3$. Importantly, phase transitions of BSA can be fine-tuned by using different ratios of weakly and strongly interacting multivalent salts at constant ionic strength [201], as notably manifested in shifts of the transition temperatures of phase-separating samples.
Having established the equilibrium phase diagrams of systems consisting of BSA and multivalent cations, here we study the kinetics of LLPS of BSA in the presence of multivalent salts *via* ultrasmall-angle X-ray scattering (USAXS), an experimental approach recently demonstrated in refs 14 and 262.

In particular, the present study focuses on the intriguing possibility of rationally manipulating the kinetics of phase separation in BSA-multivalent salt systems by changing their salt composition. Importantly, the control of the phase behavior of soft matter systems such as protein solutions opens up pathways toward controlled induction and tuning of different system properties such as phase separation and associated density fluctuations. The latter have been shown to facilitate the growth of protein crystals [176], which has crucial implications for crystallography and structural biology. In addition, the manipulation of stimulus-responsive systems is of fundamental interest for the design of the so-called smart materials [232] or drug delivery systems [231]. Establishing the role different factors play in controlling the phase behavior of soft matter is therefore of fundamental importance in a variety of research areas. In the systems described in the present study, we use different ratios of the two multivalent salts $HoCl_3$ and $LaCl_3$ introducing strong and relatively weak interprotein attractions, respectively, to rationally tune the phase behavior of our systems. We find that with increasing $HoCl_3$ concentration, i.e., increasingly attractive protein interactions, the deviation from the $\xi \sim t^{1/3}$

growth law becomes pronounced and allows the experimental systems to enter an arrested state even in the case of small temperature jumps.
Exploiting the dependence our systems have on both the type of multivalent cation used and on temperature, we thus establish a framework suitable for a multidimensional control of phase transitions of experimental systems. Our results are of general interest to areas of science concerned with fundamental research on phase separation thermodynamics and their mechanisms in colloids and proteins, and how these are affected by changes in microscopic interactions.

7.3 Experimental Methods

7.3.1 Determination of Coexistence Regions of BSA-$HoCl_3$/$LaCl_3$ Mixtures

Binodals reflecting the liquid-liquid coexistence regions of all samples were determined as follows. Samples containing initial protein concentrations of 175 mg/mL BSA and a total salt concentration of 40 mM consisting of $HoCl_3$ and $LaCl_3$ with the ratios 22/18, 25/15 and 30/10 mM were prepared in a water bath at temperatures from 12 to 45 °C by mixing appropriate amounts of protein and salt stock solutions. The samples were left to equilibrate for 20 min and subsequently centrifuged for 2 min at 21000 rcf (Mikro 220R centrifuge, Hettich, Tuttlingen, Germany) at preparation temperature to facilitate separation into dense and dilute phases. The samples were equilibrated for 15 more minutes in the water bath at preparation temperature again, after which the volumes of both dense and dilute phases were determined by pipetting. The BSA concentrations of the dilute phases were measured by UV absorbance at $\lambda = 280$ nm [1]. The concentrations of the corresponding dense phases were calculated based on mass conservation.

7.3.2 USAXS Sample Preparation

BSA (catalogue number A7906, heat shock fraction) with a purity of $\geq 98\%$ as well as $HoCl_3$ (catalogue number 450901) and $LaCl_3$ (449830) (the respective purities were indicated as 99.9-99.99%) were purchased from Sigma Aldrich (now Merck, Darmstadt, Germany) and used as received. Protein and salt stock solutions were prepared by dissolving appropriate amounts of respective chemicals in degassed ultrapure (18.2 MΩ) MilliQ water (Merck Millipore, Darmstadt, Germany). The protein concentration of the stock solution was then determined by UV absorbance at $\lambda = 280$ nm [1].
Samples containing initial concentrations of 175 mg/mL BSA and different $HoCl_3$/-$LaCl_3$ ratios were prepared by mixing appropriate amounts of protein and salt stock solutions at room temperature (21 °C). The samples were centrifuged for 2 min at 21000 rcf to facilitate the macroscopic separation of the dense and dilute phases. The samples were then stored at 21 °C overnight, after which the dilute

phases were removed. The dense phases were stored at 5 °C for several hours until they became clear and were subsequently filled into quartz capillaries with a diameter of 1 mm using a syringe (Norm-Ject, Henke-Sass Wolf GmbH, Tuttlingen, Germany). Prolonged centrifugation at low speed and at 5 °C was then applied to remove air bubbles from the capillaries.

7.3.3 USAXS Measurements

The USAXS measurements were performed at beamline ID02 [160, 161] (ESRF, Grenoble, France) using the 30 m sample detector distance setup. A $q = \frac{4\pi sin\theta}{\lambda}$ range from $1.1 \cdot 10^{-3}$ to $7.2 \cdot 10^{-2}$ nm^{-1} was covered. The wavelength λ used was 0.995 Å, corresponding to an energy of 12.46 keV. The signal was recorded using a FReLoN Kodak CCD detector.
Every measurement was performed by subjecting the respective sample to a temperature jump to a final temperature T_{fin} between 30 and 50 °C using a heating rate of 80 K/min. The starting temperature was 10 °C. Throughout the experiment, the temperature was controlled using a temperature stage (Linkam Scientific Instruments, Surrey, U.K.). The USAXS measurements were divided into three distinct steps covering different stages of phase separation at the respective T_{fin}. In steps 1, 2, and 3, exposures were taken every 0.7 s, every 4 s and every 30 s, respectively, as described in detail in ref 14. At every step, the X-ray beam was focussed onto a different spot of the capillary to minimize radiation effects [14]. We note that the temperature jumps (i.e., heating) we use for our LCST systems correspond to the temperatures quenches (i.e., cooling) commonly described for colloidal and protein systems with a UCST (see, e.g., refs 65 and 258).

Prior to data analysis, the first featureless curve of each data set obtained at 10 °C before the temperature jump was subtracted from the following curves. The q value corresponding to the maximum intensity (q_{max}) was determined for each spectrum, and the characteristic length scale ξ was calculated as $\xi = 2\pi/q_{max}$.

7.3.4 Very Small-angle Neutron Scattering (VSANS) Measurements

VSANS measurements were performed at beamline KWS-3 (FRM-II, Garching, Germany) [163]. A $q = \frac{4\pi sin\theta}{\lambda}$ range from $1.2 \cdot 10^{-5}$ to $1.1 \cdot 10^{-3}$ $Å^{-1}$ was covered. Samples with composition and preparation identical to those that used for USAXS measurements were filled into quartz cuvettes (type 404-QX, Hellma Optics, Jena, Germany) with a thickness of 1 mm and a total volume of 0.7 mL on ice and centrifuged extensively at 4 °C at very low speed (max. 20 g) to remove air bubbles. Prior to the measurement, the samples were kept on ice. To start the measurement, the samples were then placed onto a sample holder preheated to the desired T_{fin} via a circulating water bath (Julabo, Seelbach, Germany). VSANS

profiles were recorded at intervals of 5-10 min at the respective T_{fin} for a total time of up to 2 h. Background correction was performed by subtracting the scattering profile of an empty sample cell. The correlation length ξ was calculated as $2\pi/q_{max}$.

7.4 Results and Discussion

7.4.1 Binodals of BSA-$HoCl_3$/$LaCl_3$ systems

To understand the influence different $HoCl_3$/$LaCl_3$ ratios have on the coexistence regions of the respective samples, the binodals of the samples with an initial BSA concentration of 175 mg/mL and varying initial salt ratios were measured by UV-vis spectroscopy. The binodals are displayed in Figure 7.1.

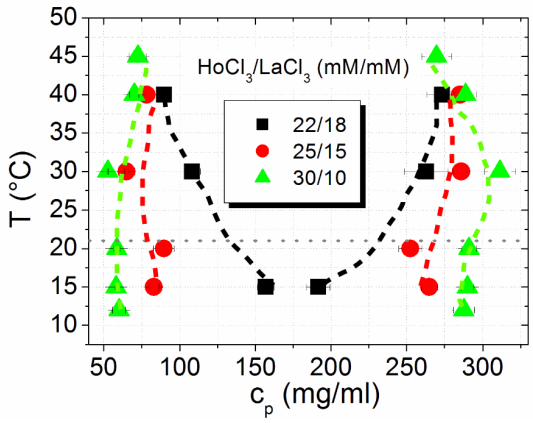

Figure 7.1: *Binodals of corresponding dense and dilute phases obtained after LCST-LLPS of samples with $c_{p,initial}$ = 175 mg/mL and varying initial salt ratios as shown in the legend. Dashed lines are guides to the eye. The gray dotted line indicates the preparation temperature of the samples. The samples used for the USAXS experiments described later on are located on the dense branches of the respective coexistences curves.*

The binodals show a clear trend toward a higher difference in protein concentration (c_p) between dense and dilute phases with increasing $HoCl_3$ concentration as indicated by the broadening of the coexistence regions with an increasing $HoCl_3$/$LaCl_3$ ratio. The samples used for the USAXS measurements (whose analysis is described below) are located on the dense branch of the binodal. As seen in Figure 7.1, their protein concentrations (volume fractions) increase with increasing $HoCl_3$ concentration. The differences in phase behavior of the systems under investigation are therefore traced back to the salt composition itself, as well as to the salt composition-induced differences in their respective protein concentrations. This is discussed in more detail below.

In addition, the only sample composition in which an experimental approach toward the lower critical point above 0 °C is possible is the one with the lowest $HoCl_3$ concentration. A stronger overall interprotein attraction brought about by higher $HoCl_3$ concentrations presumably shifts the critical point toward lower temperatures which cannot be reached within the temperature window accessible experimentally (i.e., above 0 °C). This is consistent with cloud temperature data [201] where high $HoCl_3$ concentrations led to phase separation below the temperature window experimentally accessible.

7.4.2 Obtaining $\xi(t, T_{fin})$ from USAXS Profiles

A typical USAXS $I(q)$ plot obtained using a dense phase of an initial BSA concentration of 175 mg/mL and a $HoCl_3/LaCl_3$ ratio of 25/15 (T_{fin} = 45 °C) is shown in Figure 7.2.

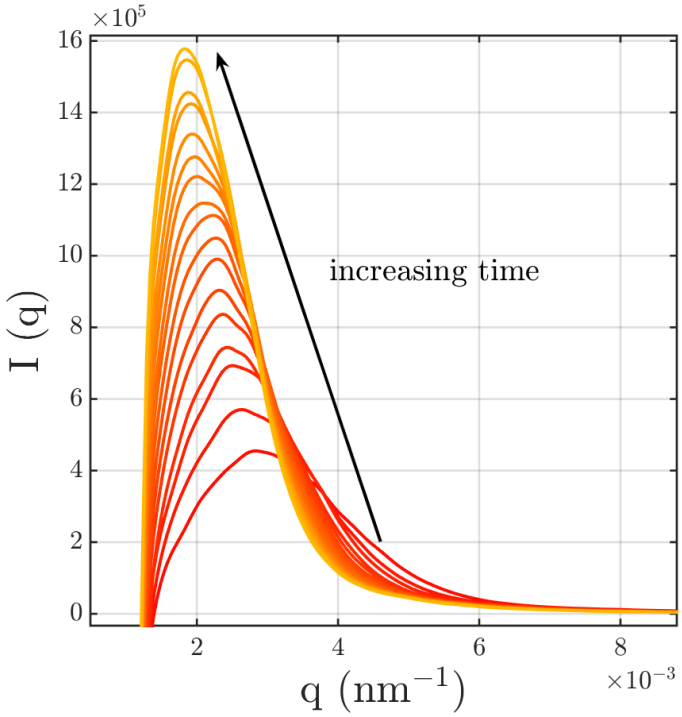

Figure 7.2: *Typical raw USAXS data (initial BSA concentration = 175 mg/mL, $HoCl_3/LaCl_3$ ratio = 25/15, T_{fin} = 45 °C. Data were smoothed by binning every 5 points. The first curve corresponds to t = 60 s after the T jump, the last to t = 510 s. The characteristic length scale of the respective systems was calculated as $\xi = 2\pi/q_{max}$. The curves shown here were taken in time intervals of 30 s. See text for details.*

From the raw USAXS data, $\xi = 2\pi/q_{max}$ values were extracted and plotted as functions of time. Data sets of $\xi(t, T_{fin})$ for each sample composition and at different jumps to T_{fin} are shown in Figure 7.3.

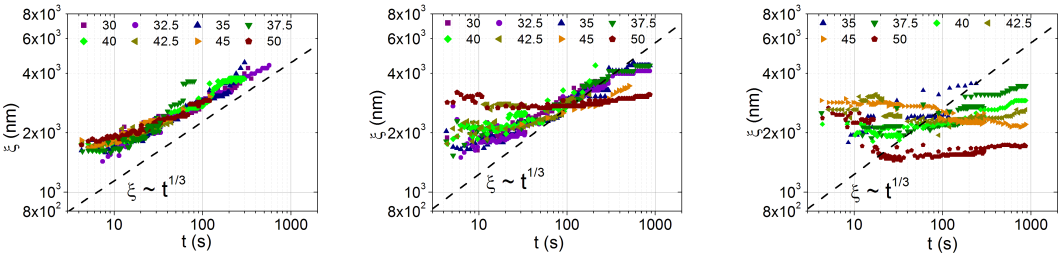

Figure 7.3: *$\xi(t, T_{fin})$ profiles of different $HoCl_3/LaCl_3$ mixing ratios. The legends indicate T_{fin} (°C). We note that for long observation times t, $\xi(t, T_{fin})$ reaches a plateau as confirmed by very small-angle neutron scattering data (see the Supporting Information.)*

In the case of the lowest $HoCl_3$ concentration (Figure 7.3 a), $\xi(t, T)$ follows the power law growth of $\xi \sim t^{1/3}$ to a good approximation for all T_{fin}. Interestingly, the power law and its temperature dependence can be strongly influenced by different $HoCl_3/LaCl_3$ ratios as becomes apparent from a comparison of Figure 7.3 a-c. With increasing T_{fin} and $HoCl_3$ concentration, the growth of $\xi(t, T_{fin})$ slows down, potentially approaching an apparently arrested state or strongly delayed kinetics of transformation at the highest T_{fin} and the highest concentrations of $HoCl_3$.

A possible scenario to rationalize the slowdown observed in the growth of ξ with increasing $HoCl_3$ concentrations would be as follows. First, a higher $HoCl_3/LaCl_3$ ratio widens the BSA-$HoCl_3/LaCl_3$ binodal and therefore influences the volume fraction of the USAXS samples that are located on the dense branch of the binodal (cf. Figure 7.1). In addition, multivalent salt has been shown to partition preferentially into the dense coexisting phase upon LLPS [10]. Moreover, the affinity of Ho^{3+} cations to BSA appears to be higher than that of La^{3+} cations [201]. Finally, Ho^{3+} cations induce a stronger interprotein attraction than La^{3+} cations [201]. It is therefore reasonable to assume that our samples are enriched with Ho^{3+}, which enhances the interprotein attraction. Thus, it seems likely that the combination of a higher protein volume fraction (which is more prone to arrest) and a stronger protein-protein attraction gives rise to the observed stronger tendency for arrest in the samples with more $HoCl_3$ and therefore deviates from the $\xi \sim t^{1/3}$ behavior.

We note that for systems with the highest $HoCl_3$ concentrations and the highest T_{fin}, the corresponding intensities $I(q_{max})$ feature a nonmonotonous behavior. In the present publication, however, we focus on the behavior of $\xi(t, T_{fin})$ and do not intend to analyze the behavior of the intensity. We note that while some of the samples appear kinetically hindered in some form for long observation times, we cannot rule out that under certain conditions, a slight coarsening of the structure might still occur for substantially longer times. Furthermore, we note that $\xi(t, T_{fin})$ saturates for very long time scales, as expected and as independently

confirmed using very small-angle neutron scattering (VSANS) [163, 262] (see the Supporting Information).

Interestingly, the plateau value of $\xi(t, T_{fin})$ in the samples containing the highest $HoCl_3/LaCl_3$ ratio shows a lower $\xi(t, T_{fin})$ for higher T_{fin} (Figure 7.4). This observation aligns well with a study conducted by Gibaud et al. [258] on a lysozyme system with an upper critical solution temperature. Gibaud et al. trace back their findings to the fact that arrest occurs in the early stage of spinodal decomposition. Given this explanation and our observation that, in the samples with the highest $HoCl_3$ concentration, ξ does not grow with time (Figure 7.3 c), we therefore tentatively assume that in this sample arrest can indeed occur at an early stage of phase separation. In addition, the data shown in Figure 7.4 indicate that even in the arrested state approached at long times for all temperatures in the samples with the highest $HoCl_3/LaCl_3$ ratio, $\xi(t, T_{fin})$ is still tunable by choosing different T_{fin}, which is of potential interest for the fabrication of protein-based materials with temperature-responsive structures.

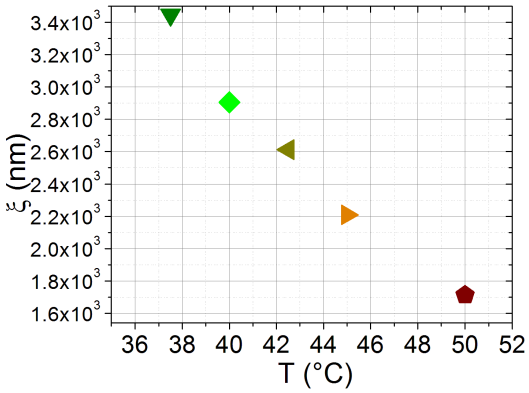

Figure 7.4: *$\xi(t, T_{fin})$ at long times ($t \approx 870$ s) obtained from the late-stage data of the samples with the highest $HoCl_3/LaCl_3$ ratio (cf. Figure 7.3 c).*

Considering that both Ho^{3+} and La^{3+} used here are trivalent and part of the lanthanide series, it is remarkable how strong the differences in the kinetics are, induced by only a small change in their relative initial concentrations. Thus, even small changes in the composition of the samples lead to substantial changes in the phase transition kinetics. This is qualitatively consistent with the observation of strong differences in the phase transition temperatures of BSA (cf. Figure 7.1 and ref 201) upon small changes of the multivalent salt ratios. In the experiments described in ref 201, it was found that Ho^{3+} cations have the strongest affinity to BSA and also induce the strongest BSA-BSA interactions. La^{3+} cations are the weakest agents in both respects. In addition, protein-protein interactions were found to be fine-tunable by varying cation mixture ratios. These results underline the importance and strength of ion-specific effects also for trivalent ions, similar

to the famous Hofmeister series (established mostly for monovalent ions) [263].

By controlling the protein-protein interactions of our systems, we are able to tune the effective depth of the temperature jump [65, 256] into the coexisting regions of our samples by varying the ratio of a salt inducing strong and weak protein-protein interactions ($HoCl_3$ and $LaCl_3$, respectively).

Moreover, we are able to influence the onset of arrested states via both strength of the cation-induced protein-protein interaction and temperature. This manifests itself in the increasing deviation from the power law growth of $\xi \sim t^{1/3}$ with increasingly attractive overall interactions. This observation can potentially be explained *via* the formation of clusters *via* cation-induced protein bridging [95]. The fact that arrest occurs at high T_{fin} and at high $HoCl_3$ concentrations can also be tentatively attributed to the fact that the high protein concentration and the strong interprotein attraction induced by Ho^{3+} cations [201] can lead to the formation of an attractive glass [254]. Importantly, the present study shows how subtle differences in sample composition, brought about by different salt ratios, can lead to large macroscopic differences in sample behavior and, intriguingly, allow for tuning of the phase behavior in a rational way.

7.5 Conclusions

We have established that the growth of the characteristic length scale $\xi(t, T_{fin})$ of our systems consisting of BSA with different mixing ratios of trivalent salts slows down with increasing temperature and increasing concentrations of the salt $HoCl_3$ inducing strongly attractive interactions up to the point that the system appears to be in a locked-in or arrested state. Intriguingly, we are able to influence the onset of arrested states by varying the ratios of different multivalent salts. We note that the specific behavior and the specific differences of (multi)valent ions and in particular their mixtures and interactions with proteins appears to not lend itself to simple explanation. In particular, effects of inhomogeneous cation distribution and their different affinities to proteins [201, 221–223] can play a role. Considering that the Hofmeister series for the seemingly simple monovalent ions was established more than 100 years ago, but is still in need of investigation, it is probably not surprising that for the more complex lanthanides a simple explanation appears elusive at present. Nevertheless, the data presented in this publication demonstrate that we can combine two control parameters — temperature and ratio of multivalent salts introducing strong and weak interprotein attraction — to obtain multidimensional control of the phase behavior of the system.

With this paper we hope to have provided new and interesting data on cation-induced liquid-liquid phase separation and its kinetics in proteins and to stimulate further theoretical work on these highly complex systems. Our results open new opportunities to tune phase transitions not only in proteins, but also in colloidal or polymer systems sensitive to external stimuli such as temperature or ionic strength. This is of particular interest for the design and development of smart

materials such as gels used to purify water [232].

7.6 Acknowledgement

The authors gratefully acknowledge the ESRF for beamtime allocation on beamline ID02 and thank the DFG for financial support. O.M. acknowledges a PhD fellowship by the Studienstiftung des Deutschen Volkes and thanks the PSCM (Grenoble) for sharing their laboratory resources as well as A. Girelli and C. Beck for assistance during the USAXS measurements. Helpful discussions with T. Narayanan (ESRF, Grenoble) and R. Roth (Tübingen) are gratefully acknowledged.

7.7 Supporting Information

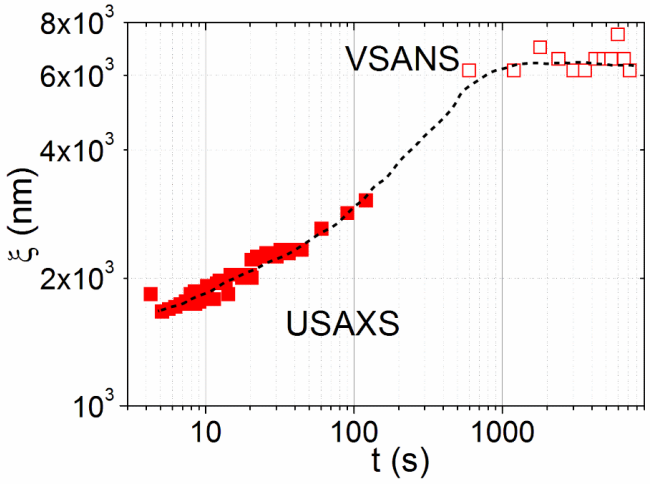

Figure 7.5: *$\xi(t)$ for the sample containing an initial $HoCl_3/LaCl_3$ ratio of 22/18. $T_{fin} = 45\,^{\circ}C$. The combined USAXS [160, 161]/VSANS [163] data set shown here indicates that at times beyond about 1000 s, ξ saturates. The dashed line is a guide to the eye.*

Chapter 8

Protein condensation in the presence of lanthanide metal ions: relating local structure at the metal centres to phase behaviour

This chapter is based on Ref. 264.

8.1 Abstract

Liquid-liquid phase separation (LLPS) of protein solutions plays an important role in protein condensation diseases, cell signalling and protein crystallisation. A thorough investigation of the mechanisms behind LLPS is therefore crucial. Multivalent salts such as YCl_3 have been shown to induce a hydration entropy-driven LLPS with a lower critical solution temperature (LCST-LLPS) in aqueous solutions of negatively charged proteins such as bovine serum albumin (BSA), providing an intriguing experimental framework for a comprehensive study of LLPS in proteins. Here, the mechanism of LCST-LLPS in these systems is investigated on a molecular level by probing the local chemical environment of the Y^{3+} cations using extended X-ray absorption fine-structure (EXAFS) spectroscopy. The EXAFS profiles presented show that the Y^{3+} coordination number (CN) decreases with increasing protein concentration and temperature. The decrease of the CN is due to the partial substitution of hydration water molecules around the Y^{3+} cations by protein carboxyl groups upon Y^{3+} coordination by the protein. The results of this study thus provide molecular-level evidence that the release of hydration water molecules around cations upon protein-cation binding and cation-mediated protein-protein bridging represents an important contribution to the hydration entropy-driven LCST-LLPS.

8.2 Introduction

The interactions of biological macromolecules, in particular proteins, in aqueous solutions are highly complex and depend on a number of environmental parameters

including the concentrations of the macromolecules themselves and of co-solute ions, pH, pressure, and temperature. In contrast to DNA or conventional colloidal systems, patches of both positive and negative charges can coexist on the surfaces of proteins. Moreover, globular proteins also exhibit more irregular geometries and anisotropy compared to DNA and conventional colloids, implying that complex and heterogeneous charge patterns prevail. Together with other interactions, such as hydrophobic and hydration effects, these factors make the phase behavior of protein solutions very difficult to predict or model [265], especially in the absence of incisive structural information that can be used to confront and/or validate model predictions.

In spite of these challenges, protein systems can nevertheless exhibit common properties. As an example, the phase diagrams of several proteins have been shown to feature liquid-liquid phase separation (LLPS) into a protein-poor (dilute) and a protein-rich (dense) phase [10, 57–60, 63, 64]. Importantly, LLPS can precede and/or enhance the growth of protein crystals [10, 58, 60, 82, 176, 266], providing an intriguing possibility to rationally manipulate pathways towards obtaining diffraction-quality crystals for structural analysis [82, 85, 87]. In addition to its important role in protein crystallisation, LLPS is also known to influence signalling pathways and intracellular communication of living cells [18–21], affect the stability of protein-based pharmaceuticals [3, 15] and cause protein condensation diseases such as eye cataract or sickle cell anemia [17, 64, 133, 267]. A detailed mechanistic understanding of LLPS in protein solutions is thus of utmost importance for many research areas and calls for both computational and experimental approaches to this topic.

Several theoretical studies [30, 31, 33, 49, 50] suggest that short-range attractions can lead to a metastable LLPS in colloidal systems. Importantly, this concept can also be used to rationalise LLPS in protein systems [57, 65, 258]. Thus, a common approach to actively induce LLPS of protein solutions for the sake of experimental investigations thereof is the addition of nonadsorbing depleting species such as polymers [64, 268, 269] which introduce the desired short-range interprotein attraction.

Alternatively, the latter can be induced by multivalent cations. Throughout the past years, we have therefore studied the effect of ion charges, introduced via di- and trivalent metal cations, on the phase behavior of aqueous solutions of negatively charged globular proteins [8–10, 12–14, 82, 83, 86–90, 269, 270]. Our studies confirm that the cations directly interact with the protein surface and, under certain circumstances, can bridge neighbouring protein molecules. This phenomenon has been rationalised *via* a patchy particle model [96, 260] based on Wertheim theory, combining a hard sphere repulsion and a short-range attraction term [95]. The cation-induced protein-protein interactions can lead to a rich phase behaviour, including re-entrant condensation [8, 9], protein crystallisation [82, 86–88, 266, 270] and, importantly, metastable LLPS [10, 12] (see Fig. 8.1).

Fig. 8.1 illustrates the phase behaviour of BSA in the presence of a multivalent salt such as YCl_3. At low salt concentrations c_s (Regime I), only few cations

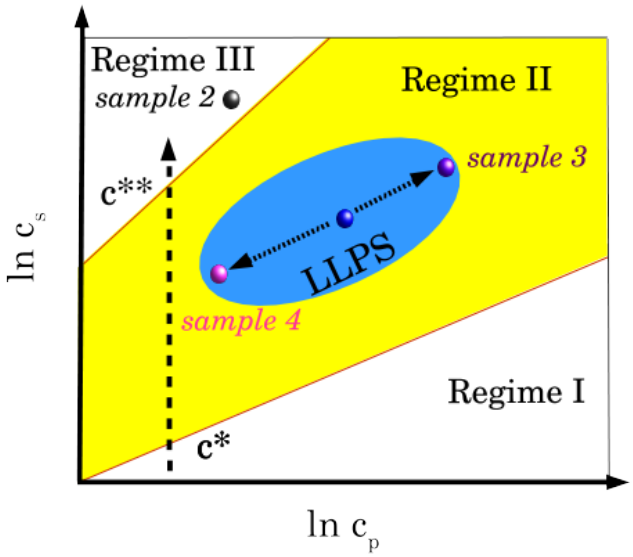

Figure 8.1: *Generic phase diagram of BSA in the presence of a lanthanide chloride. Reentrant condensation and LLPS are shown. Axis labels represent the logarithmic protein (ln c_p) and salt concentrations (ln c_s). The dashed arrow illustrates a change in phase behaviour with increasing c_s. The samples measured in this study (Table 8.1) are indicated by the grey sphere symbols. Samples 1 and 5 (not indicated here) are the reference without BSA and a thermally denatured sample, respectively (Table 8.1). Details on the phase diagram are given in Refs. 8–10, 12, 95 and in the text.*

bind to BSA, the net protein charge is negative, the overall attraction is repulsive and the solution appears clear upon visual inspection. Upon increasing c_s (dashed arrow), cations bind to and bridge BSA molecules, introducing a short-range attraction between the protein molecules and rendering the solution turbid due to protein clustering. This region of the phase diagram is referred to as Regime II. For samples located inside the area indicated by the blue ellipsoid, metastable liquid-liquid phase separation (LLPS) into a dilute (protein-poor, pink sphere) and a dense (protein-rich, purple sphere) phase can occur. At even higher c_s, the overall charge of the protein is inverted due to a high amount of multivalent cations binding to its surface; the overall interaction of the system becomes repulsive again [8–10, 12, 95].

Importantly, the metastable LLPS indicated in Fig. 8.1 has been shown to feature a hydration entropy-driven lower critical solution temperature (LCST) phase behaviour in systems of bovine serum albumin (BSA) and various multivalent salts [13, 89, 201]. We propose that a partial release of hydration water molecules around multivalent cations plays a decisive role in the entropic contribution to the LCST-LLPS [13]. We further predict that, according to the LCST phase diagram, binding and bridging of proteins by the cations should be enhanced with increasing temperature [13]. However, a detailed insight into the binding and bridging

mechanism is yet to be obtained on the atomic scale.

Typical techniques used for thermodynamic studies such as this one include calorimetric methods, most commonly differential scanning and isothermal titration (DSC and ITC) calorimetry. These methods are capable of providing insight into the thermodynamics of protein-cation interactions. Additionally, detailed information on the interparticle potential can be obtained by scattering methods, notably small-angle scattering. However, a mechanistic understanding of the phase separation induced by the binding of multivalent cations to BSA requires precise information on the local structure and the chemical interactions at the cationic centres.

In this study we therefore apply X-ray absorption fine-structure (XAFS) spectroscopy, which probes the local structure around the cations. This method is based on the excitation of core electrons from the metal centres with photon energies near the photoionisation threshold. At photon energies just below the ionisation potential, X-ray absorption near-edge structure (XANES) is observed, which arises from transitions that provide information on the density of unoccupied states in the valence region, and hence the chemical state of the absorbing atoms. Beyond the ionisation potential, the spectra exhibit extended XAFS (EXAFS) oscillations due to backscattering of the low-energy photoelectrons by atoms in the close vicinity (up to about 5-6 Å distance) of the X-ray absorber. The EXAFS oscillations arise because the phase difference between the outgoing and backscattered waves depends on the kinetic energy of the photoelectrons which increases with photon energy. The principal contribution to the phase-difference is the product of the photoelectron momentum k and the round-trip distance $2R$, but there are also energy-dependent contributions arising from the interaction with the potentials of the excited atom and the backscatterers. The Fourier transform of the EXAFS is thus akin to a modified radial distribution function of atoms around the X-ray absorber, which can be analysed in detail by iterative fitting of a structure model. For the present work it is important that the amplitude of the EXAFS oscillations depends on the number of backscattering atoms located at a distance R from the absorber (usually referred to as the coordination number or CN). The amplitude of the oscillations is also influenced by the element-dependent backscattering strength of the atomic potentials, the inelastic losses of electrons while travelling the distance $2R$. Dephasing of the backscattered photoelectron wave through thermal and static disorder is usually accounted for by a Debye-Waller factor [155]. The Debye-Waller approximation holds only if disorder is small and/or harmonic (Gaussian) in nature. For the description of strong and/or non-harmonic disorder, more advanced models need to be used.

In this study, we present *in situ* EXAFS measurements at the Y K-edge to study the aqueous BSA-YCl_3 system described above. We investigate both a protein-poor and a protein-rich phase obtained *via* LLPS of a sample prepared inside the LLPS region (blue ellipsoid in Fig. 8.1). A larger CN of Y^{3+} is observed in the dilute phase than in the dense one, indicating a higher degree of hydration of Y^{3+} cations in the dilute phase. We then subject both phases to a temperature (T)

increase. In the dense phase, a decrease of the CN with increasing T is observed, pointing towards an increase in cation-mediated protein bridging. We discuss our findings in the context of our LCST-LLPS model and the patchy particle model rationalising the latter [13, 95].

8.3 Materials and Methods

BSA ($\geq$ 98% purity, product number A7906) and YCl_3 (anhydrous, 99.99% purity) were purchased from Sigma Aldrich (now Merck, Darmstadt, Germany). Solutions were prepared by dissolving desired amounts of protein or salt in deionised degassed MilliQ water (18.2 MΩ, Merck Millipore, Darmstadt, Germany). The exact concentration of the protein stock solution was then determined by UV-Vis spectroscopy (absorbance at 280 nm [1]).

A summary of the samples measured is given in Table 8.1 and their locations in the BSA-YCl_3 phase diagram are indicated in Fig. 8.1. In order to obtain dense and dilute phases of a sample exhibiting LLPS (samples 3 and 4 in Table 8.1; blue ellipsoid in Fig. 8.1), a sample with an initial concentration of 40 mM YCl_3 and 175 mg/ml BSA was prepared at room temperature (RT) and centrifuged for 5 min at $\sim$12,000 g (MiniSpin centrifuge, Eppendorf), resulting in separation of the solution into a protein-rich (dense) and a protein-poor (dilute) phase at RT. The dense and dilute phase were then measured independently *via* EXAFS. As a reference, a 200 mM YCl_3 aqueous solution without BSA (sample 1, Table 8.1) was measured.

Sample	YCl_3 (mM)	BSA (mg/ml)	Description
1	200	0	Reference (no BSA)
2	46	175	Single phase (cal. & ref.)
3	40	175	dense (after LLPS)
4	40	175	dilute (after LLPS)
5	40	175	denat. (after LLPS)

Table 8.1: *A list of samples discussed in this study. Other samples were measured for reference. "Cal." indicates calibration, "ref." indicates reference and "denat." indicates a thermally denatured sample. All samples were prepared at room temperature (RT). One sample was prepared per category and at least 2 scans were recorded per sample. The measurements indicate a high degree of reproducibility (cf. Fig. 8.7). Sample locations in the BSA-YCl_3 phase diagram are indicated in Fig. 8.1.*

EXAFS data were measured in transmission mode at the quick XAFS beamline B18, at Diamond Light Source (Didcot, Oxfordshire, UK). The synchrotron electron storage rings were operating with an energy of 3 GeV and a current of 300 mA. B18 is a bending magnet beamline and uses a silicon (311) crystal as a monochromator. A gas ion chamber was used for monitoring the intensity I_0

of the incoming monochromated X-ray beam. All spectra used in this study were measured in transmission mode. Each spectrum could be acquired over a period of $\approx$ 3 minutes. The beam size was approximately 100 μm (height) $\cdot$ 250 μm (width). EXAFS measurements were performed in a temperature range from 15 to 40 °C.

The experimental setup (Fig. 8.2) was as follows: a plastic tube containing 2 ml of sample was placed into an aluminium block (Fig. 8.2). The temperature of the aluminium block was controlled by water flowing through a piece of silicon tubing coiled thoroughly around the aluminium block. The geometry of the aluminium block allows for X-ray transmission across the plastic tube as well as fluorescence-yield detection perpendicular to the beam path. EXAFS fitting was carried out in the R-space over a k-range of 3-12 Å^{-1} and a R-(distance to the scattering atom) range of 1-4 Å using the Demeter software package [156]. The overall amplitude factor $S_0{}^2$ was fixed at 1 while all the other parameters energy (ΔE), bond distance (Δ R) and the Debye-Waller factors (σ^2) were allowed to float.

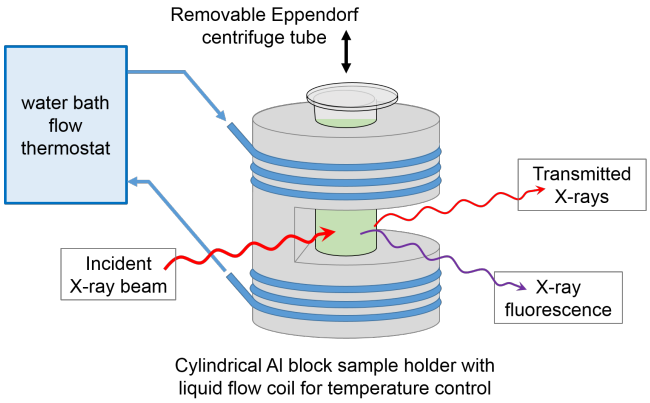

Figure 8.2: *Experimental setup. The temperature of the plastic tube containing the sample (light green cylinder) was adjusted and controlled by a coiled tubing (blue) connected to a water bath and surrounding the aluminium block (grey).*

8.4 Results and Discussion

The K-edge X-ray absorption fine-structure (XAFS) spectra of Y^{3+} were determined for a homogeneous (non-phase-separated) BSA-YCl_3 sample as well as for the dense and dilute phases obtained through LLPS. As references, spectra of a BSA-free 200 mM YCl_3 solution and of a BSA-YCl_3 solution denatured at 80 °C were also recorded (samples 1 and 5 in Table 8.1). A selection of normalised near-edge absorption spectra from these measurements is reproduced in Fig. 8.3.

It can be seen that the overall Y K X-ray absorption near-edge structure (XANES) remains very similar for all data, with a strong resonance ('white line') at a photon energy of 17056 eV. The same overall XANES was indeed observed

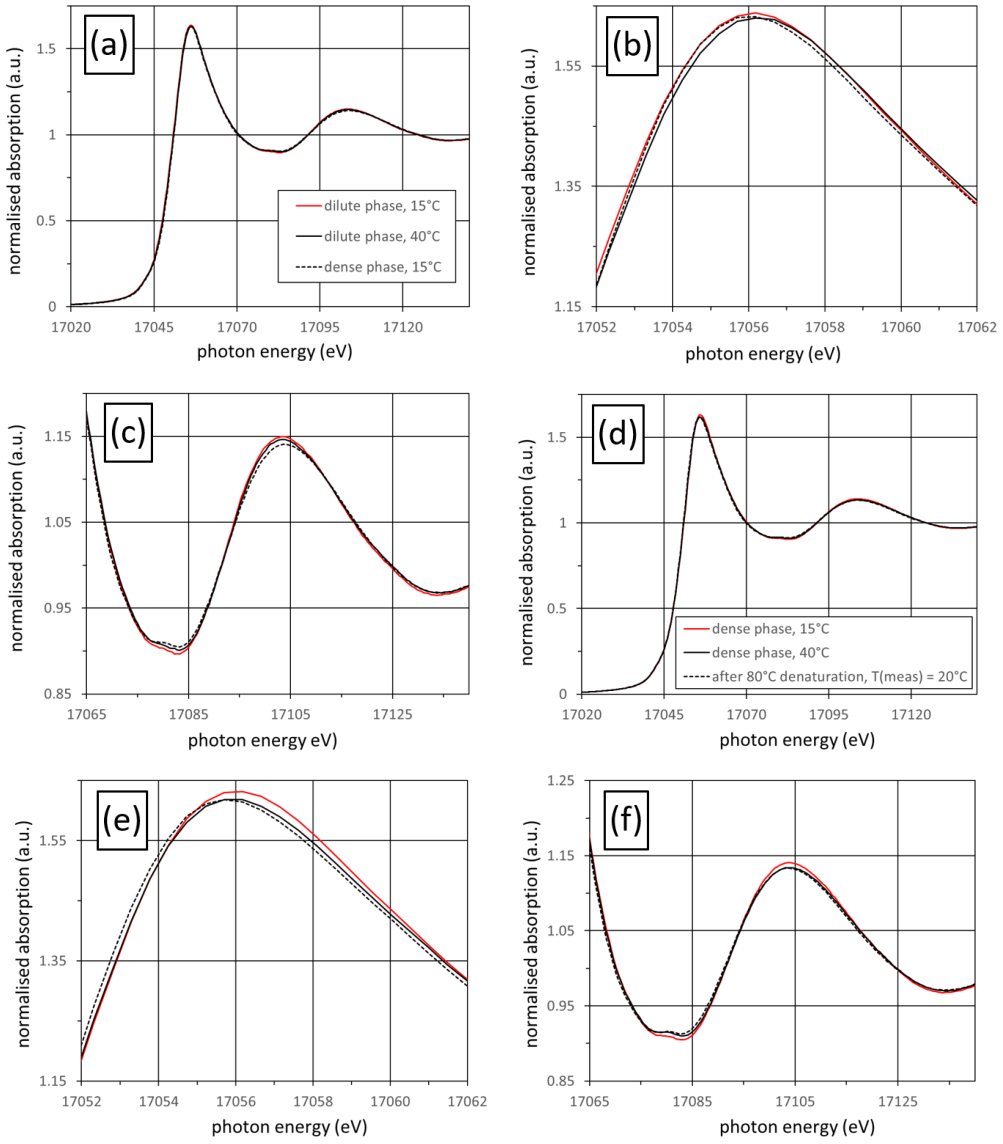

Figure 8.3: ***(a)*** *Y K XANES and first EXAFS oscillations of the dilute phase at 15 °C and 40 °C, as well as of the dense phase at 15 °C; note the similarity of the spectra suggesting the absence of major changes in electronic and geometric structure.* ***(b)*** *Close-up of the peak of the main XANES resonance in (a), indicating weak, but significant differences.* ***(c)*** *Close-up of the first EXAFS oscillations in the spectra from (a), likewise indicating weak, but significant differences.* ***(d)*** *Y K XANES and first EXAFS oscillations of the dilute phase at 15 °C alongside the spectra of the dense phase at 15 °C and 40 °C, again indicating the absence of major changes in electronic and geometric structure.* ***(e)*** *Close-up of the peak of the main XANES resonance in (d), indicating weak, but significant differences.* ***(f)*** *Close-up of the first EXAFS oscillations in the spectra from (d), indicating weak, but significant differences. The changes observed are well within the reproducibility limits of the spectroscopic measurements (cf. Figs. 8.7-8.9 in the Supporting Information, Section 8.7.1).*

for all samples investigated, with no strong variations in white line intensity, absorption edge energy position or appearance of additional XANES features. This suggests that the electronic structure of the Y absorbers remained broadly comparable throughout the study, with no strong changes due to, e.g., exchange of ligands with different elemental composition, local coordination geometry changes or Y oxidation state variations. However, closer inspection of the data in the regions of the main XAFS features reveals subtle, but significant variations, suggesting that the XAFS spectra are sensitive to subtle structural and/or electronic changes resulting from temperature variations and Y-protein interactions. These are illustrated in Fig. 8.3 through the magnified plots of spectral regions, which indicate changes that are on the order of about 10 percent of the fine-structure amplitudes, i.e., on the order of 0.01 within the normalised X-ray absorption spectra, which is an order of magnitude higher than the reproducibility of the spectroscopic measurements, i.e. well beyond the error bar (cf. Figs. 8.7-8.9 in the Supporting Information, Section 8.7.1). In the following, we will analyse the temperature-dependent EXAFS variations associated with the dilute and dense phases formed by LLPS.

In Fig. 8.4 we show EXAFS data and their Fourier transforms, which were derived from the data presented in Fig. 8.3. The Fourier transforms show that the observed reductions of the EXAFS amplitudes stem from a weaker pair correlation between the Y centres and their neighbour atoms. It was found that the EXAFS functions could be reproduced by models containing only oxygen as the atomic species binding to the metal centres. No evidence of binding to atoms other than oxygen, e.g. from the chloride ions present in the solutions, was evident in the EXAFS. A table with all parameters found by the iterative fitting analysis is given in the Supporting Information (Table 8.2, Section 8.7.1). The results (Fig. 8.5) reveal an overall higher oxygen CN in the dilute phases than in the dense one. Moreover, the CN of the homogeneous phase before phase separation was found to be at a value much closer to those observed for the dense phases (green triangle in Fig. 8.5). We note that, during our analysis, particular attention was paid to the well known correlation between the magnitude of the CNs and the Debye-Waller factors, which both influence the amplitude of the EXAFS oscillations, with high Debye-Waller factors tending to reduce the EXAFS amplitude, especially at higher k-values, while high CNs increase the overall amplitude. It is this counteracting correlation between these two amplitude factors that determines most of their statistical uncertainty when analysing individual spectra. As can be seen from Fig. 8.6, however, within the statistical uncertainties the values of the determined Debye-Waller vary very little, and they are very consistently slightly above (but close to) the value found for a homogeneous YCl_3 solution in the absence of protein. The slight increase can be rationalised by disorder in the local coordination due to interactions with protein molecules (see below). Moreover, the Debye Waller factors for dilute and dense phases were found to be virtually identical, suggesting that the observed difference between the EXAFS amplitudes of dilute and dense phases really stem from variations in the CNs and not from thermal or static

disorder. For both temperature series there also appears to be a weak overall increase of the Debye-Waller factors as a function of temperature, which is likewise an expected observation due to increasing thermal disorder.

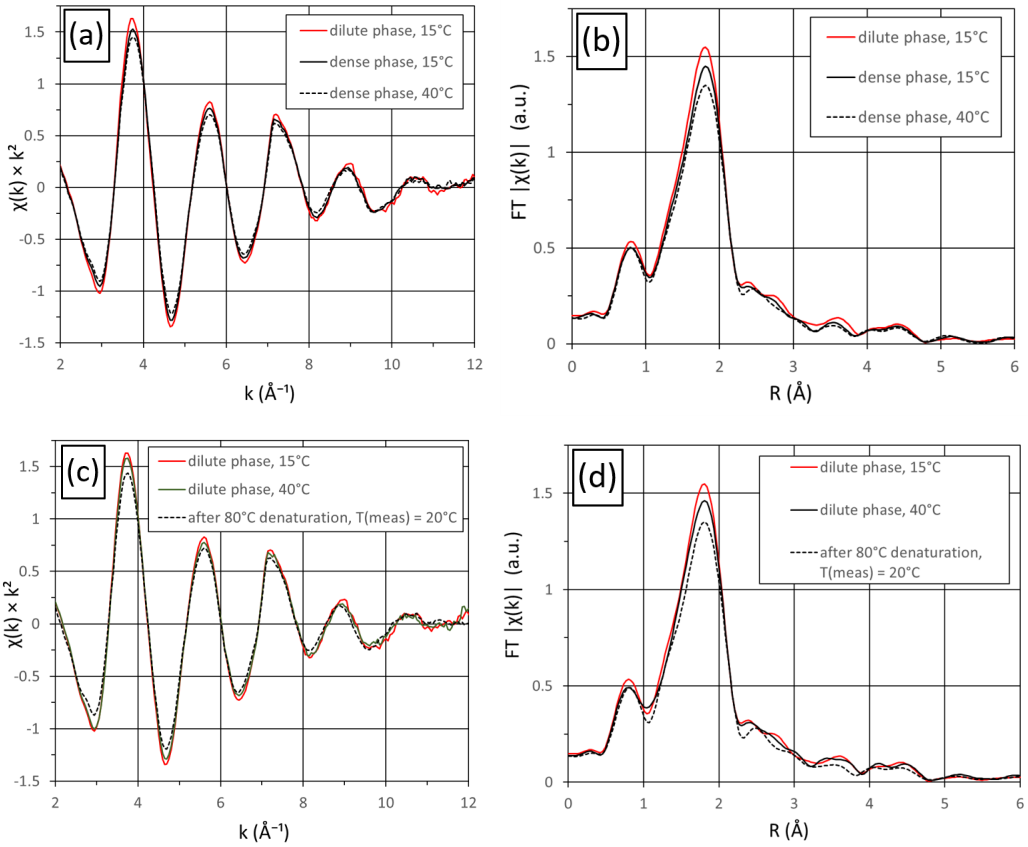

Figure 8.4: ***(a)*** *k^2-weighted Y K-edge EXAFS of the dilute phase at 15 °C as well as the dense phase at 15 °C and 40 °C; note the decreased amplitude of the EXAFS oscillations from the dense phase which decreases further upon heating.* ***(b)*** *Moduli of the Fourier-transformed EXAFS functions from (a). A reduction of the intensity of the peak around R = 1.8 Å suggests that the reduced EXAFS amplitudes stem from a weaker pair correlation between the Y centres and their ligand O atoms.* ***(c)*** *k^2-weighted Y K-edge EXAFS of the dilute phase at 15 °C in comparison with its EXAFS at 40 °C and with a denatured sample obtained by heating a 40 mM YCl_3 solution with 175 mg/ml BSA to 80 °C. As in (a), decreased EXAFS amplitudes are evident.* ***(d)*** *Moduli of the Fourier-transformed EXAFS functions from (c), showing that the reduced EXAFS amplitudes stem from a weaker pair correlation between the Y centres and their ligand O atoms. The observed changes on the order of are well within the reproducibility limits of the spectroscopic measurements (cf. Figs. 8.7-8.9 in the Supporting Information, Section 8.7.1).*

Thus, these findings based on the fitting analysis can be rationalised using our previous explanation of LCST-LLPS [13] as follows.

For the dilute phase, we find oxygen CNs just below and up to 11 (black data points in Fig. 8.5). These coordinating oxygen atoms stem very likely predominantly from water molecules bound to the Y^{3+} centres because we also observed a CN of 11 in the absence of BSA for a 200 mM YCl_3 aqueous reference solution (blue line in Fig. 8.5). Furthermore, there were no significant differences in the XANES regions of the reference and the dilute phase spectra (data not shown), which lends further support to a view that the speciation in the dilute phase and in aqueous YCl_3 is very similar. We cannot exclude that unspecific binding of Y^{3+} cations to the BSA surface takes place, but if so, it will, in all likelihood, be limited to one such interaction per metal centre, because coordination by surface functional groups from a second BSA protein molecule would require steric crowding that is impossible to reconcile with the observed high CNs. In addition, surface residues other than carboxylates are unlikely to feature the electrostatic properties (such as a strong local concentration of the negative charge) required to bind the highly positively charged Y^{3+} cations.

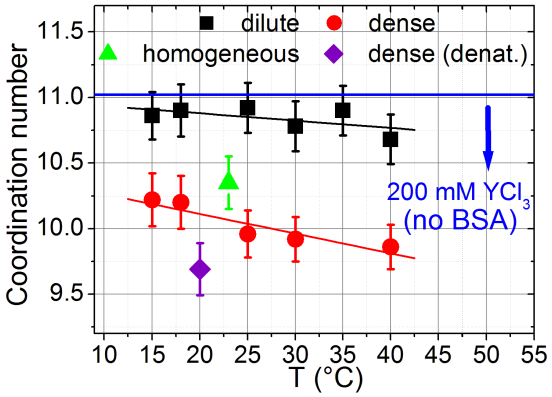

Figure 8.5: *EXAFS-derived oxygen CNs around the Y^{3+} centres in dense and dilute phases after LLPS (initial concentrations = 175 mg/ml BSA and 40 mM YCl_3) and in a homogeneous, non-phase-separated sample (175 mg/ml BSA and 46 mM YCl_3). The straight red and black lines represent linear fits to the CN in both the dense and dilute phase. The blue line indicates the CN of a 200 mM pure YCl_3 solution in the absence of BSA. A thermally denatured sample was measured as a reference and lies below the CN of the dense phases, as expected. See text for details.*

In the dense phase, the oxygen coordination number is significantly lower (i.e. relatively less Y^{3+} is surrounded by water molecules), suggesting that a higher fraction of the total number of Y^{3+} cations present interacts with BSA. Because of the steric crowding traced back to cation-mediated protein-protein bridging, this interaction is the likely cause of the observed reduction of the average CN, to values around 10.0±0.2 (Fig. 8.5). Based on protein crystal structures obtained via Y^{3+}-mediated protein bridging [82], we assume that one cation usually bridges

two BSA molecules via multidentate coordination involving up to four carboxyl or carboxylate groups per protein molecule. In the case of the protein β-lactoglobulin (BLG) which has a similar reentrant phase behaviour and, importantly, crystallises *via* Y^{3+}-mediated protein bridging, X-ray diffraction reveals a maximal coordination by 5 protein oxygens [82]. We note that this number is a reasonable order of magnitude for proteins with the kind of phase behaviour shown in Fig. 8.1, but given the fact that BSA and BLG are very different protein systems, the number of coordinating oxygen atoms cannot necessarily be easily transferred from one system to the other.

A similar coordination of Y^{3+} by BSA is likely to be entropically favoured due to the release of water molecules from the hydration layers surrounding both cations and protein [13] upon cation-protein binding and cation-mediated protein bridging. This entropy-driven interaction would already be present in the homogeneous phase prior to LLPS, which is in line with our observation of similar CNs for the homogeneous and the high density phase (*vide supra*). We remark that also the CN for the dilute phase slightly below 11 are consistent with the expectation that some Y^{3+} cations are bound to the proteins and not only surrounded by water molecules. Consequently, we assume that the smaller overall CN in the dense phase can be attributed to a significant fraction of Y^{3+} binding to BSA, which is also in line with the much higher BSA concentration in this phase. Assuming double bidentate binding, the predominant structure will be BSA-Y^{3+}-BSA bridges. Importantly, we further observe that, particularly in the dense phase, the overall values of the oxygen CNs decrease with increasing temperature, indicating that protein-protein bridging plays a more important role at higher temperatures, i.e. more Y^{3+} cations are not hydrated. This is underlined by the linear fit to this data set (red line in Fig. 8.5; slope = -0.015 $\pm$ 0.004). The effect is not as pronounced in the dilute phase (black line in Fig. 8.5) as indicated by its small slope (-0.006 $\pm$ 0.004) and its relatively high error bar compared to that of the linear fit to the dense phase data.

In addition to the samples discussed above, we measured a sample containing 175 mg/ml BSA and 40 mM YCl_3 after thermally denaturing it by immersion into hot (84 °C) water. We observe the CN of its Y^{3+} cations to be 9.7, i.e. even lower than that of the dense phase. We suggest this to reflect the fact that upon (partial) unfolding of BSA due to denaturing, the protein features a surface geometry different from its native one. This can include a scenario in which Y^{3+}-binding charged residues such as carboxylates which are predominantly found on the native protein surface are now on the inside of a coiled, gel-like network of many unfolded protein molecules. This, in turn, implies that Y^{3+} cations interacting with this network can be surrounded by even more carboxylates than when they are bridging native, folded proteins *via* surface-exposed residues.

It is interesting to note that the liquid-liquid phase separation of our protein solutions clearly observable on *macroscopic* length scales is reflected in rather subtle changes of the CN of Y^{3+} cations (i.e., a *microscopic* quality) upon crossing the LLPS boundary. This phenomenon is reminiscent of similar studies in Si-O

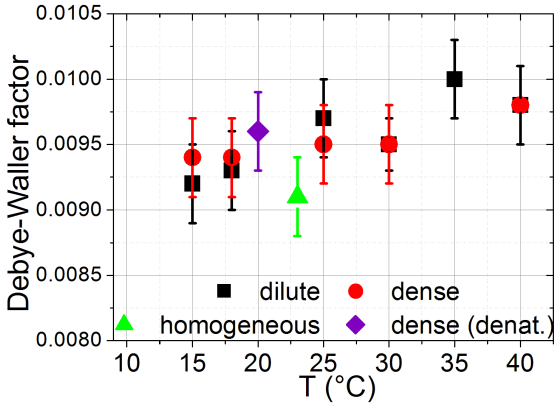

Figure 8.6: *Debye-Waller factors of the respective samples as a function of temperature.*

[271] and dielectric as well as ferroelectric systems [272]. In the first example, the length of the Si-O bond changes only very little as a function of temperature. The authors conclude that the thermal expansion of the material in question is much lower than expected on previous estimates. The second example illustrates that local distances between Bi and Ti atoms hardly change when an electric field is applied. Nevertheless, they do change their relative positions, thereby assuming a different distribution and changing the overall properties of the respective systems under investigation. Similarly, in our protein-cation system, a relatively small change in the distribution of water molecules around cations and protein molecules prompts a pronounced change in the global properties of our system.

8.5 Conclusions

In this study, we investigated the dependence of the coordination number (CN) of Y^{3+} cations in a BSA-YCl_3 system featuring liquid-liquid phase separation with a lower critical solution temperature (LCST-LLPS) into a protein-rich and a protein-poor phase. We observe that the CN of Y^{3+} is consistently lower in the protein-rich phases than in the corresponding protein-poor ones. This difference between the coordination numbers of both phases is traced back to the fact that in the dense phase cation-induced protein-protein bridging is dominant, meaning that few oxygens stemming from carboxyl groups on the BSA surface surround the Y^{3+} cations. In the dilute phase, however, Y^{3+} cations are primarily surrounded by oxygens from water molecules and therefore show an overall higher coordination number. In addition, the CN of Y^{3+} in the protein-rich phases features a pronounced temperature dependence, reflecting the increase of cation-mediated protein-protein bridging with increasing temperature.

Our observations reflect the LCST-LLPS mechanism remarkably well. This

study allows us to link changes in the coordination number of Y^{3+} to macroscopic phase behaviour of BSA-YCl_3 systems. The results reported here thus enable us to provide atom-level evidence for the mechanism of LCST-LLPS reported earlier [13, 14, 89]. With this study, we hope to stimulate further theoretical and experimental research of charge-controlled interactions in soft matter.

8.6 Acknowledgement

We thank Diamond Light Source (Harwell Science and Innovation Campus, Oxfordshire, UK) for beamtime allocation on beamline B18. We thank L. Al-Madhagi (Univ. of Leeds, UK) for experimental assistance during our beamtime. We gratefully acknowledge financial support by the DFG (SCHR700/21-1). O.M. acknowledges a fellowship by the *Studienstiftung des deutschen Volkes* and thanks R. Roth (Tübingen) for helpful discussions.

8.7 Supporting Information

8.7.1 Reproducibility of spectroscopic data and EXAFS fitting parameters

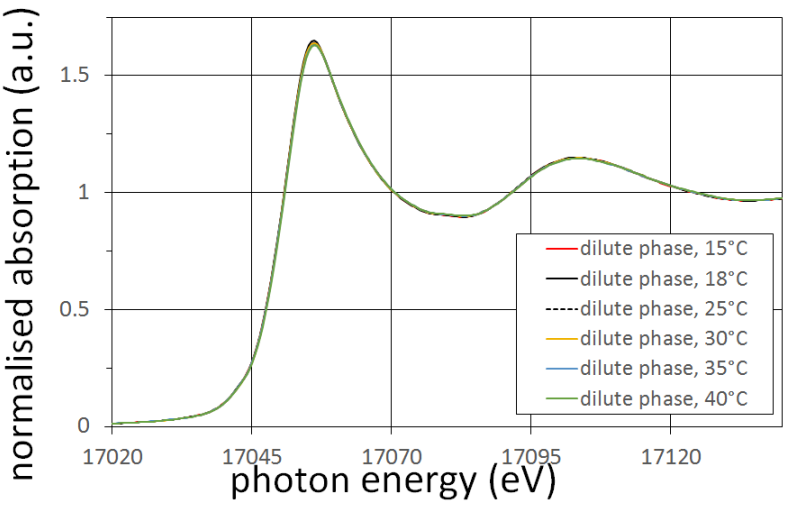

Figure 8.7: *Series of temperature-dependent XAFS spectra of the dilute phase formed by LLPS, demonstrating the reproducibility of the spectroscopic data.*

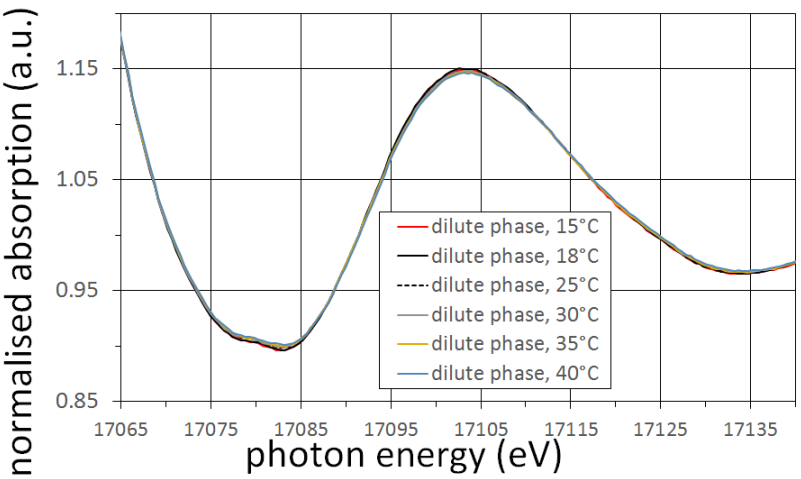

Figure 8.8: *As Fig. 8.7, zoom on the intermediate-keV region.*

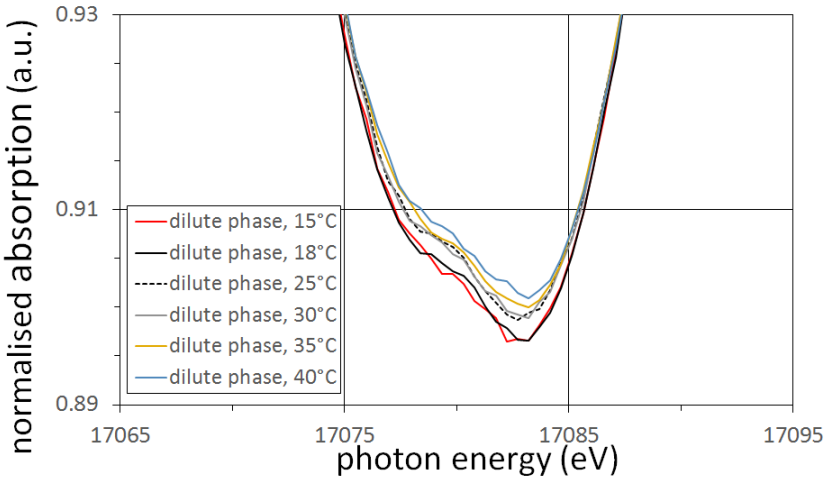

Figure 8.9: *As Figs. 8.7 and 8.8, further zoom on the high-keV region. Note in particular how the EXAFS amplitude systematically decreases as a function of temperature, indicating sensitivity to temperature-induced changes within* $\pm\ 5\,°C$ *and reproducibility of normalised absorption changes within an error of* $< 10^{-3}$.

Table 8.2: *Parameters obtained by the fitting analysis of the temperature-dependent EXAFS spectra of the dilute and dense phases. Sample details are given in the main text. Unless indicated otherwise, the initial pre-LLPS BSA concentration was 175 mg/ml in all cases. T_{meas} is the temperature at which the measurement was performed. "dil." indicates dilute phases and "den." the corresponding dense phases obtained after LLPS. "denat." indicates a thermally denatured sample measured as a reference. The overall amplitude factor, S_0^2, was fixed to 1. "CN" are the Y^{3+} coordination numbers obtained from the fits. R indicates the distance to the scattering atom (Å). "DWF" ($Å^{-2}$) are the Debye-Waller factors. "dE_0" (eV) denotes the shift from the arbitrarily chosen energy position, E_0, of the absorption edge. All data were obtained in transmission mode.*

YCl_3 (mM)	T_{meas}	CN	DWF	R	dE_0
46 (no LLPS)	23	10.35 ± 0.20	0.0091 ± 0.0003	2.37 ±0.002	-3.4 ± 0.2
40 (dil.)	15	10.86 ± 0.18	0.0092 ± 0.0003	2.37 ±0.002	-4.2 ± 0.2
40 (dil.)	18	10.90 ± 0.20	0.0093 ± 0.0003	2.37 ±0.002	-4.3 ± 0.2
40 (dil.)	25	10.92 ± 0.19	0.0097 ± 0.0003	2.37 ±0.002	-4.1 ± 0.2
40 (dil.)	30	10.78 ± 0.19	0.0095 ± 0.0002	2.37 ±0.002	-4.1 ± 0.2
40 (dil.)	35	10.90 ± 0.19	0.0100 ± 0.0003	2.37 ±0.002	-4.2 ± 0.2
40 (dil.)	40	10.68 ± 0.19	0.0098 ± 0.0003	2.37 ±0.002	-3.9 ± 0.2
40 (den.)	15	10.22 ± 0.20	0.0094 ± 0.0003	2.37 ±0.002	-3.2 ± 0.2
40 (den.)	18	10.20 ± 0.20	0.0094 ± 0.0003	2.37 ±0.002	-3.8 ± 0.2
40 (den.)	25	9.96 ± 0.18	0.0095 ± 0.0003	2.37 ±0.002	-3.5 ± 0.2
40 (den.)	30	9.92 ± 0.17	0.0095 ± 0.0003	2.37 ±0.002	-3.5 ± 0.2
40 (den.)	40	9.86 ± 0.17	0.0098 ± 0.0003	2.37 ±0.002	-3.5 ± 0.2
40 (denat.)	20	9.69 ± 0.20	0.0096 ± 0.0003	2.37 ±0.002	-3.7 ± 0.2
200 (no BSA)	23	11.02 ± 0.27	0.0084 ± 0.0003	2.37 ± 0.002	-3.2 ± 0.2

Part IV

Conclusions, open questions and directions for future work

Chapter 9

Conclusions

The results obtained in the course of this thesis are first briefly summarised in the following. Subsequently, open questions and inspiration for future investigations are provided.

In the first part of the present thesis, a mechanistic explanation of LCST-LLPS in solutions of BSA and YCl_3 was provided. Using zeta potential measurements and isothermal titration calorimetry (ITC), it was found that this phase transition is driven by the entropic gain experienced by hydration water molecules upon cation-protein binding and cation-mediated protein-protein bridging. These findings regarding LCST-LLPS in a protein-multivalent salt system, of general interest for research of soft matter thermodynamics, were published in the *Journal of Physical Chemistry B* (Matsarskaia *et al.*, *JPCB* **120** (2016), 7731-7736).

Given that LCST-LLPS also occurs in systems containing BSA and multivalent salts other than YCl_3, the effect of the respective cations used was investigated in the second part. The experiments performed focused on the salts YCl_3, $HoCl_3$ and $LaCl_3$. Zeta potential measurements showed that the affinities of the three cations to BSA can be rated according to their respective strengths as $Ho^{3+} > Y^{3+} > La^{3+}$. The same order of strengths applies to the interprotein attraction induced by the three cations, as was shown by small-angle X-ray scattering (SAXS) and temperature-controlled UV-Vis absorbance measurements. Considering the rather similar ITC signals obtained for BSA-$HoCl_3$ and BSA-YCl_3 systems, it is clear that cation radius is not the only parameter to be considered when comparing the different BSA-cation systems. In fact, as backed up by similar findings by other authors [223, 225, 226], the highly complex behaviour and hydration of the lanthanides as well as their potential differences to yttrium need to be considered. Nevertheless, the choice of the respective cation is a valuable tool allowing to fine-tune the phase behaviour of protein systems. Notably, the fine-tuning can be enhanced by using mixtures of cations with different affinities to BSA. This is of relevance for, e.g., the design of polymer- or protein-based "smart" materials sensitive to various parameters such as temperature and/or ionic strength. These results have been published in *Physical Chemistry Chemical Physics* (Matsarskaia *et al.*, *Phys. Chem. Chem. Phys* **20** (2018), 27214-27225).

The fact that cation mixtures can be used to fine-tune phase behaviour in BSA solutions was further exploited in the subsequent part of this thesis. Systems containing BSA and mixtures with varying ratios of the strongly and weakly interacting salts $HoCl_3$ and $LaCl_3$ were characterised with respect to the widths of their

respective coexisting regions. A stronger overall attraction brought about by a higher $HoCl_3$ concentration led to a wider liquid-liquid coexistence region. To elucidate the effect the different interprotein attraction strengths have on the kinetics of phase separation, the dense coexisting phases of these samples were subjected to temperature jumps with different final temperatures T_{fin}. The development and growth of the characteristic length scale ξ was monitored as a function of time and T_{fin}. Higher $HoCl_3$ concentrations in combination with high T_{fin} were observed to lead to an increasing deviation from the Lifshitz-Slyozov power law predicting a growth behaviour of $\xi \sim t^{1/3}$. In particular, higher $HoCl_3$ concentrations were shown to allow samples to enter an arrested state at relatively low temperatures. These results underline that a careful choice of the multivalent salt used has a strong influence on both thermodynamic properties and LLPS kinetics of the samples used, providing a multiparameter framework for rationally manipulating the properties of protein-salt systems. These findings are currently being prepared for publication in the *Journal of Physical Chemistry B* (Matsarskaia *et al.*, *J. Phys. Chem. B*, Article ASAP, DOI 10.1021/acs.jpcb.8b10725 (2019)). .

In the final part of this thesis, the mechanism behind LCST-LLPS was monitored using EXAFS in order to correlate the kinetics of this temperature-dependent phase transition with changes in the local structure of Y^{3+}-water complexes. To this end, the coordination number (CN) of Y^{3+} cations was monitored as a function of YCl_3 and BSA concentrations. The measurements show that in the case of a low BSA concentration (dilute phases of a phase-separated sample), the overall CN of Y is higher than in the corresponding dense phases. In accordance with the mechanistic explanation of LCST-LLPS in BSA-YCl_3 systems, this indicates that in the dilute phase, Y^{3+} cations are surrounded by more water molecules and consequently coordinate a larger amount of oxygen molecules than in the dense phase where cation-mediated protein bridging predominates. These results are currently in preparation for publication in *Phys. Chem. Chem. Phys.* (Matsarskaia *et al.*, *in preparation*).

Chapter 10

Open questions and directions for future work

10.1 Surprising differences in phase behaviours of similar experimental systems

The above research gives rise to several open questions. The first one concerns the fundamental nature of the temperature-dependent LLPS observed in the systems studied here. While BSA shows LCST-LLPS in the presence of multivalent salts and in the temperature window experimentally accessible, β-lactoglobulin (BLG) — a protein which is also net negatively charged and which also undergoes reentrant condensation induced by YCl_3 — shows a combination of UCST and LCST behaviour depending on the salt concentration.[1] Whether this gives rise to an hourglass- or closed-loop-type phase diagram is still subject to investigation. Begam and colleagues attribute the different phase diagrams of BSA-YCl_3 and BLG-YCl_3 systems to differences in the balance of cation-protein binding and cation-mediated protein bridging [273].

An equally unresolved issue is the fact that human serum albumin (HSA) readily crystallises in the presence of multivalent salts [270] while crystallisation of BSA with multivalent salts has only been observed once (M. Wolf, F. Zhang, personal communication). Given that BSA and HSA share a large part of their primary sequences, the reason for this strong difference in their phase behaviours is yet unclear. A possible explanation involves the fact that BSA contains a small fraction of dimers which seem to be absent in HSA. The BSA dimers might change the crystal nucleation kinetics in this experimental system, leading to the differences in crystallisation behaviour observed experimentally.

[1] Experimental indications that BSA-YCl_3 (N. Begam) and BSA-$HoCl_3$/$LaCl_3$ (O. Matsarskaia) systems may feature both LCST and UCST have been obtained, *inter alia via* (U)SAXS, but the interpretation of the data is challenging for a variety of reasons.

10.2 Comprehensive concept of cation and anion influence on protein phase behaviour

The work presented here is concerned with the role of multivalent cations; the role of the chloride (Cl^-) counterions is not investigated. The latter has been studied in great detail by Braun *et al.* [106], revealing strong differences in the phase behaviour of BSA induced by Cl^- and nitrate ($(NO_3)^{3-}$) as Y^{3+} and La^{3+} counterions. The experiments have been further extended to studies of co-salting effects of Hofmeister salts in BSA-La^{3+} systems [274]. It is tempting to integrate these data and those obtained in this thesis into the framework of the Hofmeister effects through further studies. However, care needs to be taken when doing so since, while significant progress has been made towards understanding the Hofmeister effect on a fundamental level, some of its aspect still remain unclear and, in addition, lanthanides were not part of the original Hofmeister series.

10.3 Limits of the isotropic patchy particle model

The patchy-particle model used to rationalise the phase behaviour observed experimentally [95] assumes an isotropic distribution of patches. Similarly, the analysis of the SAXS data obtained in the course of this thesis is mostly based on a sticky hard sphere (SHS) model, equally assuming an isotropic attractive interaction. However, when studying cation-specific effects on the phase behaviour of BSA, an interesting aspect to consider is the anisotropy of protein-cation complexes given that both the protein itself as well as the distribution of cation binding sites are very likely at least slightly anisotropic. Kern and Frenkel [68] established a theoretical framework for anisotropically patchy systems and for future research it would be intriguing to apply a model similar to theirs to the cation-BSA systems studied here. This may help obtain a more detailed understanding of cation binding in situations where the isotropic patchy particle model reaches its limits. Similarly, the potential decoupling of cation-protein binding and cation-mediated protein bridging (discussed in Chapter 6) is an intriguing aspect not yet fully understood and certainly worth investigating from a theoretical point of view.

10.4 Thermodynamics and hydration of lanthanide cations

A very interesting albeit highly complicated topic are the intricate and fascinating chemical and physical properties of the yttrium and lanthanide salts used in the experiments described here. As discussed in Section 6, several studies [122, 221, 222]

established a semi-quantitative relation between cation radius and affinity to different macromolecules including proteins. On the other hand, other studies [223, 224] including the present one underline that a strictly monotonous dependence of affinity on cationic radius is not always given. An important factor to be considered here appears to be the relation between the chemical and physical properties of yttrium and the lanthanides. In fact, although yttrium has been found to be sufficiently similar to the lanthanide series to be considered and treated like a lanthanide [110], Moeller *et al.* [225, 226] found that it is particularly yttrium which, depending on its ligand, seems to give rise to molecular complexes the stability of which resembles either the heavier or the lighter lanthanides. This interferes with a straightforward classification of yttrium and its affinity to BSA with respect to other lanthanides. Gomez *et al.* [223] tentatively trace the observations of a non-monotonous relation between cationic radius and cation-protein affinities back to potentially incomplete dehydration of Y^{3+} cations. With ion hydration being a well-known driving force of ion-ligand interactions (see, e.g., Refs. [194] and [275]) and the LCST-LLPS in the experimental systems studied here being a hydration entropy-driven process, this is clearly an aspect warranting further attention.

The properties and behaviour of the lanthanides have been studied extensively using various experimental techniques [79, 80, 105, 113–115, 122, 276–278]. The advancement of computational methods now allows to focus on aspects not easily accessible by experiments such as polarisability and, importantly, hydration behaviour and dynamics [108, 116, 118, 121, 279–284]. In particular, precise enthalpic and entropic contributions to the two latter aspects can be accessed computationally [118, 121]. A comprehensive computational approach directed at disentangling the thermodynamics of lanthanide-protein interactions on a fundamental thermodynamic level, including explicit modelling of the lanthanide electron orbitals, would help clarify many open questions. It is important to keep in mind that the complexity of these systems — rooted in difficulties with modelling even pure lanthanide solutions due to, *inter alia*, non-negligible relativistic effects [118, 124] — will presently likely render the addition of a molecule as complicated as a protein into such calculations borderline impossible in terms of calculation times (M. Dolg, personal communication). Nevertheless, advances in computational devices will potentially allow for such calculations, or simplified subsets thereof, to be performed in the future.

List of own publications

- **Olga Matsarskaia**, Michal K. Braun, Felix Roosen-Runge, Marcell Wolf, Fajun Zhang, Roland Roth, and Frank Schreiber
  Cation-induced hydration effects cause lower critical solution temperature behavior in protein solutions
  J. Phys. Chem. B **120** (2016), 7731-7736

- **Olga Matsarskaia**, Felix Roosen-Runge, Gudrun Lotze, Johannes Möller, Alessandro Mariani, Fajun Zhang, and Frank Schreiber
  Tuning phase transitions of aqueous protein solutions by multivalent cations
  Phys. Chem. Chem. Phys. **20** (2018), 27214-27225

- **Olga Matsarskaia**, Stefano Da Vela, Alessandro Mariani, Zhendong Fu, Fajun Zhang, and Frank Schreiber
  Phase separation kinetics in protein-salt mixtures with compositionally tuned interactions
  J. Phys. Chem. B, Article ASAP, DOI 10.1021/acs.jpcb.8b10725 (2019)

- **Olga Matsarskaia**, Sin-Yuen Chang, Felix Roosen-Runge, Stephen Parry, Giannantonio Cibin, Fajun Zhang, Sven L. M. Schroeder, and Frank Schreiber
  Protein condensation in the presence of lanthanide metal ions: relating local structure at the metal centres to phase behaviour
  in preparation (2019)

- Michal K. Braun, Marcell Wolf, **Olga Matsarskaia**, Stefano Da Vela, Felix Roosen-Runge, Michael Sztucki, Roland Roth, Fajun Zhang, and Frank Schreiber
  Strong isotope effects on effective interactions and phase behavior in protein solutions in the presence of multivalent ions
  J. Phys. Chem. B **121** (2017), 1731-1739

- Michal K. Braun, Andrea Sauter, **Olga Matsarskaia**, Marcell Wolf, Felix Roosen-Runge, Michael Sztucki, Roland Roth, Fajun Zhang, and Frank Schreiber
  Reentrant phase behavior in protein solutions induced by multivalent salts: strong effect of anions Cl^- versus NO_3^-
  J. Phys. Chem. B **122** (2018), 11978-11985

- Ralph Maier, Andrea Sauter, Georg Zocher, Stefano Da Vela, **Olga Matsarskaia**, Ralf Schweins, Michael Sztucki, Fajun Zhang, Thilo Stehle, and Frank Schreiber
  Protein crystallization with a metastable liquid-liquid phase separation
  in preparation (2019)

Acknowledgement

Scientific work is always a group effort and it is therefore a pleasure to thank those who accompanied me throughout the past years.

First of all, I express my sincerest gratitude to my supervisors F. Zhang and F. Schreiber for their enthusiastic support, their scientific creativity, their continuous guidance, patience, optimism, encouragement and mentoring as well as for their contagious eagerness to tackle scientific challenges. I am very grateful for the numerous opportunities to network and broaden my horizon they provided me through allowing me to participate in (inter)national conferences, undertake scientific visits and, importantly, perform experiments at renowned large-scale facilities. The inspirational work with my supervisors has allowed me to grow both as a scientist and as a person and I count myself truly lucky to have joined their research group.

I am indebted to F. Roosen-Runge for his unwaveringly encouraging and enthusiastic support with the often challenging, but all the more intriguing analysis and interpretation of my experimental data.

I sincerely thank M. Dolg, M. Klopotek, M. Oettel, R. Roth, H.-J. Schöpe and T. Seydel for our extremely fruitful discussions about various scientific topics which helped me significantly improve my understanding of our experimental systems and the theoretical models behind them.

I am grateful to the anonymous reviewers of our publications for their insightful, constructive and encouraging comments.

I thank the ESRF and the ILL (Grenoble, France), the FRM-II (Garching, Germany) and DLS (Didcot, Oxfordshire, UK) for the allocation of beamtime as well as for financial and administrative support during our experiments. Excellent on-site support by G. Lotze, A. Mariani, J. Möller and T. Narayanan at ID02 (ESRF); Z. Fu at KWS-3 (FRM-II); and G. Cibin and S. Parry at B18 (DLS) is gratefully acknowledged.

I am very grateful to S.L.M. Schroeder and S.-Y. Chang for experimental support and data analysis throughout our EXAFS collaboration. Thanks for support with the temperature-controlled EXAFS cell setup is due to L. Al-Madhagi.

Thanks is due to T. Kennel (FRM-II) and A. Geiger (DLS) for lab support during beamtimes. Furthermore, I acknowledge the Partnership for Soft and Condensed Matter (PSCM, Grenoble) for sharing their lab resources as well as Y. Gerelli, I. Grillo, D. Hess, P. Lloria, D. Pontoni and S. Verdon for lab and administrative support.

Sharing of their lab resources by F. Bono, T. Stehle and N. Jaspert is gratefully acknowledged. I furthermore thank S. Shanmugaratnam, C. Wolf and P. Christodoulou for assistance with ITC experiments and M. Dietrich for help with zeta potential measurements.

I gratefully acknowledge a PhD fellowship by the *Studienstiftung des Deutschen Volkes* and financial support to our group by the *Deutsche Forschungsgemeinschaft* (DFG). Moreover, I thank the Wilhelm and Else Heraeus foundation as well as SoftComp for travel grants to the DPG Spring meetings and the SoftComp Annual Meetings. I am grateful to the organisers and participants of the DPG Spring Meetings, the SoftComp Annual Meetings, the Neutrons in Structural Biology Conference (Grenoble, 06/2017) and the Structure and Stability of Biomolecules Conference (Košice, Slovakia, 09/2017) for providing excellent platforms for scientific exchange.

I thank R. Akiyama for hosting my supervisor F. Zhang and myself during a visit to Kyushu University (Fukuoka, Japan, 01/2015) and Y. Gerelli for giving me the opportunity to perform experiments at the PSCM as a visiting scientist (05/2015). I am equally grateful to Y. Liu and P. Fenter for hosting me during research visits to the National Institute of Standards and Technology (Gaithersburg, MD, USA) and to Argonne National Laboratory (Lemont, IL, USA) (07/2017).

Thanks for outstanding technical and administrative support is due to B. Hofferberth, H. Maurer, A. Rötschke and R. Zenke.

I express my sincere appreciation to A. Gerlach for his quiet, but tremendous organisational efforts "behind the scenes" of our group and especially our annual retreat.

I gratefully acknowledge very helpful proofreading of my thesis by F. Bäuerle, C. Beck, N. Begam, M. K. Braun, S. Y. Chang, S. Da Vela, M. Fries, A. Girelli, M. Grimaldo, H. Hansen-Goos, R. Maier, F. Roosen-Runge and D. Stopper.

Finally, a warm thank you to my (former) colleagues in Tübingen and Grenoble — notably F. Bäuerle, C. Beck, N. Begam, M. K. Braun, P. Christodoulou, S. Da Vela, G. Duva, M. Fries, A. Girelli, M. Grimaldo, J. Hagenlocher, H. Hansen-Goos, M. Hodas, M. Klopotek, D. Lepple, M. Lütje, R. Maier, M. Mikorski, A. Ragulskaya, A. Sauter (special thanks for allowing me to adapt her LaTeX templates), D. Stopper and M. Wolf — for being an excellent research team and to my family for their support.

Bibliography

[1] A. L. Lehninger, D. L. Nelson, and M. M. Cox, *Lehninger Principles of Biochemistry*, W. H. Freeman New York, 2005.

[2] R. K. Murray, D. A. Bender, K. M. Botham, P. J. Kennelly, V. W. Rodwell, and P. A. Weil, *Harper's Illustrated Biochemistry*, 28th ed., McGraw Hill, 2009.

[3] B. D. Mason, J. Z. van Enk, L. Zhang, R. L. Remmele, Jr., and J. Zhang, *Liquid-liquid phase separation of a monoclonal antibody and nonmonotonic influence of Hofmeister anions*, Biophys. J. **99** (2010), 3792–3800.

[4] Y. Wang, A. Lomakin, T. Hideshima, J. P. Laubach, O. Ogun, P. G. Richardson, N. C. Munshi, K. C. Anderson, and G. B. Benedek, *Pathological crystallization of human immunoglobulins*, Proc. Natl. Acad. Sci. USA **109** (2012), 13359–13361.

[5] L. C. Antonino, R. A. Kautz, N. Takayuki, R. O. Fox, and A. L. Fink, *Cold denaturation and ^2H_2O stabilization of a staphylococcal nuclease mutant*, Proc. Natl. Acad. Sci. USA **88** (1991), 7715–7718.

[6] M. Bucciantini, E. Giannoni, F. Chiti, F. Baroni, L. Formigli, J. Zurdo, N. Taddei, G. Ramponi, C. M. Dobson, and M. Stefani, *Inherent cytotoxicity of aggregates implies a common origin for protein misfolding diseases*, Nature **416** (2002), 507–511.

[7] G. B. Benedek, *Theory of transparency of the eye*, Appl. Opt. **10** (1971), 459–473.

[8] F. Zhang, M. W. A. Skoda, R. M. J. Jacobs, S. Zorn, R. A. Martin, C. M. Martin, G. F. Clark, S. Weggler, A. Hildebrandt, O. Kohlbacher, and F. Schreiber, *Reentrant condensation of proteins in solution induced by multivalent counterions*, Phys. Rev. Lett. **101** (2008), 148101.

[9] F. Zhang, S. Weggler, M. J. Ziller, L. Ianeselli, B. S. Heck, A. Hildebrandt, O. Kohlbacher, M. W. A. Skoda, R. M. J. Jacobs, and F. Schreiber, *Universality of protein reentrant condensation in solution induced by multivalent metal ions*, Proteins **78** (2010), 3450–3457.

[10] F. Zhang, R. Roth, M. Wolf, F. Roosen-Runge, M. W. A. Skoda, R. M. J. Jacobs, M. Sztucki, and F. Schreiber, *Charge-controlled metastable liquid-liquid phase separation in protein solutions as a universal pathway towards crystallization*, Soft Matter **8** (2012), 1313–1316.

[11] F. Zhang, F. Roosen-Runge, A. Sauter, R. Roth, M. W. A. Skoda, R. Jacobs, M. Sztucki, and F. Schreiber, *The role of cluster formation and metastable liquid-liquid phase separation in protein crystallization*, Faraday Discuss. **159** (2012), 313–325.

[12] F. Zhang, F. Roosen-Runge, A. Sauter, M. Wolf, R. M. J. Jacobs, and F. Schreiber, *Reentrant condensation, liquid-liquid phase separation and crystallization in protein solutions induced by multivalent metal ions*, Pure Appl. Chem. **86** (2014), 191–202.

[13] O. Matsarskaia, M. K. Braun, F. Roosen-Runge, M. Wolf, F. Zhang, R. Roth, and F. Schreiber, *Cation-induced hydration effects cause lower critical solution temperature behavior in protein solutions*, J. Phys. Chem. B **120** (2016), 7731–7736.

[14] S. Da Vela, M. K. Braun, A. Dörr, A. Greco, J. Möller, Z. Fu, F. Zhang, and F. Schreiber, *Kinetics of liquid-liquid phase separation in protein solutions exhibiting LCST phase behavior studied by time-resolved USAXS and VSANS*, Soft Matter **12** (2016), 9334–9341.

[15] A. S. Raut and D. S. Kalonia, *Pharmaceutical perspective on opalescence and liquid–liquid phase separation in protein solutions*, Mol. Pharmaceutics **13** (2016), 1431–1444.

[16] W. A. Eaton and J. Hofrichter, *Sickle cell hemoglobin polymerization*, Adv. Protein Chem. **40** (1990), 63–279.

[17] G. B. Benedek, *Cataract as a protein condensation disease: the Proctor Lecture.*, Invest. Ophth. Vis. Sci. **38** (1997), 1911–1921.

[18] J. Berry, S. C. Weber, N. Vaidya, M. Haataja, and C. P. Brangwynne, *RNA transcription modulates phase transition-driven nuclear body assembly*, Proc. Natl. Acad. Sci. USA **112** (2015), E5237–E5245.

[19] J. Berry, C. P. Brangwynne, and M. Haataja, *Physical principles of intracellular organization via active and passive phase transitions*, Rep. Prog. Phys. **81** (2018), 046601.

[20] T. Baumgart, A. T. Hammond, P. Sengupta, S. T. Hess, D. A. Holowka, B. A. Baird, and W. W. Webb, *Large-scale fluid-/fluid phase separation of proteins and lipids in giant plasma membrane vesicles*, Proc. Natl. Acad. Sci. USA **104** (2007), 3165–3170.

[21] C. F. Lee, C. P. Brangwynne, J. Gharakani, A. A. Hyman, and F. Jülicher, *Spatial organization of the cell cytoplasm by position-dependent phase separation*, Phys. Rev. Lett. (2013), 1962–1966.

[22] R. Mezzenga, P. Schurtenberger, A. Burbidge, and M. Michel, *Understanding foods as soft materials.*, Nature Materials **4** (2005), 729–740.

[23] R. Mezzenga and P. Fischer, *The self-assembly, aggregation and phase transitions of food protein systems in one, two and three dimensions*, Rep. Prog. Phys. **76** (2013), 046601.

[24] B. Heras and J. L. Martin, *Post-crystallization treatments for improving diffraction quality of protein crystals*, Acta Cryst. D **61** (2005), 1173–1180.

[25] J. A. Gavira, *Current trends in protein crystallization*, Arch. Biochem. Biophys. **602** (2016), 3 – 11.

[26] A. Ribeiro, F. J. Arias, J. Reguera, M. Alonso, and J. C. Rodríguez-Cabello, *Influence of the amino-acid sequence on the inverse temperature transition of elastin-like polymers*, Biophys. J. **97** (2009), 312–320.

[27] J. Israelachvili, *Intermolecular and Surface Forces*, Academic Press, London, 1991.

[28] H. N. W. Lekkerkerker and R. Tuinier, *Colloids and the depletion interaction*, Springer Netherlands, 2011.

[29] W. Poon, *Colloids as big atoms*, Science **304** (2004), 830–831.

[30] S. Asakura and F. Oosawa, *On Interaction between Two Bodies Immersed in a Solution of Macromolecules*, J. Chem. Phys. **22** (1954), 1255–1256.

[31] A. P. Gast, C. K. Hall, and W. B. Russel, *Phase Separations Induced in Aqueous Colloidal Suspensions by Dissolved Polymer*, Faraday Discuss. Chem. Soc. **76** (1983), 189–201.

[32] P. R. Sperry, H. B. Hopfenberg, and N. L. Thomas, *Flocculation of latex by water-soluble polymers: Experimental confirmation of a nonbridging, nonadsorptive, volume-restriction mechanism*, J. Colloid Interface Sci. **82** (1981), 62—76.

[33] A. P. Gast, W. B. Russel, and C. K. Hall, *An Experimental and Theoretical Study of Phase Transitions in the Polystyrene Latex and Hydroxyethylcellulose System*, J. Colloid Interface Sci. **109** (1986), 161–171.

[34] S. M. Ilett, A. Orrock, W. C. Poon, and P. N. Pusey, *Phase behavior of a model colloid-polymer mixture*, Phys. Rev. E **51** (1995), 1344–1352.

[35] E. J. Meijer and D. Frenkel, *Computer simulation of polymer-induced clustering of colloids*, Phys. Rev. Lett. **67** (1991), 1110–1113.

[36] J.-P. Hansen and I. R. McDonald, *Theory of simple liquids*, 3rd ed., Academic Press Amsterdam, 2006.

[37] G. Nägele, *The physics of colloidal soft matter*, Institute of Fundamental Technological Research, Warsaw, Poland, 2004.

[38] P. N. Pusey and W. van Megen, *Phase behaviour of concentrated suspensions of nearly hard colloidal spheres*, Nature **320** (1986), 340–342.

[39] J. D. van der Waals, *Over de continuiteit van den gas- en vloeistoftoestand*, Ph.D. thesis, Hoogeschool Te Leiden, 1873.

[40] P. Atkins and J. de Paula, *Physical chemistry*, 8th ed., Oxford University Press, Oxford, 2006.

[41] G. Wedler, *Lehrbuch der physikalischen Chemie*, 5th ed., Wiley-VCH, Weinheim, 2004.

[42] P. Papon, S. Schnur, J. Leblond, and P. Meijer, *The physics of phase transitions: Concepts and applications*, Advanced Texts in Physics, Springer Berlin Heidelberg, 2006.

[43] N. F. Carnahan and K. E. Starling, *Equation of state for nonattracting rigid spheres*, J. Chem. Phys. **51** (1969), 635–636.

[44] J. P. Sethna, *Statistical mechanics: entropy, order parameters, and complexity*, Clarendon Press, Oxford, 2011.

[45] W. Nolting, *Grundkurs Theoretische Physik 4: Spezielle Relativitätstheorie und Thermodynamik*, 6th ed., Springer, Braunschweig/Wiesbaden, 2005.

[46] R. A. L. Jones, *Soft condensed matter*, Oxford University Press, USA, 2002.

[47] A. V. Finkelstein, *The physics of protein molecules*, Izhevsk Institute of Computer Research, 2014.

[48] B. Smit, *Phase diagrams of Lennard-Jones fluids*, J. Chem. Phys. **96** (1992), 8639–8640.

[49] M. H. J. Hagen and D. Frenkel, *Determination of phase diagrams for the hard-core attractive Yukawa system*, J. Chem. Phys. **101** (1994), 4093–4097.

[50] E. Lomba and N. G. Almarza, *Role of the interaction range in the shaping of phase diagrams in simple fluids. The hard sphere Yukawa fluid as a case study*, J. Chem. Phys. **100** (1994), 8367–8372.

[51] M. G. Noro, N. Kern, and D. Frenkel, *The role of long-range forces in the phase behavior of colloids and proteins*, Europhys. Lett. **48** (1999), 332–338.

[52] M. G. Noro and D. Frenkel, *Extended corresponding-states behavior for particles with variable range attractions*, J. Chem. Phys. **113** (2000), 2941–2944.

[53] A. George and W. W. Wilson, *Predicting protein crystallization from a dilute solution property*, Acta Cryst. D **50** (1994), 361–365.

[54] D. Rosenbaum, P. Zamora, and C. Zukoski, *Phase behavior of small attractive colloidal particles*, Phys. Rev. Lett. **76** (1996), 150–153.

[55] V. J. Anderson and H. N. W. Lekkerkerker, *Insights into phase transition kinetics from colloid science*, Nature **416** (2002), 811–815.

[56] C. Ishimoto and T. Tanaka, *Critical behavior of a binary mixture of protein and salt water*, Phys. Rev. Lett. **39** (1977), 474–477.

[57] M. Muschol and F. Rosenberger, *Liquid–liquid phase separation in supersaturated lysozyme solutions and associated precipitate formation/crystallization*, J. Chem. Phys. **107** (1997), 1953–1962.

[58] J. A. Thomson, P. Schurtenberger, G. M. Thurston, and G. B. Benedek, *Binary liquid phase separation and critical phenomena in a protein/water solution*, Proc. Natl. Acad. Sci. USA **84** (1987), 7079–7083.

[59] P. Schurtenberger, R. A. Chamberlin, G. M. Thurston, J. A. Thomson, and G. B. Benedek, *Observation of critical phenomena in a protein-water solution*, Phys. Rev. Lett. **63** (1989), 2064–2067.

[60] M. L. Broide, C. R. Berland, J. Pande, O. O. Ogun, and G. B. Benedek, *Binary-liquid phase separation of lens protein solutions*, Proc. Natl. Acad. Sci. USA **88** (1991), 5660–5664.

[61] C. R. Berland, G. M. Thurston, M. Kondo, M. L. Broide, J. Pande, O. Ogun, and G. B. Benedek, *Solid-liquid phase boundaries of lens protein solutions*, Proc. Natl. Acad. Sci. USA **89** (1992), 1214–1218.

[62] P. L. San Biagio and M. U. Palma, *Spinodal lines and Flory-Huggins free-energies for solutions of human hemoglobins HbS and HbA*, Biophys. J. **60** (1991), 508–512.

[63] O. Galkin, K. Chen, R. L. Nagel, R. E. Hirsch, and P. G. Vekilov, *Liquid–liquid separation in solutions of normal and sickle cell hemoglobin*, Proc. Natl. Acad. Sci. USA **99** (2002), 8479–8483.

[64] Q. Chen, P. G. Vekilov, R. L. Nagel, and R. E. Hirsch, *Liquid-liquid phase separation in hemoglobins: Distinct aggregation mechanisms of the $\beta 6$ mutants*, Biophys. J. **86** (2004), 1702–1712.

[65] F. Cardinaux, T. Gibaud, A. Stradner, and P. Schurtenberger, *Interplay between spinodal decomposition and glass formation in proteins exhibiting short-range attractions*, Phys. Rev. Lett. **99** (2007), 118301.

[66] D. W. Urry, C.-H. Luan, T. M. Parker, D. C. Gowda, K. U. Prasad, M. C. Reid, and A. Safavy, *Temperature of polypeptide inverse temperature transition depends on mean residue hydrophobicity*, J. Am. Chem. Soc. **113** (1991), 4346–4348.

[67] A. Lomakin, N. R. Asherie, and G. B. Benedek, *Monte Carlo study of phase separation in aqueous protein solutions*, J. Chem. Phys. **104** (1996), 1646.

[68] N. Kern and D. Frenkel, *Fluid–fluid coexistence in colloidal systems with short-ranged strongly directional attraction*, J. Chem. Phys. **118** (2003), 9882–9889.

[69] T. H. Zhang and Y. Liu, *Experimental modelling of single-particle dynamic processes in crystallization by controlled colloidal assembly*, Chem. Soc. Rev. **43** (2014), 2324.

[70] J. M. Garcia-Ruiz, *Nucleation of protein crystals*, J. Struct. Biol. **142** (2003), 22–31.

[71] I. M. Lifshitz and V. Slyozov, *The kinetics of precipitation from supersaturated solid solutions*, J. Phys. Chem. Solids **19** (1961), 35–50.

[72] K. A. Majorek, P. J. Porebski, A. Dayal, M. D. Zimmerman, K. Jablonska, A. J. Stewart, M. Chruszcz, and W. Minor, *Structural and immunologic characterization of bovine, horse, and rabbit serum albumins*, Mol. Immunol. **52** (2012), 174–182.

[73] J. M. Berg, J. L. Tymoczko, and L. Stryer, *Lecture notebook for biochemistry*, W. H. Freeman, 2002.

[74] G. Loeffler, P. E. Petrides, and P. C. Heinrich, *Biochemie und Pathobiochemie*, 8th ed., Springer Medizin Verlag, Heidelberg, 2007.

[75] J. Yuan and G. Wang, *Lanthanide complex-based fluorescence label for time-resolved fluorescence bioassay*, J. Fluoresc. **15** (2005), 559–568.

[76] Y.-Y. Xu and I. A. Hemmilä, *Co-fluorescence enhancement system based on pivaloyltrifluoroacetone and yttrium for the simultaneous detection of europium, terbium, samarium and dysprosium*, Anal. Chim. Acta **256** (1992), 9–16.

[77] W. R. Harris and V. L. Pecoraro, *Thermodynamic binding constants for gallium transferrin*, Biochemistry **22** (1983), 292–299.

[78] W. R. Harris, *Thermodynamics of gallium complexation by human lactoferrin*, Biochemistry **25** (1986), 803–808.

[79] W. R. Harris and Y. Chen, *Difference ultraviolet spectroscopic studies on the binding of lanthanides to human serum albumin*, Inorg. Chem. **31** (1992), 5001–5006.

[80] W. R. Harris, *Binding and transport of nonferrous metals by serum transferrin*, Structure and Bonding **92** (1998), 121–162.

[81] W. R. Harris and L. Messori, *A comparative study of aluminum(III), gallium(III), indium(III), and thallium(III) binding to human serum transferrin*, Coord. Chem. Rev. **228** (2002), 237–262.

[82] F. Zhang, G. Zocher, A. Sauter, T. Stehle, and F. Schreiber, *Novel approach to controlled protein crystallization through ligandation of yttrium cations*, J. Appl. Cryst. **44** (2011), 755–762.

[83] F. Roosen-Runge, B. S. Heck, F. Zhang, O. Kohlbacher, and F. Schreiber, *Interplay of pH and binding of multivalent metal ions: Charge inversion and reentrant condensation in protein solutions*, J. Phys. Chem. B **117** (2013), 5777–5787.

[84] M. Wolf, F. Roosen-Runge, F. Zhang, R. Roth, M. W. Skoda, R. M. Jacobs, M. Sztucki, and F. Schreiber, *Effective interactions in protein–salt solutions approaching liquid–liquid phase separation*, J. Mol. Liq. **200** (2014), 20–27.

[85] A. Sauter, M. Oelker, G. Zocher, F. Zhang, T. Stehle, and F. Schreiber, *Nonclassical pathways of protein crystallization in the presence of multivalent metal ions*, Cryst. Growth Des. **14** (2014), 6357–6366.

[86] A. Sauter, F. Roosen-Runge, F. Zhang, G. Lotze, R. M. J. Jacobs, and F. Schreiber, *Real-time observation of nonclassical protein crystallization kinetics*, J. Am. Chem. Soc. **137** (2015), 1485–1491.

[87] A. Sauter, F. Roosen-Runge, F. Zhang, G. Lotze, A. Feoktystov, R. M. J. Jacobs, and F. Schreiber, *On the question of two-step nucleation in protein crystallization*, Faraday Discuss. **179** (2015), 41–58.

[88] A. Sauter, F. Zhang, N. K. Szekely, V. Pipich, M. Sztucki, and F. Schreiber, *Structural Evolution of Metastable Protein Aggregates in the Presence of Trivalent Salt Studied by (V)SANS and SAXS*, J. Phys. Chem. B **120** (2016), 5564–5571.

[89] M. K. Braun, M. Wolf, O. Matsarskaia, S. Da Vela, F. Roosen-Runge, M. Sztucki, R. Roth, F. Zhang, and F. Schreiber, *Strong isotope effects on effective interactions and phase behavior in protein solutions in the presence of multivalent ions*, J. Phys. Chem. B **121** (2017), 1731–1739.

[90] M. R. Fries, D. Stopper, M. K. Braun, A. Hinderhofer, F. Zhang, R. M. J. Jacobs, M. W. A. Skoda, H. Hansen-Goos, R. Roth, and F. Schreiber, *Multivalent-ion-activated protein adsorption reflecting bulk reentrant behavior*, Phys. Rev. Lett. **119** (2017), 228001.

[91] T. T. Nguyen, I. Rouzina, and B. I. Shklovskii, *Reentrant condensation of DNA induced by multivalent counterions*, J. Chem. Phys. **112** (2000), 2562–2568.

[92] P.-Y. Hsiao, *Overcharging, charge inversion, and reentrant condensation: Using highly charged polyelectrolytes in tetravalent salt solutions as an example of study*, J. Phys. Chem. Lett. **114** (2008), 7347–7350.

[93] H. G. Schild and D. A. Tirrell, *Microcalorimetric detection of lower critical solution temperatures in aqueous polymer solutions*, J. Phys. Chem. **94** (1990), 4352–4356.

[94] T. Lopez-Leon, J. L. Ortega-Vinuesa, D. Bastos-Gonzalez, and A. Elaissari, *Thermally sensitive reversible microgels formed by poly(N-Isopropylacrylamide) charged chains: A Hofmeister effect study*, J. Colloid. Interface Sci. **426** (2014), 300–307.

[95] F. Roosen-Runge, F. Zhang, F. Schreiber, and R. Roth, *Ion-activated attractive patches as a mechanism for controlled protein interactions*, Sci. Rep. **4** (2014), 7016.

[96] E. Bianchi, J. Largo, P. Tartaglia, E. Zaccarelli, and F. Sciortino, *Phase diagram of patchy colloids: Towards empty liquids*, Phys. Rev. Lett. **97** (2006), 168301.

[97] E. Bianchi, R. Blaak, and C. N. Likos, *Patchy colloids: state of the art and perspectives*, Phys. Chem. Chem. Phys. **13** (2011), 6397–6410.

[98] A. Bujacz, *Structures of bovine, equine and leporine serum albumin*, Acta Cryst. D **68** (2012), 1278–1289.

[99] J. M. Peula-Garcia, R. Hidaldo-Alvarez, and F. J. de las Nieves, *Protein co-adsorption on different polystyrene latexes: electrokinetic characterization and colloidal stability*, Colloid Polym. Sci. **275** (1997), 198–202.

[100] J. Lee and S. Timasheff, *Partial specific volumes and interactions with solvent components of proteins in guanidine hydrochloride*, Biochemistry **13** (1974), 257–265.

[101] F. Roosen-Runge, M. Hennig, F. Zhang, R. M. J. Jacobs, M. Sztucki, H. Schober, T. Seydel, and F. Schreiber, *Protein self-diffusion in crowded solutions*, Proc. Natl. Acad. Sci. USA **108** (2011), 11815–11820.

[102] E. Riedel and C. Janiak, *Anorganische Chemie*, de Gruyter Berlin, 2007.

[103] A. D. McNaught and A. Wilkinson, *IUPAC. Compendum of chemical terminology*, 2nd ed., Blackwell Scientific Publications, 1997.

[104] B. H. Mahan, *University Chemistry*, 3rd ed., Addison-Wesley Publishing Company, 1967.

[105] C. H. Evans, *Biochemistry of the Lanthanides*, Springer Science + Business Media, New York, 1990.

[106] M. K. Braun, A. Sauter, O. Matsarskaia, M. Wolf, F. Roosen-Runge, M. Sztucki, R. Roth, F. Zhang, and F. Schreiber, *Reentrant phase behavior in protein solutions induced by multivalent salts: Strong effect of anions Cl^- versus NO_3^-*, submitted.

[107] R. D. Shannon, *Revised effective ionic radii and systematic studies of interatomic distances in halides and chaleogenides*, Acta Cryst. A **32** (1976), 751–767.

[108] P. D'Angelo, A. Zitolo, V. Migliorati, G. Chillemi, M. Duvail, P. Vitorge, S. Abadie, and R. Spezia, *Revised ionic radii of lanthanoid(III) ions in aqueous solution*, Inorg. Chem. **50** (2011), 4572–4579.

[109] T. Ikeda, M. Hirata, and T. Kimura, *Hydration structure of Y^{3+} and La^{3+} compared: An application of metadynamics*, J. Chem. Phys. **122** (2005).

[110] F. G. N. Cloke, *Zero oxidation state compounds of scandium, yttrium, and the lanthanides*, Chem. Soc. Rev. **22** (1993), 17–24.

[111] G. R. Choppin and K. L. Nash, *Actinide separation science*, Radiochim. Acta (1995), 225–236.

[112] S. R. Vallabhajosula, J. F. Harwig, J. K. Siemsen, and W. Wolf, *Radiogallium localization in tumors: Blood binding and transport and the role of transferrin*, J. Nucl. Med. **21** (1980), 650–656.

[113] A. Habenschuss and F. H. Spedding, *The coordination (hydration) of rare earth ions in aqueous chloride solutions from x-ray diffraction. I.* $TbCl_3$, $DyCl_3$, $ErCl_3$, $TmCl_3$, *and* $LuCl_3$, J. Chem. Phys. **70** (1979), 2797–2806.

[114] A. Habenschuss and F. H. Spedding, *The coordination (hydration) of rare earth ions in aqueous chloride solutions from x- ray diffraction. II.* $LaCl_3$, $PrCl_3$, *and* $NdCl_3$, J. Chem. Phys. **70** (1979), 3758–3763.

[115] A. Habenschuss and F. H. Spedding, *The coordination (hydration) of rare earth ions in aqueous chloride solutions from x-ray diffraction. III.* $SmCl_3$, $EuCl_3$ *and series behavior*, J. Chem. Phys. **73** (1979), 442–450.

[116] M. Duvail, R. Spezia, and P. Vitorge, *A dynamic model to explain hydration behaviour along the lanthanide series*, Chem. Phys. Chem. **9** (2008), 693–696.

[117] C. Cossy, A. C. Barnes, J. E. Enderby, and A. E. Merbach, *The hydration of* Dy^{3+} *and* Yb^{3+} *in aqueous solution: A neutron scattering first order difference study*, J. Chem. Phys. **90** (1989), 3254.

[118] J. Zhang, N. Heinz, and M. Dolg, *Understanding lanthanoid(III) hydration structure and kinetics by insights from energies and wave functions*, Inorg. Chem. **53** (2014).

[119] I. Persson, P. D'Angelo, S. De Panfilis, M. Sandström, and L. Eriksson, *Hydration of lanthanoid(III) ions in aqueous solution and crystalline hydrates studied by EXAFS spectroscopy and crystallography: The myth of the "gadolinium break"*, Chemistry - A European Journal **14** (2008), 3056–3066.

[120] R. J. Hinchey and J. W. Cobble, *Standard-State Entropies for the Aqueous Trivalent Lanthanide and Yttrium Ions*, Inorg. Chem. **9** (1970), 917–921.

[121] J. Ciupka, X. Cao-Dolg, J. Wiebke, and M. Dolg, *Computational study of lanthanide(III) hydration*, Phys. Chem. Chem. Phys. **12** (2010), 13215.

[122] G. R. Choppin, *Structure and thermodynamics of lanthanide and actinide complexes in solution*, Pure Appl. Chem. **27** (1971), 23–41.

[123] C. Beuchat, D. Hagberg, R. Spezia, and L. Gagliardi, *Hydration of lanthanide chloride salts: A quantum chemical and classical molecular dynamics simulation study*, J. Phys. Chem. B **114** (2010), 15590–15597.

[124] P. Pyykkö, *Relativistic effects in chemistry: more common than you thought*, Annu. Rev. Phys. Chem. **63** (2012), 45–64.

[125] D. Sivia, *Elementary scattering theory for X-ray and neutron users*, Oxford University Press, 2011.

[126] P. Lindner and T. Zemb, *Neutrons, X-rays, and light: Scattering methods applied to soft condensed matter*, Elsevier North-Holland, 2002.

[127] S. Skou, R. E. Gillilan, and N. Ando, *Synchrotron-based small-angle X-ray scattering of proteins in solution*, Nature Protocols **9** (2014), 1727–1739.

[128] J. S. Pedersen, *Analysis of small-angle scattering data from colloids and polymer solutions: modeling and least-squares fitting*, Adv. Colloid Interface Sci. **70** (1997), 171–210.

[129] P. Debye, *Zerstreuung von Röntgenstrahlen*, Annalen der Physik **351** (1915), 809–823.

[130] J. Als-Nielsen and D. McMorrow, *Elements of modern X-ray physics*, John Wiley & Sons, West Sussex, United Kingdom, 2011.

[131] A. Tardieu, A. Le Verge, M. Malfois, F. Bonneté, S. Finet, M. Riès-Kautt, and L. Belloni, *Proteins in solution: from X-ray scattering intensities to interaction potentials*, J. Cryst. Growth **196** (1999), 193–203.

[132] D. I. Svergun and M. H. J. Koch, *Small-angle scattering studies of biological macromolecules in solution*, Rep. Prog. Phys. **66** (2003), 1735–1782.

[133] J. Gunton, A. Shiryayev, and D. Pagan, *Protein condensation: Kinetic pathways to crystallization and disease*, Cambridge University Press, 2007.

[134] A. Guinier and G. Fournet, *Small-angle scattering of X-rays*, vol. 14, Wiley New York, 1955.

[135] W. Schärtl, *Light scattering from polymer solutions and nanoparticle dispersions*, Springer, 2007.

[136] F. Bonneté and D. Vivarès, *Interest of the normalized second virial coefficient and interaction potentials for crystallizing large macromolecules*, Acta Cryst. D **58** (2002), 1571–1575.

[137] S. R. Kline, *Reduction and analysis of SANS and USANS data using IGOR Pro*, J. Appl. Cryst. **39** (2006), 895–900.

[138] G. A. Vliegenthart and H. N. W. Lekkerkerker, *Predicting the gas–liquid critical point from the second virial coefficient*, J. Chem. Phys. **112** (2000), 5364–5369.

[139] M. Bée, *Quasielastic neutron scattering*, Adam Hilger, Bristol, 1988.

[140] S. Busch, W. Doster, S. Longeville, V. Sakai, and T. Unruh, *Microscopic protein diffusion at high concentration*, MRS Bulletin. Quasielastic Neutron Scattering Conference, 2006, pp. 117–116.

[141] F. Roosen-Runge, M. Hennig, T. Seydel, F. Zhang, M. W. Skoda, S. Zorn, R. M. Jacobs, M. Maccarini, P. Fouquet, and F. Schreiber, *Protein diffusion in crowded electrolyte solutions*, Biochim. Biophys. Acta Proteins Proteom. **1804** (2010), 68–75.

[142] M. Hennig, F. Roosen-Runge, F. Zhang, S. Zorn, M. W. A. Skoda, R. M. J. Jacobs, T. Seydel, and F. Schreiber, *Dynamics of highly concentrated protein solutions around the denaturing transition*, Soft Matter **8** (2012), 1628–1633.

[143] M. Grimaldo, F. Roosen-Runge, M. Hennig, F. Zanini, F. Zhang, N. Jalarvo, M. Zamponi, F. Schreiber, and T. Seydel, *Hierarchical molecular dynamics of bovine serum albumin in concentrated aqueous solution below and above thermal denaturation*, Phys. Chem. Chem. Phys. **17** (2015), 4645–4655.

[144] M. Grimaldo, F. Roosen-Runge, M. Hennig, F. Zanini, F. Zhang, M. Zamponi, N. Jalarvo, F. Schreiber, and T. Seydel, *Salt-induced universal slowing down of the short-time self-diffusion of a globular protein in aqueous solution*, J. Phys. Chem. Lett. **6** (2015), 2577–2582.

[145] W. Doster, S. Cusack, and W. Petry, *Dynamical transition of myoglobin revealed by inelastic neutron scattering*, Nature **337** (1989), 754–756.

[146] F. Gabel, D. Bicout, U. Lehnert, M. Tehei, M. Weik, and G. Zaccai, *Protein dynamics studied by neutron scattering*, Q. Rev. Biophys. **35** (2002), 327–367.

[147] M. Grimaldo, F. Roosen-Runge, F. Zhang, T. Seydel, and F. Schreiber, *Diffusion and dynamics of γ- globulin in crowded aqueous solutions*, J. Phys. Chem. B **118** (2014), 7203–7209.

[148] G. Zaccai, *How soft is a protein? a protein dynamics force constant measured by neutron scattering*, Science **288** (2000), 1604–1607.

[149] J. Teixeira, M. C. Bellissent-Funel, S. H. Chen, and B. Dorner, *Observation of new short-wavelength collective excitations in heavy water by coherent inelastic neutron scattering*, Phys. Rev. Lett. **54** (1985), 2681–2683.

[150] J. Teixeira, M.-C. Bellissent-Funel, S. H. Chen, and A. J. Dianoux, *Experimental determination of the nature of diffusive motions of water molecules at low temperatures*, Phys. Rev. A **31** (1985), 1913–1917.

[151] I. Cendoya, A. Alegria, J. Alberdi, and J. Colmenero, *Effect of blending on the PVME Dynamics. A dielectric, NMR, and QENS Investigation*, Macromolecules **12** (1999), 4065–4078.

[152] P. Coppens, D. Cox, E. Vlieg, and I. K. Robinson, *Synchrotron radiation crystallography*, Academic Press, London, 1992.

[153] Y. Sun and Y. Ren, *In situ synchrotron x-ray techniques for real-time probing of colloidal nanoparticle synthesis*, Part. Part. Syst. Charact. **30** (2013), 399–419.

[154] J. R. Helliwell, *Macromolecular Crystallography with Synchrotron Radiation*, Cambridge University Press, Cambridge, 1992.

[155] J. Penner-Hahn, *X-ray absorption spectroscopy*, Comprehensive Coordination Chemistry II, vol. 2, John Wiley & Sons, 2003, pp. 159–186.

[156] B. Ravel and M. Newville, *ATHENA, ARTEMIS, HEPHAESTUS: data analysis for x-ray absorption spectroscopy using IFEFFIT*, J. Synchrotron Rad. **12** (2005), 537–541.

[157] ESRF, *What is a synchrotron?*, https://www.esrf.eu/about/synchrotron-science/synchrotron, accessed on 14/08/2018.

[158] D. H. Tomboulian and P. L. Hartman, *Spectral and angular distribution of ultraviolet radiation from the 300-MeV Cornell Synchrotron*, Phys. Rev. **102** (1956), 1423–1447.

[159] A. Balerna and S. Mobilio, *Synchrotron radiation: Basics, methods and applications*, ch. 1. Introduction to Synchrotron Radiation, Springer Berlin-Heidelberg, 2016.

[160] T. Narayanan, M. Sztucki, P. Van Vaerenbergh, J. Leonardon, J. Gorini, L. Claustre, F. Sever, J. Morse, and P. Boesecke, *A multipurpose instrument for time-resolved ultra small-angle and coherent X-ray scattering*, J. Appl. Cryst. **51** (2018).

[161] P. Van Vaerenbergh, J. Léonardon, M. Sztucki, P. Boesecke, J. Gorini, L. Claustre, F. Sever, J. Morse, and T. Narayanan, *An upgrade beamline for combined wide, small and ultra small-angle x-ray scattering at the ESRF*, AIP Conference Proceedings, vol. 1741, AIP Publishing, 2016, p. 030034.

[162] M. Sztucki, J. Gorini, L.-P. Vassalli, L. Goirand, P. van Vaerenbergh, and T. Narayanan, *Optimization of a Bonse-Hart instrument by suppressing surface parasitic scattering*, J. Synchrotron Rad. **15** (2008), 341–349.

[163] V. Pipich and Z. Fu, *KWS-3: Very small angle scattering diffractometer with focusing mirror*, Journal of Large-Scale Research Facilities, 1, A31 **1** (2015).

[164] G. Goerigk and Z. Varga, *Comprehensive upgrade of the high-resolution small-angle neutron scattering instrument KWS-3 at FRM II*, J. Appl. Cryst. **44** (2011), 337–342.

[165] B. Henke and J. W. M. DuMond, *Low Angle X-Ray Diffraction with Long Wavelengths*, Phys. Rev. **89** (1953), 1300.

[166] B. Alefeld, D. Schwahn, and T. Springer, *New developments of small angle neutron scattering instruments with focussing*, Nucl. Instrum. Meth. **A274** (1989), 210–216.

[167] B. Alefeld, L. Dohmen, D. Richter, and T. Brückel, *X-ray space technology for focusing small-angle neutron scattering and neutron reflectometry*, Physica B **283** (2000), 330–332.

[168] E. Kentzinger, L. Dohmen, B. Alefeld, U. Rücker, J. Stellbring, A. Ioffe, D. Richter, and T. Brückel, *KWS-3, the new focusing-mirror ultra small-angle neutron scattering instrument and reflectometer at Jülich*, Physica B **350** (2004), 779–781.

[169] A. Mehta, *Ultraviolet-Visible (UV-Vis) Spectroscopy Limitations and Deviations of Beer-Lambert Law*, https://pharmaxchange.info/, 2012, accessed on 14/06/2018.

[170] A. Delgado, F. González-Caballero, R. Hunter, L. Koopal, and J. Lyklema, *Measurement and interpretation of electrokinetic phenomena*, J. Colloid Interface Sci. **309** (2007), 194–224.

[171] H. Ohshima, T. W. Healy, and L. R. White, *Accurate analytic expressions for the surface charge density/surface potential relationship and double-layer potential distribution for a spherical colloidal particle*, J. Colloid Interface Sci. **90** (1982), 17–26.

[172] H. Ohshima, *A simple expression for Henry's function for the retardation effect in electrophoresis of spherical colloidal particles*, J. Colloid Interface Sci. **168** (1994), 269–271.

[173] Malvern Instruments, *Zetasizer Nano user manual*, 2008.

[174] S. Leavitt and E. Freire, *Direct measurement of protein binding energetics by isothermal titration calorimetry*, Curr. Opinion Struct. Biol. **11** (2001).

[175] M. W. Freyer and E. A. Lewis, *Isothermal titration calorimetry: experimental design, data analysis, and probing macromolecule/ligand binding and kinetic interactions*, Methods Cell Biol. **84** (2008), 79–113.

[176] P. R. ten Wolde and D. Frenkel, *Enhancement of protein crystal nucleation by critical density fluctuations*, Science **277** (1997), 1975–1978.

[177] P. G. Vekilov, *Dense liquid precursor for the nucleation of ordered solid phases from solution*, Cryst. Growth Des. **4** (2004), 671–685.

[178] C. Gögelein, D. Wagner, F. Cardinaux, G. Nägele, and S. U. Egelhaaf, *Effect of glycerol and dimethyl sulfoxide on the phase behavior of lysozyme: Theory and experiments*, J. Chem. Phys. **136** (2012), 015102.

[179] J. Möller, S. Grobelny, J. Schulze, S. Bieder, A. Steffen, M. Erlkamp, P. Michael, M. Tolan, and R. Winter, *Liquid-liquid phase separation in protein solutions at elevated hydrostatic pressures*, Phys. Rev. Lett. **112** (2014), 028101.

[180] S. Moelbert and P. De Los Rios, *Hydrophobic interaction model for upper and lower critical solution temperatures*, Macromolecules **36** (2003), 5845–5853.

[181] Y. C. Bae, S. M. Lambert, D. S. Soane, and J. M. Prausnitz, *Cloud-Point Curves of Polymer Solutions from Thermooptical Measurements*, Macromolecules **24** (1991), 4403–4407.

[182] P. J. Roth, T. P. Davis, and A. B. Lowe, *Comparison between the LCST and UCST transitions of double thermoresponsive diblock copolymers: insights into the behavior of POEGMA in alcohols*, Macromolecules **45** (2012), 3221–3230.

[183] M. Manno, A. Emanuele, V. Martorana, P. L. San Biagio, D. Bulone, M. B. Palma-Vittorelli, D. T. McPherson, J. Xu, T. M. Parker, and D. W. Urry, *Interaction of processes on different length scales in a bioelastomer capable of performing energy conversion*, Biopolymers **59** (2001), 51–64.

[184] E. Y. Permyakov, *Metalloproteomics*, Wiley Hoboken New Jersey, 2009.

[185] R. Murthy, R. Nunez, J. Szklaruk, W. Erwin, D. C. Madoff, S. Gupta, K. Ahrar, M. J. Wallace, A. Cohen, D. M. Coldwell, A. S. Kennedy, and M. E. Hicks, *Yttrium-90 microsphere therapy for hepatic malignancy: Devices, indications, technical considerations, and potential complications*, Oncol. Interv. **2** (2005), S41–S55.

[186] A. Pol, T. R. M. Barends, A. Dietl, A. F. Khadem, J. Eygensteyn, M. S. M. Jetten, and H. J. M. Op den Camp, *Rare earth metals are essential for methanotrophic life in volcanic mudpots*, Environ. Microbiol. **16** (2014), 255–264.

[187] R. S. Sandhu, *A thermodynamic study of complexation reaction of yttrium(III), lanthanum(III) and cerium(III) with tyrosine*, Monatsh. Chem. **108** (1977), 51–55.

[188] F. M. Elzawawy, *Complex formation constants and thermodynamic parameters for La(III) and Y(III) L-serine complexes*, Monatsh. Chem. **122** (1991), 921–925.

[189] K. V. Ragnarsdottir, E. H. Oelkers, D. M. Sherman, and C. R. Collins, *Aqueous speciation of yttrium at temperatures from 25 to 340 °C at P_{sat}: an in situ EXAFS study*, Chem. Geol. **151** (1998), 29–39.

[190] P. Lindqvist-Reis, K. Lamble, S. Pattanaik, I. Persson, and M. Sandström, *Hydration of the yttrium(III) ion in aqueous solution. An X-ray diffraction and XAFS structural study*, J. Phys. Chem. B **104** (2000), 402–408.

[191] G. A. Jeffrey, *Hydrogen bonding in biological structures*, Springer-Verlag Berlin Heidelberg, 1991.

[192] J. D. Dunitz, *The entropic cost of bound water in crystals and biomolecules*, Science (New York) **264** (1994), 670.

[193] P. Ball, *Water as an active constituent in cell biology*, Chem. Rev. **108** (2008), 74–108.

[194] K. D. Collins, *Ions from the Hofmeister series and osmolytes: effects on proteins in solution and in the crystallization process*, Methods **34** (2004), 300–311.

[195] F. Zhang, F. Roosen-Runge, M. W. A. Skoda, R. M. J. Jacobs, M. Wolf, P. Callow, H. Frielinghaus, V. Pipich, S. Prevost, and F. Schreiber, *Hydration and interactions in protein solutions containing concentrated electrolytes studied by small-angle scattering*, Phys. Chem. Chem. Phys. **14** (2012), 2483–2493.

[196] P. D. Ross and A. P. Minton, *Analysis of non-ideal behavior in concentrated hemoglobin solutions*, J. Mol. Biol. **112** (1977), 437–452.

[197] F. Rosenberger, S. B. Howard, J. W. Sowers, and T. A. Nyce, *Temperature dependence of protein solubility - determination and application to crystallization in X-ray capillaries*, J. Cryst. Growth **129** (1993), 1–12.

[198] P. G. Vekilov, A. R. Feeling-Taylor, S.-T. Yau, and D. Petsev, *Solvent entropy contribution to the free energy of protein crystallization*, Acta Cryst. D **58** (2002), 1611–1616.

[199] A. Shiryayev, D. L. Pagan, J. D. Gunton, D. S. Rhen, A. Saxena, and T. Lookman, *Role of solvent for globular proteins in solution*, J. Chem. Phys. **122** (2005), 234911.

[200] N. Wentzel and J. D. Gunton, *Effect of solvent on the phase diagram of a simple anisotropic model of globular proteins*, J. Phys. Chem. B **112** (2008), 7803–7809.

[201] O. Matsarskaia, F. Roosen-Runge, G. Lotze, J. Möller, A. Mariani, F. Zhang, and F. Schreiber, *Tuning phase transitions of aqueous protein solutions by multivalent cations*, Phys. Chem. Chem. Phys **20** (2018), 27214–27225.

[202] L. M. Gaetke and C. K. Chow, *Copper toxicity, oxidative stress, and antioxidant nutrients*, Toxicology **189** (2003), 147–163.

[203] A. Pałasz and P. Czekaj, *Toxicological and cytophysiological aspects of lanthanides action*, Acta Biochim. Pol. **47** (2000), 1107–1114.

[204] D. McLachlan, C. Bergeron, J. Smith, D. Boomer, and S. L. Rifat, *Risk for neuropathologically confirmed Alzheimer's disease and residual aluminum in municipal drinking water employing weighted residential histories*, Neurology **46** (1996), 401–405.

[205] V. Rondeau, D. Commenges, H. Jacqmin-Gadda, and J.-F. Dartigues, *Relation between aluminum concentrations in drinking water and Alzheimer's disease: An 8-year follow-up study*, Am. J. Epidemiol. **152** (2000), 59–66.

[206] R. S. Stubbs, R. J. Cannan, and A. W. Mitchell, *Selective internal radiation therapy with 90-yttrium microspheres for extensive colorectal liver metastases*, J. Gastrointest. Surg. **5** (2001), 294–302.

[207] A. D. Sherry, E. R. Birnbaum, and D. W. Darnall, *A Nuclear Magnetic Resonance Study of Histidine-Neodymium(III) Complexes*, J. Biol. Chem. **70** (1972), 3489–3494.

[208] P. Caravan, J. J. Ellison, T. J. McMurry, and R. B. Lauffer, *Gadolinium(III) chelates as MRI contrast agents: Structure, dynamics and applications*, Chem. Rev. **99** (1999), 2293–2352.

[209] E. Dadachova, S. Mirzaeh, S. V. Smith, F. F. Knapp Jr., and E. L. Hetherington, *Radiolabeling antibodies with Holmium-166*, Appl. Radiat. Isot. **48** (1997), 477–481.

[210] J. Yu, N. Jackson, X. Xu, Y. Morgenstern, Y. Kaufmann, M. Ruths, J. de Pablo, and M. Tirrell, *Multivalent Counterions Diminish the Lubricity of Polyelectrolyte Brushes*, Science **1438** (2018), 1434–1438.

[211] I. Koltover, K. Wagner, and C. R. Safinya, *DNA condensation in two dimensions*, Proc. Natl. Acad. Sci. USA **97** (2000), 14046–14051.

[212] A. G. Cherstvy, A. A. Kornyshev, and S. Leikin, *Temperature-dependent DNA condensation triggered by rearrangement of adsorbed cations*, J. Phys. Chem. B **106** (2002), 13362–13369.

[213] C. Pasquier, M. Vazdar, J. Forsman, P. Jungwirth, and M. Lund, *Anomalous protein-protein interactions in multivalent salt solution*, J. Phys. Chem. B **121** (2017), 3000–3006.

[214] E. Jordan, F. Roosen-Runge, S. Leibfarth, F. Zhang, M. Sztucki, A. Hildebrandt, O. Kohlbacher, and F. Schreiber, *Competing salt effects on phase behavior of protein solutions: Tailoring of protein interaction by the binding of multivalent ions and charge screening*, J. Phys. Chem. B **118** (2014), 11365–11374.

[215] C. A. Dreiss, K. S. Jack, and A. P. Parker, *On the absolute calibration of bench-top small-angle x-ray scattering instruments: a comparison of different standard methods*, J. Appl. Cryst. **39** (2006), 32–38.

[216] J. B. Hayter and J. Penfold, *An analytic structure factor for macroion solutions*, Mol. Phys. **42** (1981), 109–118.

[217] J.-P. Hansen and J. B. Hayter, *A rescaled MSA structure factor for dilute charged colloidal dispersions*, Mol. Phys. **46** (1982), 651–656.

[218] R. J. Baxter, *Percus–Yevick equation for hard spheres with surface adhesion*, J. Chem. Phys. **49** (1968), 2770–2774.

[219] S. V. G. Menon, C. Manohar, and K. S. Rao, *A new interpretation of the sticky hard sphere model*, J. Chem. Phys. **95** (1991), 9186–9190.

[220] W. L. Hulse, J. Gray, and R. T. Forbes, *Evaluating the inter and intra batch variability of protein aggregation behaviour using Taylor dispersion analysis and dynamic light scattering*, Int. J. Pharm. **453** (2013), 351–357.

[221] K. Schomäcker, D. Mocker, R. Münze, and G.-J. Beyer, *Stabilities of lanthanide-protein complexes*, Appl. Radiat. Isot. **39** (1988), 261–264.

[222] G. E. Smolka, E. R. Birnbaum, and D. W. Darnall, *Rare earth metal ions as substitutes for the calcium ion in Bacillus subtilis alpha-amylase*, Biochemistry **10** (1971), 4556–4561.

[223] J. E. Gomez, E. R. Birnbaum, and D. W. Darnall, *Metal ion acceleration of the conversion of trypsinogen to Trypsin. Lanthanide ions as calcium ion substitutes*, Biochemistry **13** (1974), 3745–3750.

[224] P. Mulqueen, J. M. Tingey, and W. D. W. Horrocks, *Characterization of lanthanide(III) ion binding to calmodulin using luminescence spectroscopy*, Biochemistry **24** (1985), 6639–6645.

[225] T. Moeller and R. Ferrús, *Observations on the rare earths - LXXIII: The heat and entropy of formation of the 1:1 chelates of N-hydroxyethylethylenediaminetriacetic acid with the tripositive cations*, J. Inorg. Nucl. Chem. **20** (1961), 261–273.

[226] T. Moeller, D. F. Martin, L. C. Thompson, R. Ferrus, G. R. Feistel, and W. J. Randall, *The coordination chemistry of yttrium and the rare earth metal ions*, Chem. Rev. **65** (1965), 1–50.

[227] C. Clavaguéra and J. P. Dognon, *Accurate static electric dipole polarizability calculations of +3 charged lanthanide ions*, Chem. Phys. **311** (2005), 169–176.

[228] A. G. Cherstvy and A. A. Kornyshev, *DNA melting in aggregates: Impeded or facilitated?*, J. Phys. Chem. B **109** (2005), 13024–13029.

[229] A. González, A. Wildes, M. Marty-Roda, S. Cuesta-López, E. Mossou, A. Studer, B. Demé, G. Moiroux, J. L. Garden, N. Theodorakopoulos, and M. Peyrard, *Melting transition of oriented DNA fibers submerged in poly(ethylene glycol) solutions studied by neutron scattering and calorimetry*, J. Phys. Chem. B **122** (2018), 2504–2515.

[230] F. Sebastiani, A. Pietrini, M. Longo, L. Comez, C. Petrillo, F. Sacchetti, and A. Paciaroni, *Melting of DNA nonoriented fibers: A wide-angle x-ray diffraction study*, J. Phys. Chem. B **118** (2014), 3785–3792.

[231] M. Constantin, *Lower critical solution temperature versus volume phase transition temperature in thermoresponsive drug delivery systems*, Express Polym. Lett. **5** (2011), 839–848.

[232] B. O. Okesola and D. K. Smith, *Applying low-molecular weight supramolecular gelators in an environmental setting self-assembled gels as smart materials for pollutant removal*, Chem. Soc. Rev. **97** (2016), 219–243.

[233] B. B. Owen, R. C. Miller, C. E. Milner, and H. L. Cogan, *The dielectric constant of water as a function of temperature and pressure.*, J. Phys. Chem. **65** (1961), 2065–2070.

[234] D. C. Henry, *The Cataphoresis of Suspended Particles. Part I. The Equation of Cataphoresis*, Proceedings of the Royal Society A: Mathematical, Physical and Engineering Sciences **133** (1931), 106–129.

[235] O. Matsarskaia, S. Da Vela, A. Mariani, Z. Fu, F. Zhang, and F. Schreiber, *Phase-Separation Kinetics in Protein-Salt Mixtures with Compositionally Tuned Interactions*, J. Phys. Chem. B Article ASAP (2019).

[236] A. Boire, C. Sanchez, M.-H. Morel, M. P. Lettinga, and P. Menut, *Dynamics of liquid-liquid phase separation of wheat gliadins*, Sci. Rep. **8** (2018), 14441.

[237] W. Pan, O. Galkin, L. Filobelo, R. L. Nagel, and P. G. Vekilov, *Metastable mesoscopic clusters in solutions of sickle-cell hemoglobin*, Biophys. J. **92** (2007), 267–277.

[238] Y. Wang, Y. Wang, D. R. Breed, V. N. Manoharan, L. Feng, A. D. Hollingsworth, M. Weck, and D. J. Pine, *Colloids with valence and specific directional bonding*, Nature **491** (2012), 51–55.

[239] R. Schubert, A. Meyer, D. Baitan, K. Dierks, M. Perbandt, and C. Betzel, *Real-time observation of protein dense liquid cluster evolution during nucleation in protein crystallization*, Crystal Growth Design **17** (2017), 954–958.

[240] J. W. Cahn and J. E. Hilliard, *Free energy of a nonuniform system. III. Nucleation in a two-component incompressible fluid*, J. Chem. Phys. **31** (1959), 688–699.

[241] J. W. Cahn, *Phase separation by spinodal decomposition in isotropic systems*, J. Chem. Phys. **42** (1965), 93–99.

[242] D. A. Huse, *Corrections to late-stage behavior in spinodal decomposition: Lifshitz-Slyozov scaling and Monte Carlo simulations*, Phys. Rev. B **34** (1986).

[243] K. Binder and D. Stauffer, *Theory for the slowing down of the relaxation and spinodal decomposition of binary mixtures*, Phys. Rev. Lett. **33** (1974), 1006.

[244] K. Rundman and J. Hilliard, *Early stages of spinodal decomposition in an aluminum-zinc alloy*, Acta Metall. **15** (1967), 1025–1033.

[245] D. Laughlin and J. W. Cahn, *Spinodal decomposition in age hardening copper-titanium alloys*, Acta Metall. **23** (1975), 329–339.

[246] F. Bruder and R. Brenn, *Spinodal Decomposition in Thin Films of a Polymer Blend*, Phys. Rev. Lett. **69** (1992).

[247] F. S. Bates and P. Wiltzius, *Spinodal decomposition of a symmetric critical mixture of deuterated and protonated polymer*, J. Chem. Phys. **91** (1989), 3258–3274.

[248] G. Ramirez-Santiago and A. E. González, *Growth laws and spinodal decomposition type of scaling in fractal aggregation of colloids*, Physica A **236** (1997), 75–84.

[249] H. Sedgwick, K. Kroy, A. Salonen, M. Robertson, S. Egelhaaf, and W. Poon, *Non-equilibrium behavior of sticky colloidal particles: beads, clusters and gels*, Eur. Phys. J. E **16** (2005), 77–80.

[250] P. J. Lu, E. Zaccarelli, F. Ciulla, A. B. Schofield, F. Sciortino, and D. A. Weitz, *Gelation of particles with short-range attraction*, Nature **453** (2008), 499–503.

[251] N. A. Verhaegh, J. S. van Duijneveldt, J. K. Dhont, and H. N. Lekkerkerker, *Fluid-fluid phase separation in colloid-polymer mixtures studied with small angle light scattering and light microscopy*, Physica A **230** (1996), 409–436.

[252] J. K. G. Dhont, *An introduction to dynamics of colloids*, Elsevier Science B. V., 1996.

[253] J. K. G. Dhont, *Spinodal decomposition of colloids in the initial and intermediate stages*, J. Chem. Phys. **105** (1996), 5122–5125.

[254] E. Zaccarelli, *Colloidal gels: equilibrium and non-equilibrium routes*, J. Phys.: Condens. Matter **19** (2007), 323101.

[255] O. Annunziata, O. Ogun, and G. B. Benedek, *Observation of liquid–liquid phase separation for eye lens γS-crystallin*, Proc. Natl. Acad. Sci. USA **100** (2003), 970–974.

[256] M. Shah, O. Galkin, and P. G. Vekilov, *Smooth transition from metastability to instability in phase separating protein solutions*, J. Chem. Phys. **121** (2004), 7505–7512.

[257] O. Gliko, W. Pan, P. Katsonis, N. Neumaier, O. Galkin, S. Weinkauf, and P. G. Vekilov, *Metastable liquid clusters in super- and undersaturated protein solutions*, J. Phys. Chem. B **111** (2007), 3106–3114.

[258] T. Gibaud and P. Schurtenberger, *A closer look at arrested spinodal decomposition in protein solutions*, J. Phys.: Condens. Matter **21** (2009), 322201.

[259] Y. Wang, A. Lomakin, R. F. Latypov, and G. B. Benedek, *Phase separation in solutions of monoclonal antibodies and the effect of human serum albumin*, Proc. Natl. Acad. Sci. USA **108** (2011), 16606–16611.

[260] E. Bianchi, B. Capone, I. Coluzza, L. Rovigatti, and P. D. J. van Oostrum, *Limiting the valence: advancements and new perspectives on patchy colloids, soft functionalized nanoparticles and biomolecules*, Phys. Chem. Chem. Phys. **19** (2017), 19847–19868.

[261] G. Sudlow, D. J. Birkett, and D. N. Wade, *Spectroscopic techniques in the study of protein binding. a fluorescence technique for the evaluation of the albumin binding and displacement of warfarin and warfarin-alcohol*, Clin Exp Pharmacol Physiol. **2** (1975), 129–140.

[262] S. Da Vela, C. Exner, R. S. Schäufele, J. Möller, Z. Fu, F. Zhang, and F. Schreiber, *Arrested and temporarily arrested states in a protein-polymer mixture studied by USAXS and VSANS*, Soft Matter **13** (2017), 8756–8765.

[263] H. I. Okur, J. Hladílková, K. B. Rembert, Y. Cho, J. Heyda, J. Dzubiella, P. S. Cremer, and P. Jungwirth, *Beyond the Hofmeister series: Ion-specific effects on proteins and their biological functions*, J. Phys. Chem. B **121** (2017), 1997–2014.

[264] O. Matsarskaia, S.-Y. Chang, F. Roosen-Runge, S. Parry, G. Cibin, F. Zhang, S. L. M. Schroeder, and F. Schreiber, *Protein condensation in the presence of lanthanide metal ions: Relating local structure at the metal centres to phase behaviour*, in preparation (2018).

[265] R. Piazza, *Protein interactions and association: an open challenge for colloid science*, Curr. Opin. Colloid Interface Sci. **8** (2004), 515–522.

[266] F. Zhang, *Nonclassical nucleation pathways in protein crystallization*, J. Phys.: Condens. Matter **29** (2017), 443002.

[267] M. Delaye, J. Clark, and G. Benedek, *Identification of the scattering elements responsible for lens opacification in cold cataracts*, Biophys. J. **37** (1982), 647–656.

[268] D. Vivarès and F. Bonneté, *Liquid-liquid phase separation in urate oxdase/peg mixtures: Characterization and implications for protein crystallization*, J Phys. Chem. B **108** (2004), 6498–6507.

[269] S. Da Vela, F. Roosen-Runge, M. W. A. Skoda, R. M. J. Jacobs, T. Seydel, H. Frielinghaus, M. Sztucki, R. Schweins, F. Zhang, and F. Schreiber, *Effective interactions and colloidal stability of bovine γ-globulin in solution*, J. Phys. Chem. B **121** (2017), 5759–5769.

[270] R. Maier, A. Sauter, G. Zocher, S. Da Vela, O. Matsarskaia, R. Schweins, M. Sztucki, F. Zhang, T. Stehle, and F. Schreiber, *Protein crystallization with a metastable liquid-liquid phase separation*, in preparation.

[271] M. G. Tucker, M. T. Dove, and D. A. Keen, *Direct measurement of the thermal expansion of the si-o bond by neutron total scattering*, J. Phys.: Condens. Matter **12** (2000), L425–L430.

[272] T.-M. Usher, I. Levin, J. E. Daniels, and J. L. Jones, *Electric-field-induced local and mesoscale structural changes in polycrystalline dielectrics and ferroelectrics*, Sci. Rep. **5** (2015), 14678.

[273] N. Begam, S. Da Vela, F. Zhang, and F. Schreiber, *Unification of Lower Critical and Upper Critical Solution Temperatures of Protein Solutions*, in preparation (2018).

[274] L. Lang, *Effect of anions on the phase behavior of BSA solutions in the presence of multivalent salts*, Master's thesis, Eberhard Karls University Tübingen, 2018.

[275] K. D. Collins, *Ion hydration: Implications for cellular function, polyelectrolytes, and protein crystallization*, Biophys. Chem. **119** (2006), 271 – 281.

[276] G. R. Choppin and J. A. Chopoorian, *Complexes of the lanthanide elements with α-hydroxy carboxylate ligands*, J. Inorg. Nucl. Chem. (1961), 97–113.

[277] G. R. Choppin and P. J. Unrein, *Halide complexes of the lanthanide elements*, J. Inorg. Nucl. Chem. (1963), 387–393.

[278] G. R. Choppin, *The thermodynamics of lanthanide aminopolycarboxylate complexation*, Thermochim. Acta (1993), 1–7.

[279] X. Chu, A. Dalgarno, and G. C. Groenenboom, *Dynamic polarizabilities of rare-earth-metal atoms and dispersion coefficients for their interaction with helium atoms*, Phys. Rev. A **75** (2007), 1–4.

[280] M. Duvail, M. Souaile, R. Spezia, and T. Cartailler, *Pair interaction potentials with explicit polarization for molecular dynamics simulations of La^{3+} in bulk water*, J. Chem. Phys. **127** (2007), 034503.

[281] M. Duvail, R. Spezia, T. Cartailler, and P. Vitorge, *Temperature dependence of hydrated La^{3+} properties in liquid water, a molecular dynamics simulations study*, Chem. Phys. Lett. **448** (2007), 41–45.

[282] M. Duvail, P. Vitorge, and R. Spezia, *Building a polarizable pair interaction potential for lanthanoids(III) in liquid water: A molecular dynamics study of structure and dynamics of the whole series*, J. Chem. Phys. **130** (2009), 104501.

[283] M. Duvail, P. Vitorge, and R. Spezia, *Temperature influence on lanthanoids(III) hydration from molecular dynamics simulations*, Chem. Phys. Lett **498** (2010), 90–96.

[284] P. D'Angelo and R. Spezia, *Hydration of Lanthanoids(III) and Actinoids(III): An Experimental/Theoretical Saga*, Chemistry - A European Journal **18** (2012), 11162–11178.